Modelling of Transport Phenomena in Direct Methanol and Proton Exchange Membrane Fuel Cells

by

Erik Birgersson

February 2003
Technical Reports from
Royal Institute of Technology
Department of Mechanics
S-100 44 Stockholm, Sweden

Typsatt i $\mathcal{AMS}$-LaTeX.

Akademisk avhandling som med tillstånd av Kungliga Tekniska Högskolan i Stockholm framlägges till offentlig granskning för avläggande av teknologie licentiatexamen torsdagen den 27 februari 2003 kl 16.15 i sal E36, Kungliga Tekniska Högskolan, Lindstedtsvägen 3, Stockholm.

Universitetsservice US AB, Stockholm 2003

Modelling of Transport Phenomena in Direct Methanol and Proton Exchange Membrane Fuel Cells

Erik Birgersson
Department of Mechanics, Royal Institute of Technology
SE-100 44 Stockholm, Sweden.

Abstract

This thesis deals with modelling of two types of fuel cells, namely the direct methanol fuel cell (DMFC) and proton exchange membrane fuel cell (PEMFC).

One-phase models, comprising conservation of mass, momentum and species, are derived and analysed for the anode of the DMFC and the cathode of the PEMFC. The impact of hydrodynamic, electrochemical and geometrical features on the fuel cell performance are studied. The slenderness of the fuel cells allows the use of a narrow-gap approximation, leading to reduced models, with benefits such as reduced computational cost and understanding of the physical trends prior to any numerical computations.

Four different flow distributors are studied for the cathode of the PEMFC. These are: parallel flow channels run in coflow or counterflow arrangement, interdigitated channels and a foam. A quantitative comparison shows that the interdigitated channels can sustain the highest current densities, followed in descending order by the foam, the counterflow and coflow channels.

Descriptors: Hydrodynamics, DMFC, PEMFC, mass transfer, momentum transfer, multicomponent, asymptotic analysis.

Preface

This thesis considers modelling of transport phenomena in direct methanol and polymer electrolyte membrane fuel cells. The thesis is based on the following papers:

Paper 1. Vynnycky, M. and Birgersson, E. 2002, 'Analysis of a Model For Multicomponent Mass Transfer in the Cathode of a Polymer Electrolyte Fuel Cell'. *Accepted by SIAM, Journal of Applied Mathematics.*

Paper 2. Birgersson, E. and Vynnycky, M. 2002, 'A Quantitative Study of the Effect of Flow-Distributor Geometry in the Cathode of a PEM Fuel Cell'. *To be submitted.*

Paper 3. Birgersson, E. , Nordlund, J., Ekström, H., Vynnycky, M. and Lindbergh, G. 2002, 'A Reduced Two-Dimensional One-Phase Model for Analysis of the Anode of a DMFC'. *Submitted to Journal of the Electrochemical Society.*

The papers are re-set in the present thesis format.

Contents

CHAPTER 1

Introduction

In view of ever increasing levels of environmental pollution and thus a desire to replace the fossil-fuel-based economy with a cleaner alternative, the fuel cell has in recent years become a prime candidate as a power source for transport and stationary applications. The potential use of fuel cells range from distributed power sources and portable applications, such as laptops or even for the future dismounted soldier, to vehicles. Two such types of cells are the proton exchange membrane fuel cell (PEMFC) and the direct methanol fuel cell (DMFC), a schematic representation of these is shown in figure 1.

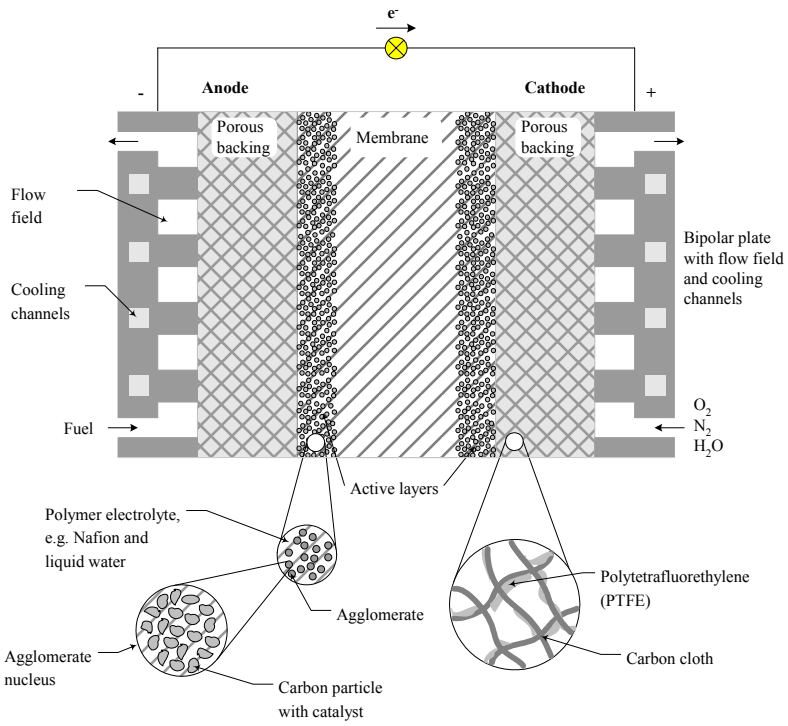

Figure 1. A schematic of a fuel cell.

The basic cell consists of two porous electrodes, termed the anode and the cathode, separated by a proton conducting membrane. The porous electrodes are made of a composite material, containing carbon cloth and a hydrophobic agent, such as polytetrafluorethylene. Each electrode has a thin layer containing an electrocatalyst, such as platinum, that is dispersed on the carbon cloth and is in contact with the membrane, usually a hydrated perfluorinated sulfonic acid polymer. In addition a bipolar plate, essentially graphite into which flow and cooling channels have been machined, is situated adjacent to each electrode. In the course of operation, an oxidant, usually oxygen from air which is either dry or humidified to some extent, is fed at the inlet on the cathode side and transported to the electrolyte/cathode interface; the fuel on the other hand, hydrogen for the PEMFC and methanol for the DMFC, is fed at the anode inlet and is transported to the electrolyte/anode interface. The reactions occurring at these interfaces are then for the PEMFC:

$$2H_2 \rightarrow 4H^+ + 4e^- \qquad \text{at the anode,} \tag{1.1}$$

$$O_2 + 4H^+ + 4e^- \rightarrow 2H_2O \qquad \text{at the cathode,} \tag{1.2}$$

and for the DMFC:

$$CH_3OH + H_2O \rightarrow CO_2 + 6H^+ + 6e^- \qquad \text{at the anode,} \tag{1.3}$$

$$\frac{3}{2}O_2 + 6H^+ + 6e^- \rightarrow 3H_2O \qquad \text{at the cathode.} \tag{1.4}$$

Thus, the protons produced at the anode are transported through the membrane to the cathode, whilst the electrons can drive a load through an external circuit.

During recent years, a number of mathematical models have been developed in an attempt to understand the phenomena occurring in fuel cells. Since a complete fuel cell model would have to consider mass, momentum, species and heat transfer in gas and liquid phases in a three-dimensional geometry, as well as the electrokinetics for the anode and cathode, most models choose to focus on only some of these aspects at a time. This thesis addresses the cathode of the PEMFC and the anode of the DMFC: the cathode of the PEMFC is more limiting due to its sluggish kinetics, as compared to the fast hydrogen oxidation at the anode, provided that the hydrogen feed stream is sufficiently pure to avoid poisoning of the catalyst and sufficiently hydrated; the anode of the DMFC, however, is of interest due to its complex reaction kinetics. Further details of the above are given in the introduction of papers 1 and 3, respectively.

CHAPTER 2

Summary of papers

Paper 1

A chief factor that is thought to limit the performance of polymer electrolyte fuel cells (PEFCs) is the hydrodynamics associated with the cathode. In this paper, a 2-D model for three-component (oxygen, nitrogen, water) gaseous flow in a PEFC cathode is derived, nondimensionalized and analyzed. The fact that the geometry is slender allows the use of a narrow-gap approximation leading to a simplified formulation. Inspite of the highly non-linear coupling between the velocity variables and the mole fractions, an asymptotic treatment of the problem indicates that oxygen consumption and water production can be described rather simply in the classical lubrication theory limit with the reduced Reynolds number as a small parameter. In general, however, the reduced Reynolds number is $O(1)$, requiring a numerical treatment; this is done using the Keller-Box discretization scheme. The analytical and numerical results are compared in the limit mentioned above, and further results are generated for varying inlet velocity and gas composition, channel width and porous backing thickness, pressure and current density. Also, a novel, compact way to present fuel cell performance, which takes into account geometrical, hydrodynamical and electrochemical features, is introduced.

Paper 2

An isothermal three-dimensional model describing mass, momentum and species transfer in the cathode of proton exchange membrane fuel cell has been used to study four different flow distributors: interdigitated, coflow and counterflow channels, and a foam. A quantitative comparison of the results shows that the interdigitated channels can sustain the highest current densities, followed in descending order by the foam, the counterflow and the coflow channels. The foam yields the most uniform current density distribution at higher currents, but also induces the greatest pressure drop.

Paper 3

An isothermal 2-D liquid-phase model for the electrokinetics and the transport of mass, momentum and species in the anode of a DMFC is presented and analysed. The model is developed for the case when the geometry aspect ratio is small, and it is shown that, under realistic operating conditions, a reduced model, which nonetheless still describes all the essential physics of the full model, can be derived. The significant benefits of this approach are that

physical trends become much more apparent than in the full model, and the considerable reduction in the time required to compute numerical solutions - a fact especially useful for wide-ranging parameter studies. Such a study is then performed in terms of the three nondimensional parameters that emerge from the analysis, and we subsequently interpret our results in terms of the dimensional design and operating parameters. In particular, we highlight the effect of these on methanol mass transfer in the flow channel and on the current density. The results indicate the relative importance of mass transfer resistance in both the flow channel and the adjacent porous backing.

CHAPTER 3

Future Work

The one-phase models presented in this thesis will be extended to take the second phase in both fuel cells into account: in the anode of the DMFC, the low solubility of carbon dioxide in the liquid will give rise to bubbles in the liquid phase; for the cathode of the PEMFC, the water vapour will start to condense once its vapour pressure exceeds the saturation pressure.
In contrast to the anode of the DMFC, which we can treat as being two-phase throughout the flow distributor and porous backing, the condensation of liquid water in the cathode of the PEMFC is not known *a priori*, requiring a model, capable of resolving both the gaseous one-phase region and the ensuing two-phase region at sufficiently high water vapour pressures.
By applying scaling arguments, reduced models for both the DMFC and PEMFC will be derived and analysed. Properties, such as velocity fields and local current density distributions, will be investigated.

Acknowledgments

First of all, I would like to thank my supervisor Michael Vynnycky for his valuable advice during the years and for introducing me to scaling and asymptotic analysis.

The cooperation with Joakim Nordlund has been inspiring, for which I am very grateful.

I also wish to thank my collegues, friends and room mates at the Department of Mechanics for providing a very stimulating atmosphere.

The financial support from the Swedish Foundation for Strategic Environmental Research, MISTRA, and from the Swedish National Energy Administration is gratefully acknowledged. The work was done within the framework of the Jungner Center.

Paper 1

Analysis of a Model for Multicomponent Mass Transfer in the Cathode of a Polymer Electrolyte Fuel Cell

Michael Vynnycky and Erik Birgersson

Department of Mechanics, FaxénLaboratoriet, KTH,
SE-100 44, Stockholm, Sweden

Abstract. A chief factor that is thought to limit the performance of polymer electrolyte fuel cells (PEFCs) is the hydrodynamics associated with the cathode. In this paper, a 2-D model for three-component (oxygen, nitrogen, water) gaseous flow in a PEFC cathode is derived, nondimensionalized and analyzed. The fact that the geometry is slender allows the use of a narrow-gap approximation leading to a simplified formulation. Inspite of the highly non-linear coupling between the velocity variables and the mole fractions, an asymptotic treatment of the problem indicates that oxygen consumption and water production can be described rather simply in the classical lubrication theory limit with the reduced Reynolds number as a small parameter. In general, however, the reduced Reynolds number is $O(1)$, requiring a numerical treatment; this is done using the Keller-Box discretization scheme. The analytical and numerical results are compared in the limit mentioned above, and further results are generated for varying inlet velocity and gas composition, channel width and porous backing thickness, pressure and current density. Also, a novel, compact way to present fuel cell performance, which takes into account geometrical, hydrodynamical and electrochemical features, is introduced.

---

1. Introduction

There is at present a rapidly increasing interest in improving the design of fuel cells, that is electrochemical devices that convert the chemical energy of a fuel with an oxidant directly into electricity. Fuel cells have a variety of applications; for instance, the alkaline fuel cell (AFC) was mainly used in space exploration, while the phosphoric acid fuel cell (PAFC), the solid oxide fuel cell (SOFC) and the molten carbonate fuel cell (MCFC) are most suited to stationary applications. Of the several types of fuel cells that are currently under development, perhaps the one that has received the most attention, particularly from the point of view of commercialization in the automotive industry, has been the polymer electrolyte fuel cell (PEFC), also often referred to as the proton-exchange membrane (PEM) fuel cell or the solid polymer fuel cell (SPFC); the merit of this type of fuel cell over others for this particular application is that it can generate the high current densities that are required to power a vehicle, as well as the fact that it operates at comparatively low temperatures (often no higher than 100°C).

A schematic diagram of a PEFC is given in Fig. 1. Essentially, this entails a polymer membrane sandwiched between two gas-diffusion electrodes, which are

each adjacent to flow channels contained within bipolar plates. The oxidant, usually oxygen from air which is either dry or humidified to some extent, is fed in at the inlet of the channel on the cathode side, and is transported to the electrolyte/cathode interface; the fuel on the other hand, normally hydrogen, is fed at the anode channel inlet and is transported to the electrolyte/anode interface.

Both interfaces contain catalyst, often platinum, to accelerate the reactions

$$2H_2 \rightarrow 4H^+ + 4e^- \text{ at the anode,} \tag{1.1}$$

$$O_2 + 4H^+ + 4e^- \rightarrow 2H_2O \text{ at the cathode,} \tag{1.2}$$

in the course of which an electric current is produced to drive a given load.

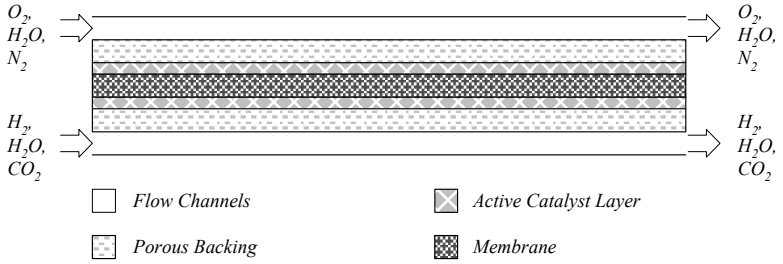

Figure 1. 2-D polymer electrolyte fuel cell.

In particular, the reaction at the cathode also produces both heat and water as by-products, the latter of which may be present throughout the system as either vapor or liquid, or both; the production of the former can lead to temperatures at the catalytic layer in the order of 80-90°C. Optimal fuel cell performance is achieved at typical voltages of around 0.5V at current densities of about 1Acm^{-2}.

Recent years have seen the appearance of mathematical models for some or all of the parts of a typical fuel cell described above. Modelling proves necessary because of an, as yet, incomplete understanding of several important phenomena:

(1) mass transport limitations, that is to ensure that sufficient amounts of oxygen reach the catalytic layer at the cathode in order that a desired current is sustained;
(2) water management, that is to ensure that the water flow in the system is great enough to keep the membrane adequately hydrated, but low enough to prevent flooding;
(3) thermal management, that is to ensure that the cell does not overheat, which may well occur as the result of the heat produced by electrochemical reactions in the catalyst layer.

Since the full problem is highly three-dimensional, non-isothermal, multiphase, multicomponental and most likely time-dependent in nature, numerous simplifications have been made in existing models to ensure some element of

tractability. Perhaps the first one-dimensional models to provide a simplified treatment were developed by Bernardi and Verbrugge [**5, 6**] and Springer, Zawodzinski and Gottesfeld [**40**]; a recent contribution is due to Gurau, Barbir and Lui [**21**]. One-dimensional treatments, whilst they are able to address some aspects of the three issues related to fuel cell performance mentioned above, are not able to address these questions at a local level: that is to say, where oxygen depletion occurs, where there is flooding or inadequate heat removal. Subsequent pseudo-two-dimensional models have tackled some of these issues [**13, 18, 34, 48**], with varying assumptions about the nature of the flow; in these so-called 'along-the-channel' models, the resulting equations are ordinary differential equations with the coordinate along the fuel cell as the independent variable. Most recently, techniques of computational fluid dynamics have been used. Amongst models assuming single-phase gaseous flow, there are 2D isothermal models for the cathode [**14, 49**], 2D isothermal models for the whole cell [**19, 20, 24, 39**], 3D isothermal models for the whole cell [**20, 16**], and 3D non-isothermal models for the whole cell [**7**]; generally speaking, there does not appear to be any experimental evidence that fuel cells are isothermal, although this assumption may indeed be valid for either small cells, or in large cells from which heat is removed at an adequate rate. In addition, two-phase flow at the cathode has also begun to receive attention [**23, 34, 45**].

This paper primarily addresses the first issue of the three given above. In addition, one of the goals is to steer between one-dimensional models and full computational fluid dynamics to derive a 2D formulation that does not sacrifice too many geometrical features, yet on the other hand does not demand excessive computing time either. We focus here on the isothermal, 3-component, gas-phase, two-dimensional flow in a gas channel and adjacent porous gas backing of a PEFC cathode (Fig. 2), although we note that the problem of multicomponent flow is a generic one, appearing not only in both electrodes of a PEFC (the gases are $(O_2,\ N_2,\ H_2O)$ at the cathode and (H_2, CO_2, H_2O) at the anode), but also in other types of fuel cells [**7, 22**]. The geometry is assumed to be slender, as is typically the case in practice.

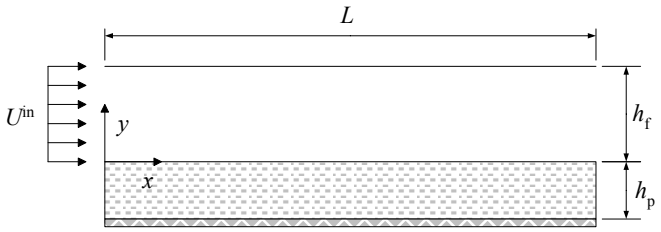

Figure 2. The cathode of a polymer electrolyte fuel cell.

Air, possibly humidifed, is fed in at the inlet at the left (Fig. 2); oxygen that reaches the catalytic layer reacts to produce water vapor, which is transported, along with oxygen and nitrogen, out at the outlet. The approach

used here, however, differs from previous ones, in that we use scaling arguments, nondimensionalization and asymptotics to identify the main governing parameters and, subsequently, to obtain a reduced model. The benefits of this are the availability of closed-form analytical solutions in certain limits, as well as a model that is cheap to compute away from those limits; this feature is important from the point of view of extension to fuel cell stacks where transport in as many as 125 such assemblies may need to be computed (see, e.g. [**29, 30, 31, 42**]). The solution of this benchmark problem is useful from several other points of view:

- as a basis for later work and comparison when two-phase flow is introduced;
- to elucidate features that might not be obvious from simply solving the full equations.

Regarding the second point, it is clear from the majority of cathode studies that the mole fraction of O_2 decreases monotonically along the channel, while the mole fraction of H_2O increases, with the two slopes in some way dependent on physical and operating parameters. Among the results of the present treatment are closed-form expressions for these in certain limits.

The mathematical model is formulated in Section 2. This consists of mass, momentum and species transport equations, and allows for the possibility of varying mixture density, as well as the crossed diffusion of species. A nondimensional analysis of the governing equations in Section 3 provides an indication of the qualitative features one would expect in a multicomponent flow; there are found to be similarities with classical lubrication theory, in view of the slenderness of the geometry, except that the reduced Reynolds number is typically $O(1)$. Furthermore, transport in the porous backing is found, to a reasonable approximation, to be one-dimensional. In Section 4, the first term in an asymptotic series in the reduced Reynolds number is derived: at leading order, the mole fractions are found to be solely a function of the distance along the fuel cell. Section 5 provides a description of a numerical scheme that is subsequently used when the reduced Reynolds number is $O(1)$; the scheme is verified in the lubrication theory limit for which closed form solutions can be secured. Section 6 presents the results. A novel feature which we demonstrate here is that the traditional method for evaluating fuel cell performance, namely through the use of polarization curves, can be supplemented by the concept of a 'polarization surface', whereby the average current density is plotted not as a function of cell potential, but as a function of two dimensionless parameters which depend on cell potential, channel geometry and inlet velocity; consequently, individual polarization curves are then paths along a 'polarization surface'. The implications of these results for a PEFC are also considered, in particular as regards the limitations of the formulation with respect to liquid water formation, and conclusions are drawn in Section 7.

2. Mathematical formulation

2.1. Basics of multicomponent flow. We define the local mass average velocity, $\mathbf{v}$, of an n-component gas by

$$\mathbf{v} = \frac{\sum_{i=1}^{n} \rho_i \mathbf{v}_i}{\sum_{i=1}^{n} \rho_i},$$

where $\mathbf{v}_i$ denotes the velocity of species i with respect to stationary coordinate axes, and ρ_i is the mass concentration (the mass of species i per unit of volume of solution). For each component, the mass flux with respect to a coordinate system fixed in space is given by

$$\mathbf{n}_i = \rho \omega_i \mathbf{v} + \mathbf{j}_i, \quad i = 1, .., n,$$

with

$$\rho = \sum_{i=1}^{n} \rho_i,$$

where ω_i is the mass fraction of species i, given by $\omega_i = \rho_i/\rho$, $\mathbf{j}_i$ is the mass diffusive flux relative to the mass-averaged velocity, and ρ_i denotes the density of species i. If we consider just concentration diffusion for an ideal gas mixture [**8**], we have

$$\mathbf{j}_i = \frac{c^2}{\rho} \sum_{j=1}^{n} M_i M_j D_{ij} \nabla x_j, \quad i = 1, .., n; \tag{2.1}$$

here $(M_i)_{i=1,..,n}$ are the molecular weights, $(D_{ij})_{i,j=1,..,n}$ are the multicomponent diffusion coefficients, $(x_i)_{i=1,..,n}$ is the mole fraction of species i and is given by $x_i = c_i/c$, where c_i is the molar concentration of species i in moles per m^3 ($c_i = \rho_i/M_i$), and

$$c = \sum_{i=1}^{n} c_i.$$

Useful additional identities are $c = \rho/M$ where $M = \sum_{i=1}^{n} x_i M_i$, and a relation between the mass and mole fractions

$$\omega_i = x_i c M_i/\rho.$$

In general, $(D_{ij})_{i,j=1,..,n}$ are strongly dependent on composition, but can be expressed in terms of the Stefan-Maxwell diffusion coefficients, $(\mathcal{D}_{ij})_{i,j=1,..,n}$, which are independent of composition. For a 3-component system, as will be the case here, the relations are of the form [**8**],

$$D_{ij} = \mathcal{D}_{ij} \left\{ 1 + \frac{x_k \left[(M_k/M_j)\, \mathcal{D}_{ik} - \mathcal{D}_{ij} \right]}{x_i \mathcal{D}_{jk} + x_j \mathcal{D}_{ik} + x_k \mathcal{D}_{ij}} \right\}, \quad i, j, k = 1, 2, 3 \ \ (i \neq j)\,. \tag{2.2}$$

$(\mathcal{D}_{ij})_{i,j=1,..,n}$ can in principle be measured experimentally [**8, 41**].

For the mixture density, we use the constitutive relation for an ideal gas,

$$\rho = \frac{pM}{RT}, \tag{2.3}$$

where p is the pressure, T is the temperature and R is the universal gas constant (8.314 $\mathrm{kgm^2s^{-2}mol^{-1}K^{-1}}$). We note, in addition, the possibility that the mixture viscosity, μ_{mix}, will not necessarily be constant either, although we treat it to be so here.

2.2. Channel. Consider the 2-D steady flow of a 3-component gas in a channel of height h_f, adjacent to a porous medium of length L and height h_p (see Figure 2). The equations of continuity of mass and momentum for the mixture are taken as

$$\nabla.\left(\rho\mathbf{v}\right) = 0, \tag{2.4}$$

$$\nabla.\left(\rho\mathbf{v}\otimes\mathbf{v}\right) = -\nabla\left(p+\frac{2\mu}{3}\nabla.\mathbf{v}\right)+\mu\nabla^2\mathbf{v}-\rho g\mathbf{j}, \tag{2.5}$$

where g is the acceleration due to gravity and $\mathbf{j}$ is the unit vector in the positive y-direction; for later use, it is also convenient to define p', the modified pressure, given by

$$p' = p+\frac{2}{3}\mu\nabla.\mathbf{v}.$$

The continuity equation for each of the species,

$$\nabla.\mathbf{n}_i = 0, \quad i=1,..,3 \tag{2.6}$$

can be recast as, for the cathode of a fuel cell, with $n=3$, in the form of two transport equations

$$\nabla.\left(\frac{\rho\mathbf{v}}{M}\left[\begin{array}{c} x_{O_2} \\ x_{H_2O}\end{array}\right]\right) = \nabla.\left(\frac{\rho}{M^2}\mathbf{M}\left[\begin{array}{c}\nabla x_{O_2} \\ \nabla x_{H_2O}\end{array}\right]\right), \tag{2.7}$$

where

$$\mathbf{M} = M_{N_2}\left(\begin{array}{cc} D_{O_2,N_2} & D_{O_2,N_2} \\ D_{H_2O,N_2} & D_{H_2O,N_2}\end{array}\right)-\left(\begin{array}{cc} 0 & M_{H_2O}D_{O_2,H_2O} \\ M_{O_2}D_{H_2O,O_2} & 0\end{array}\right).$$

Here, use has been made of the relation $x_{O_2}+x_{N_2}+x_{H_2O}=1$ to eliminate x_{N_2}, with the diffusion coefficients D_{O_2,H_2O}, $D_{H_2O,O_2}, D_{H_2O,N_2}$ and D_{O_2,N_2} given by (2.38) .

2.3. Porous backing. For the porous region, volume-averaging of (2.1-2.7) along the lines of DeVidts and White [**14**] or Whitaker [**47**] is required. We present this at a moderate level of detail in order to sketch how the transport equations that are normally used, (2.23) below, can be arrived at; fuller details of analogous equations can be found elsewhere [**14, 47**]. First, let B be a quantity (either scalar, vector, or tensor) associated with the gas phase, and let the quantity $\langle B\rangle$ be the local volume (or superficial) average of B,

$$\langle B\rangle \equiv \frac{1}{\mathcal{V}}\int_{\mathcal{V}^{(\mathrm{g})}} B d\mathcal{V}, \tag{2.8}$$

and $\langle B\rangle^{(\mathrm{g})}$ be the intrinsic volume average of B in the gas phase

$$\langle B\rangle^{(\mathrm{g})} \equiv \frac{1}{\mathcal{V}^{(\mathrm{g})}}\int_{\mathcal{V}^{(\mathrm{g})}} B d\mathcal{V}, \tag{2.9}$$

Also, let γ be the porosity, given by $\gamma = \mathcal{V}^{(\mathrm{g})}/\mathcal{V}$. A comparison of equations (2.8) and (2.9) shows that the local and intrinsic volume average for the gas phase is given by

$$\langle B \rangle = \gamma \langle B \rangle^{(\mathrm{g})} . \tag{2.10}$$

Taking the superficial average of (2.4) gives

$$\langle \nabla . (\rho \mathbf{v}) \rangle = 0, \tag{2.11}$$

whilst the superficial average of (2.5) gives (cf. [**46**])

$$\langle \mathbf{v} \rangle = -\frac{\mathbf{K}}{\mu} . \left(\nabla \langle p' \rangle^{(\mathrm{g})} + \langle \rho \rangle^{(\mathrm{g})} g \mathbf{j} \right) + \mathbf{K} . \nabla^2 \left(\frac{\langle \mathbf{v} \rangle}{\gamma} \right) - \mathbf{F} . \langle \mathbf{v} \rangle , \tag{2.12}$$

where $\mathbf{K}$ is the Darcy Law permeability tensor, and $\mathbf{F}$ is the Forchheimer correction tensor. Writing $\widetilde{D}_{ij} = c^2 D_{ij}/\rho$, we have

$$\nabla . \langle c_i \mathbf{v} \rangle + \frac{1}{\mathcal{V}} \int_{A_{gs}} c_i \mathbf{n}_{gs} . \mathbf{v} dA + \sum_{j=1}^{n} M_i M_j \nabla . \left(\left\langle \widetilde{D}_{ij} \right\rangle \left[\nabla \langle x_j \rangle + \frac{1}{\mathcal{V}} \int_{A_{gs}} x_j \mathbf{n}_{gs} dA \right] \right)$$

$$+ \frac{1}{\mathcal{V}} \sum_{j=1}^{n} M_i M_j \widetilde{D}_{ij} \int_{A_{gs}} \mathbf{n}_{gs} . \nabla x_j dA = 0, \tag{2.13}$$

where $\mathbf{n}_{gs}$ represents the unit normal vector pointing from the gas phase to the solid phase, and A_{gs} represents the area of the gas-solid interface contained within $\mathcal{V}$. In the absence of surface reactions and zero normal velocity (passive dispersion), this reduces to

$$\nabla . \langle c_i \mathbf{v} \rangle + \sum_{j=1}^{n} M_i M_j \nabla . \left(\left\langle \widetilde{D}_{ij} \right\rangle \left[\nabla \langle x_j \rangle + \frac{1}{\mathcal{V}} \int_{A_{gs}} x_j \mathbf{n}_{gs} dA \right] \right) = 0, \tag{2.14}$$

and then

$$\nabla . \langle c_i \mathbf{v} \rangle + \sum_{j=1}^{n} M_i M_j \nabla . \left(\widetilde{D}_{ij} \left[\nabla \left(\gamma \langle x_j \rangle^{(\mathrm{g})} \right) + \frac{1}{\mathcal{V}} \int_{A_{gs}} x_j \mathbf{n}_{gs} dA \right] \right) = 0, \tag{2.15}$$

where we have used the fact that $\widetilde{D}_{ij}$ changes slowly with temperature and mole fraction within the representative elementary volume in order to be able to write

$$\nabla . \left\langle \widetilde{D}_{ij} \nabla x_j \right\rangle = \nabla . \left(\widetilde{D}_{ij} \langle \nabla x_j \rangle \right) . \tag{2.16}$$

To ascertain this, we generalise the reasoning given by Whitaker [**47**], as follows. With

$$\begin{aligned} \widetilde{D}_{ij} &= \frac{p D_{ij}}{RTM} \\ &= \frac{p \mathcal{D}_{ij}}{RTM} \left\{ 1 + \frac{x_k \left[(M_k/M_j) \mathcal{D}_{ik} - \mathcal{D}_{ij} \right]}{x_i \mathcal{D}_{jk} + x_j \mathcal{D}_{ik} + x_k \mathcal{D}_{ij}} \right\} , \end{aligned}$$

we require

$$\frac{l_\gamma}{\widetilde{D}_{ij}}\left(\left.\frac{\partial\widetilde{D}_{ij}}{\partial p}\right|_{\langle p\rangle^{(\mathrm{g})}}\nabla\langle p\rangle^{(\mathrm{g})}+\left.\frac{\partial\widetilde{D}_{ij}}{\partial T}\right|_{\langle T\rangle^{(\mathrm{g})}}\nabla\langle T\rangle^{(\mathrm{g})}+\sum_{l=1}^{n}\left.\frac{\partial\widetilde{D}_{ij}}{\partial x_l}\right|_{\langle x_l\rangle^{(\mathrm{g})}}\nabla\langle x_l\rangle^{(\mathrm{g})}\right)\ll 1,$$

where l_γ is the pore length scale. Also, for later use, we need to be able to justify that within the representative elementary volume

$$\begin{aligned}\nabla.\langle c_i\mathbf{v}\rangle &= \nabla.\left(\frac{p}{RT}\langle x_i\mathbf{v}\rangle\right)\\ &= \nabla.\left(\frac{\rho}{M}\langle x_i\mathbf{v}\rangle\right)\\ &= \nabla.\left(\frac{\langle\rho\rangle}{\langle M\rangle}\langle x_i\mathbf{v}\rangle\right);\end{aligned}$$

this would be justified if

$$\frac{l_\gamma}{D_\gamma}\left(\left.\frac{\partial D_\gamma}{\partial p}\right|_{\langle p\rangle^{(\mathrm{g})}}\nabla\langle p\rangle^{(\mathrm{g})}+\left.\frac{\partial D_\gamma}{\partial T}\right|_{\langle T\rangle^{(\mathrm{g})}}\nabla\langle T\rangle^{(\mathrm{g})}\right)\ll 1,$$

where $D_\gamma = p/RT$. Thus, we would require

$$l_\gamma\left(\frac{\nabla\langle p\rangle^{(\mathrm{g})}}{p}-\frac{\nabla\langle T\rangle^{(\mathrm{g})}}{T}\right)\ll 1; \tag{2.17}$$

we verify that this relation is indeed satisfied in Section 3.2.

Now, decomposing according to

$$\phi=\langle\phi\rangle^{(\mathrm{g})}+\phi',$$

where $\phi=(x_j,c_j,\mathbf{v},\rho)$ and the primed quantities denote spatial fluctuations, (2.11) and (2.15) can be shown to become, respectively,

$$\nabla.\left(\langle\rho\rangle^{(\mathrm{g})}\langle\mathbf{v}\rangle\right)=-\nabla.\left(\langle\rho'\mathbf{v}'\rangle\right), \tag{2.18}$$

$$\begin{aligned}\nabla.\left(\frac{\gamma\langle\rho\rangle^{(\mathrm{g})}\langle x_i\rangle^{(\mathrm{g})}\langle\mathbf{v}\rangle^{(\mathrm{g})}}{\langle M\rangle^{(\mathrm{g})}}\right)&\\ +\sum_{j=1}^{n}M_iM_j\nabla.\left(\widetilde{D}_{ij}\left[\nabla\left(\gamma\langle x_j\rangle^{(\mathrm{g})}\right)+\frac{1}{\mathcal{V}}\int_{A_{gs}}x_j'\mathbf{n}_{gs}dA\right]\right)&\\ -\nabla.\left(\frac{\langle\rho\rangle^{(\mathrm{g})}}{\langle M\rangle^{(\mathrm{g})}}\langle\mathbf{v}'x_i'\rangle\right)=0,&\end{aligned} \tag{2.19}$$

where we again use analysis due to Whitaker [**47**] (cf. pp. 14-20). To keep the ongoing discussion simple, we assume henceforth that γ is constant. Eventually,

we arrive at

$$\nabla.\left(\frac{\gamma\left\langle\rho\right\rangle^{(\mathrm{g})}\left\langle x_i\right\rangle^{(\mathrm{g})}\left\langle\mathbf{v}\right\rangle^{(\mathrm{g})}}{\left\langle M\right\rangle^{(\mathrm{g})}}\right)+\sum_{j=1}^{n}M_iM_j\nabla.\left(\left[\mathbf{D}_{ij}^{\mathrm{eff}}+\gamma\mathbf{D}_j^{\mathrm{hyd}}\delta_{ij}\right]\nabla\left\langle x_j\right\rangle^{(\mathrm{g})}\right)=0, \tag{2.20}$$

where $\mathbf{D}_{ij}^{\mathrm{eff}}$ is an effective diffusivity tensor given by

$$\mathbf{D}_{ij}^{\mathrm{eff}}=\gamma\widetilde{D}_{ij}\left(1+\frac{1}{\mathcal{V}^{(\mathrm{g})}}\int_{A_{gs}}\mathbf{n}_{gs}\mathbf{b}_g dA\right),$$

and δ_{ij} is the Kronecker delta; here, $\mathbf{b}_g$ is referred to as the closure variable and is found from the so-called closure problem. $\mathbf{D}_j^{\mathrm{hyd}}$ is called the hydrodynamic dispersion tensor and is defined by

$$\mathbf{D}_j^{\mathrm{hyd}}:=-\frac{\left\langle\rho\right\rangle^{(\mathrm{g})}}{\left\langle M\right\rangle^{(\mathrm{g})}}\left\langle\mathbf{v}'x_j'\right\rangle^{(\mathrm{g})}.$$

For gas diffusion electrodes, the following is often used [**3, 5, 6, 49**]:

$$\mathbf{D}_{ij}^{\mathrm{eff}}=\widetilde{D}_{ij}\gamma^{\frac{3}{2}};$$

this would imply

$$\left(1+\frac{1}{\mathcal{V}^{(\mathrm{g})}}\int_{A_{gs}}\mathbf{n}_{gs}\mathbf{b}_g dA\right)=\gamma^{\frac{1}{2}}.$$

For the cathode, with $i=O_2, N_2$ and H_2O, we have in more expedient form, on assuming the permeability to be isotropic and constant, and neglecting the Forchheimer correction term in (2.12) and dispersion terms in (2.18) and (2.19) (see Section 3.4),

$$\nabla.\left(\left\langle\rho\right\rangle^{(\mathrm{g})}\left\langle\mathbf{v}\right\rangle\right) = 0, \tag{2.21}$$

$$\left\langle\mathbf{v}\right\rangle = -\frac{\kappa}{\mu}\left(\nabla\left\langle p'\right\rangle^{(\mathrm{g})}+\left\langle\rho\right\rangle^{(\mathrm{g})}g\mathbf{j}\right)+\frac{\kappa}{\gamma}\nabla^2\left\langle\mathbf{v}\right\rangle, \tag{2.22}$$

$$\nabla.\left(\frac{\left\langle\rho\right\rangle^{(\mathrm{g})}\left\langle\mathbf{v}\right\rangle}{\left\langle M\right\rangle^{(\mathrm{g})}}\begin{bmatrix}\left\langle x_{O_2}\right\rangle^{(\mathrm{g})}\\ \left\langle x_{H_2O}\right\rangle^{(\mathrm{g})}\end{bmatrix}\right)$$
$$=\nabla.\left(\frac{\gamma^{\frac{3}{2}}\left\langle\rho\right\rangle^{(\mathrm{g})}}{\left(\left\langle M\right\rangle^{(\mathrm{g})}\right)^2}\left\langle\mathbf{M}\right\rangle^{(\mathrm{g})}\begin{bmatrix}\nabla\left\langle x_{O_2}\right\rangle^{(\mathrm{g})}\\ \nabla\left\langle x_{H_2O}\right\rangle^{(\mathrm{g})}\end{bmatrix}\right), \tag{2.23}$$

where

$$\left\langle\mathbf{M}\right\rangle^{(\mathrm{g})} = M_{N_2}\begin{pmatrix}\left\langle D_{O_2,N_2}\right\rangle^{(\mathrm{g})} & \left\langle D_{O_2,N_2}\right\rangle^{(\mathrm{g})}\\ \left\langle D_{H_2O,N_2}\right\rangle^{(\mathrm{g})} & \left\langle D_{H_2O,N_2}\right\rangle^{(\mathrm{g})}\end{pmatrix}$$
$$-\begin{pmatrix}0 & M_{H_2O}\left\langle D_{O_2,H_2O}\right\rangle^{(\mathrm{g})}\\ M_{O_2}\left\langle D_{H_2O,O_2}\right\rangle^{(\mathrm{g})} & 0\end{pmatrix},$$

with

$$\langle D_{ij}\rangle^{(\mathrm{g})} = \mathcal{D}_{ij}\left\{1 + \frac{\langle x_k\rangle^{(\mathrm{g})}\left[(M_k/M_j)\,\mathcal{D}_{ik} - \mathcal{D}_{ij}\right]}{\langle x_i\rangle^{(\mathrm{g})}\,\mathcal{D}_{jk} + \langle x_j\rangle^{(\mathrm{g})}\,\mathcal{D}_{ik} + \langle x_k\rangle^{(\mathrm{g})}\,\mathcal{D}_{ij}}\right\};$$

(2.21)-(2.23) are then akin to the governing equations for the porous backing used by most authors, although with more attention having been paid here to the distinction between intrinsic and superficial variables, the possibility of non-constant diffusion coefficients and the inclusion of crossed diffusion terms.

2.4. Boundary conditions.

2.4.1. *Inlet, outlet, upper wall, vertical walls.* For boundary conditions in the channel, we prescribe inlet velocity and gas composition at $x = 0$, $0 \le y \le h_f$, so that

$$u = U^{in}, \quad v = 0, \quad x_{O_2} = x^{in}_{O_2}, \quad x_{H_2O} = x^{in}_{H_2O}, \tag{2.24}$$

where $\mathbf{v} = (u, v)$. At the upper channel wall ($0 \le x \le L$, $y = h_f$), there is no slip, no normal flow and no componental flux, so that

$$u = v = \frac{\partial x_{O_2}}{\partial y} = \frac{\partial x_{H_2O}}{\partial y} = 0. \tag{2.25}$$

At the outlet at $x = L, 0 \le y \le h_f$, we have constant pressure and no diffusive componental flux, so that

$$p = p^{out}, \quad \frac{\partial v}{\partial x} = \frac{\partial x_{O_2}}{\partial x} = \frac{\partial x_{H_2O}}{\partial x} = 0. \tag{2.26}$$

At the vertical walls of the porous electrode ($x = 0, L, -h_p \le y \le 0$), we prescribe no normal flow, no tangential shear and no mass flux for the gas components, so that

$$\langle u\rangle = \frac{\partial \langle v\rangle}{\partial x} = \frac{\partial \langle x_{O_2}\rangle^{(\mathrm{g})}}{\partial x} = \frac{\partial \langle x_{H_2O}\rangle^{(\mathrm{g})}}{\partial x} = 0, \tag{2.27}$$

where $\langle \mathbf{v}\rangle = (\langle u\rangle, \langle v\rangle)$.

2.4.2. *Channel/porous backing interface.* In addition, matching conditions are required for the fluid-porous interface at $y = 0$, $0 \le x \le L$. The conditions for continuity of normal velocity and normal stress are given respectively as

$$v = \langle v\rangle, \tag{2.28}$$

$$p - \mu\frac{\partial v}{\partial y} = \langle p\rangle^{(\mathrm{g})} - \mu_{eff}\frac{\partial \langle v\rangle}{\partial y}, \tag{2.29}$$

where $\mu_{eff}\,(= \mu/\gamma)$ is termed the effective viscosity of the porous medium. The remaining two conditions that are required have been the subject of longstanding debate ever since the work of Beavers and Joseph [**4**]; a recent contribution is due to Jäger and Mikelić [**25**]. A summary of possible options for the momentum equation is given by Alazmi and Vafai [**1**], of which the most relevant for this application, and indeed most consistent in view of our use of the full

Navier-Stokes equations for the fluid and a Darcy/Brinkman/Forchheimer formulation for the porous medium, is one due to Ochoa-Tapia and Whitaker [**35**] when inertial effects are important:

$$u = \langle u \rangle , \tag{2.30}$$

$$\frac{\mu}{\gamma}\frac{\partial \langle u \rangle}{\partial y} - \mu\frac{\partial u}{\partial y} = \frac{\beta_1 \mu}{\kappa^{\frac{1}{2}}}u + \beta_2 \rho u^2, \tag{2.31}$$

respectively. Here, β_1 and β_2 are $O(1)$ constants which would need to be determined experimentally, although it turns out here that the leading order problem is dictated more by (2.30) than by (2.31).

Finally, analogous volume-averaging techniques at the interface to those used for heat transfer by [**36**] are required for the mole fraction transport equations. We do not pursue the details, but simply assume the point values for the mole fractions of O_2 and H_2O in the channel to be equal to their intrinsic values in the porous backing, so that

$$\langle x_{O_2} \rangle^{(\mathrm{g})} = x_{O_2}, \quad \langle x_{H_2O} \rangle^{(\mathrm{g})} = x_{H_2O}, \text{ at } y = 0, \tag{2.32}$$

and in addition that the point values for the mole fraction fluxes of O_2 and H_2O are equal to their superficial values in the porous medium, so that,

$$\mathbf{n}_{O_2}.\mathbf{n} = \langle \mathbf{n}_{O_2}.\mathbf{n} \rangle , \quad \mathbf{n}_{H_2O}.\mathbf{n} = \langle \mathbf{n}_{H_2O}.\mathbf{n} \rangle ;$$

using (2.28) and (2.32), we arrive at

$$\gamma^{\frac{3}{2}}\frac{\partial}{\partial y}\begin{bmatrix} \langle x_{O_2} \rangle^{(\mathrm{g})} \\ \langle x_{H_2O} \rangle^{(\mathrm{g})} \end{bmatrix} = \frac{\partial}{\partial y}\begin{bmatrix} x_{O_2} \\ x_{H_2O} \end{bmatrix}, \tag{2.33}$$

respectively.

2.4.3. *Catalyst/porous backing interface.* At $y = -h_f$, we would expect $\langle u \rangle , \langle v \rangle , \langle x_{O_2} \rangle^{(\mathrm{g})}$ and $\langle x_{H_2O} \rangle^{(\mathrm{g})}$ to match to their counterparts in the catalytic layer, although naturally this approach would require us to model the catalyst layer, and then by extension the membrane and the corresponding regions on the anode side. This has been done to varying degrees by various authors [**5, 6, 20, 18, 19, 20, 21, 24, 34, 7, 39, 40**]. An alternative approach, often adopted when the flow field in the porous backing and gas channels rather than the electrochemistry in the catalyst and the membrane is of interest [**14, 33, 49, 45**], is to prescribe a current density, I, at this interface. Using Faraday's Law, the superficial mass flux of oxygen is given as a function of current density, so that

$$\langle \mathbf{n}_{O_2}.\mathbf{n} \rangle = -\frac{M_{O_2} I}{4F}, \tag{2.34}$$

where F is the Faraday constant. The corresponding expression for water is then taken to be

$$\langle \mathbf{n}_{H_2O}.\mathbf{n} \rangle = \frac{M_{H_2O}(1 + 2\alpha)I}{2F}, \tag{2.35}$$

where α is a parameter accounting for the water transport by electro-osmosis in the membrane; typical values encountered in the literature are α =0.3 [**45**] and

$0.5 \leq \alpha \leq 1.7$ [**33, 48, 49**]. Furthermore, since nitrogen does not participate in the reaction at the catalyst layer,

$$\langle \mathbf{n}_{N_2}.\mathbf{n} \rangle = 0. \tag{2.36}$$

This leads to the following boundary conditions for $\langle v \rangle$, $\langle x_{O_2} \rangle^{(\mathrm{g})}$ and $\langle x_{H_2O} \rangle^{(\mathrm{g})}$:

$$\langle \rho \rangle^{(\mathrm{g})} \langle v \rangle = \frac{I}{4F} \left(2(1+2\alpha) M_{H_2O} - M_{O_2} \right), \tag{2.37}$$

and

$$\frac{\langle \rho \rangle^{(\mathrm{g})} \langle v \rangle}{\langle M \rangle^{(\mathrm{g})}} \begin{bmatrix} \langle x_{O_2} \rangle^{(\mathrm{g})} \\ \langle x_{H_2O} \rangle^{(\mathrm{g})} \end{bmatrix} - \frac{\gamma^{\frac{3}{2}} \langle \rho \rangle^{(\mathrm{g})}}{\left(\langle M \rangle^{(\mathrm{g})} \right)^2} \bar{\mathbf{M}} \frac{\partial}{\partial y} \begin{bmatrix} \langle x_{O_2} \rangle^{(\mathrm{g})} \\ \langle x_{H_2O} \rangle^{(\mathrm{g})} \end{bmatrix} = \frac{I}{4F} \begin{bmatrix} -1 \\ 2(1+2\alpha) \end{bmatrix}.$$

3. Analysis

3.1. Nondimensionalization. Writing

$$\tilde{x} = \frac{x}{L}, \quad \tilde{y} = \frac{y}{L}, \quad \widetilde{\mathbf{v}} = \frac{\mathbf{v}}{U^{in}}, \quad \langle \widetilde{\mathbf{v}} \rangle = \frac{\langle \mathbf{v} \rangle}{U^{in}}, \; \tilde{\rho} = \frac{\rho}{[\rho]}, \; \langle \widetilde{\rho} \rangle^{(\mathrm{g})} = \frac{\langle \rho \rangle^{(\mathrm{g})}}{[\rho]},$$

$$\tilde{p} = \frac{p - p^{out}}{[\rho] \left(U^{in} \right)^2}, \; \langle \tilde{p} \rangle^{(\mathrm{g})} = \frac{\langle p \rangle^{(\mathrm{g})} - p^{out}}{[\rho] \left(U^{in} \right)^2}, \; \tilde{p}' = \frac{p' - p^{out}}{[\rho] \left(U^{in} \right)^2}, \; \langle \tilde{p}' \rangle^{(\mathrm{g})} = \frac{\langle p' \rangle^{(\mathrm{g})} - p^{out}}{[\rho] \left(U^{in} \right)^2},$$

$$\widetilde{I} = \frac{I}{[I]}, \quad \mathcal{M} = \frac{M}{[M]}, \; \langle \mathcal{M} \rangle^{(\mathrm{g})} = \frac{\langle M \rangle^{(\mathrm{g})}}{[M]}, \quad \tilde{c} = \frac{c}{[\rho] / [M]},$$

$$\mathcal{M}_i = \frac{M_i}{[M]}, i = 1, .., 3, \quad \tilde{D}_{ij} = \frac{D_{ij}}{[D]}, \; i, j = 1, .., 3, \quad \tilde{D}_{ij}^{eff} = \frac{D_{ij}^{eff}}{[D]}, \; i, j = 1, .., 3,$$

$$Re = \frac{[\rho] U^{in} L}{\mu}, \quad Sc = \frac{\mu}{[\rho] [D]}, \quad Da = \frac{\kappa}{L^2}, \quad Fr = \frac{U^2}{gL},$$

$$\tilde{\mathbf{M}} = \frac{\mathbf{M}}{[M] [D]}, \; \left\langle \tilde{\mathbf{M}} \right\rangle^{(\mathrm{g})} = \frac{\langle \mathbf{M} \rangle^{(\mathrm{g})}}{[M] [D]},$$

where $[\rho]$ is a density scale, $[D]$ is a diffusion scale, $[I]$ is a current density scale and $[M]$ is a molecular weight scale (all to be either determined or specified shortly), and Re, Sc, Da and Fr are the Reynolds, Schmidt, Darcy and Froude numbers, respectively, we drop the tildes and arrive at the following nondimensionalised forms. For the channel ($0 \leq x \leq 1$, $0 \leq y \leq 1$),

$$\nabla . (\rho \mathbf{v}) = 0, \tag{3.1}$$

$$\nabla . (\rho \mathbf{v} \otimes \mathbf{v}) = -\nabla \left(p + \frac{2\delta^2}{3} \nabla . \mathbf{v} \right) + \delta^2 \nabla^2 \mathbf{v} - Fr^{-1} \rho \mathbf{j}, \tag{3.2}$$

$$\nabla . \left(\frac{\rho \mathbf{v}}{\mathcal{M}} \begin{bmatrix} x_{O_2} \\ x_{H_2O} \end{bmatrix} \right) = \frac{\delta^2}{Sc} \nabla . \left(\frac{\rho}{\mathcal{M}^2} \mathbf{M} \begin{bmatrix} \nabla x_{O_2} \\ \nabla x_{H_2O} \end{bmatrix} \right), \tag{3.3}$$

where $\delta^2 = Re^{-1}$, and for the porous medium ($0 \leq x \leq 1$, $-h_p/L \leq y \leq 0$),

$$\begin{aligned} \nabla.\left(\langle\rho\rangle^{(\mathrm{g})}\langle\mathbf{v}\rangle\right) &= 0, \\ \frac{\delta^2}{\epsilon^2}\langle\mathbf{v}\rangle &= -\nabla\langle p'\rangle^{(\mathrm{g})} + \delta^2\nabla^2\left(\frac{\langle\mathbf{v}\rangle}{\gamma}\right) - Fr^{-1}\langle\rho\rangle^{(\mathrm{g})}\mathbf{j}, \end{aligned} \tag{3.4}$$

$$\begin{aligned} &\nabla.\left(\frac{\langle\rho\rangle^{(\mathrm{g})}\langle\mathbf{v}\rangle}{\langle\mathcal{M}\rangle^{(\mathrm{g})}}\begin{bmatrix}\langle x_{O_2}\rangle^{(\mathrm{g})}\\ \langle x_{H_2O}\rangle^{(\mathrm{g})}\end{bmatrix}\right) \\ &\qquad = \frac{\delta^2}{Sc}\nabla.\left(\gamma^{\frac{3}{2}}\frac{\langle\rho\rangle^{(\mathrm{g})}}{\left(\langle\mathcal{M}\rangle^{(\mathrm{g})}\right)^2}\langle\mathbf{M}\rangle^{(\mathrm{g})}\begin{bmatrix}\nabla\langle x_{O_2}\rangle^{(\mathrm{g})}\\ \nabla\langle x_{H_2O}\rangle^{(\mathrm{g})}\end{bmatrix}\right), \end{aligned} \tag{3.5}$$

where $\epsilon^2 = Da$. The boundary conditions are now

$$u = 1, \quad v = 0, \quad x_{O_2} = x_{O_2}^{in}, \quad x_{H_2O} = x_{H_2O}^{in}, \quad \text{at} \quad x = 0, \quad 0 \leq y \leq h_f/L; \tag{3.6}$$

$$u = v = \frac{\partial x_{O_2}}{\partial y} = \frac{\partial x_{H_2O}}{\partial y} = 0, \quad \text{at} \quad 0 \leq x \leq 1, \quad y = h_f/L; \tag{3.7}$$

$$p = 0, \quad \frac{\partial v}{\partial x} = \frac{\partial x_{O_2}}{\partial x} = \frac{\partial x_{H_2O}}{\partial x} = 0, \quad \text{at} \quad x = 1, \quad 0 \leq y \leq h_f/L; \tag{3.8}$$

$$\langle u\rangle = \frac{\partial\langle v\rangle}{\partial x} = \frac{\partial\langle x_{O_2}\rangle^{(\mathrm{g})}}{\partial x} = \frac{\partial\langle x_{H_2O}\rangle^{(\mathrm{g})}}{\partial x} = 0, \text{ at } x = 0, 1, \quad -h_p/L \leq y \leq 0. \tag{3.9}$$

The boundary conditions for $0 \leq x \leq 1$, $y = -h_p/L$ are now:

$$\langle u\rangle = 0, \quad \langle\rho\rangle^{(\mathrm{g})}\langle v\rangle = \Lambda\left\{\frac{I}{4}\left(2(1+2\alpha)\mathcal{M}_{H_2O} - \mathcal{M}_{O_2}\right)\right\}, \tag{3.10}$$

$$\begin{aligned} &\frac{\langle\rho\rangle^{(\mathrm{g})}\langle\mathbf{v}\rangle}{\langle\mathcal{M}\rangle^{(\mathrm{g})}}\begin{bmatrix}\langle x_{O_2}\rangle^{(\mathrm{g})}\\ \langle x_{H_2O}\rangle^{(\mathrm{g})}\end{bmatrix} - \frac{\delta^2\gamma^{\frac{3}{2}}\langle\rho\rangle^{(\mathrm{g})}}{Sc\left(\langle\mathcal{M}\rangle^{(\mathrm{g})}\right)^2}\langle\mathbf{M}\rangle^{(\mathrm{g})}\frac{\partial}{\partial y}\begin{bmatrix}\langle x_{O_2}\rangle^{(\mathrm{g})}\\ \langle x_{H_2O}\rangle^{(\mathrm{g})}\end{bmatrix} \\ &\qquad = \frac{\Lambda I}{4}\begin{pmatrix}-1\\ 2(1+2\alpha)\end{pmatrix}, \end{aligned} \tag{3.11}$$

where $\Lambda = [I][M]/FU^{in}[\rho]$. Finally, the boundary conditions along the fluid-porous interface on $y = 0$ reduce to

$$v = \langle v\rangle, \tag{3.12}$$

$$p - \delta^2\frac{\partial v}{\partial y} = \langle p\rangle^{(\mathrm{g})} - \delta^2\frac{\partial\langle v\rangle}{\partial y}, \tag{3.13}$$

$$u = \langle u\rangle, \tag{3.14}$$

$$\frac{1}{\gamma}\frac{\partial\langle u\rangle}{\partial y} - \frac{\partial u}{\partial y} = \left(\frac{\beta_1}{\varepsilon}\right)u + \left(\frac{\beta_2}{\delta^2}\right)\rho u^2. \tag{3.15}$$

and

$$\langle x_{O_2}\rangle^{(\mathrm{g})} = x_{O_2}, \quad \langle x_{H_2O}\rangle^{(\mathrm{g})} = x_{H_2O}, \tag{3.16}$$

$$\gamma^{\frac{3}{2}}\frac{\partial}{\partial y}\begin{bmatrix} \langle x_{O_2}\rangle^{(g)} \\ \langle x_{H_2O}\rangle^{(g)} \end{bmatrix} = \frac{\partial}{\partial y}\begin{bmatrix} x_{O_2} \\ x_{H_2O} \end{bmatrix}. \tag{3.17}$$

3.2. Parameters. Typically, $U^{in} \sim 1$ ms^{-1}, $h_f \sim 10^{-3}$ m, $h_p \sim 3\times 10^{-4}$ m, $L \geq 10^{-2}$ m, $[I] \sim 10^4$ Am^{-2}, $p^{out} \sim 1$ atm $\sim 10^5$kgm^{-1}s^{-2}, $T \sim 300-350$ K, $0.1 \leq \gamma \leq 0.5$, $0.3 \leq \alpha \leq 1.7$, $\mu \sim O(10^{-5})$ kgm$^{-1}s^{-1}$. In addition, $M_{O_2} = 0.032$ kgmol^{-1}, $M_{H_2O} = 0.018$ kgmol^{-1}, $M_{N_2} = 0.028$ kgmol^{-1}, $F = 96487$ Asmol^{-1}, from which we note that $M_{min} \leq M \leq M_{max}$, where

$$\begin{aligned} M_{min} &= M|_{x_{H_2O}=1, x_{O_2}=0} = 0.018 \text{ kgmol}^{-1}, \\ M_{max} &= M|_{x_{H_2O}=0, x_{O_2}=1} = 0.032 \text{ kgmol}^{-1}. \end{aligned}$$

Further, we use the constitutive relation for an ideal gas in order to obtain the density scale $[\rho]$; with $p \sim p^{out}$, we have $\rho \sim 1$ kgm^{-3}, so that $[\rho] \sim 1$ kgm^{-3} seems appropriate. For $[D]$, we take $O\left(10^{-5}\right)$ m^{2}s^{-1} from available literature, e.g. [**5, 6**]. Note also that the relation (2.17) is satisfied, since the smallest length on the macroscale in the porous backing, h_p, is still much larger than the scale for l_γ, $10^{-5}-10^{-6}$m, suggested by the electrochemical literature [**17, 43**].

Thence, for the nondimensional parameters Re, Sc, Da, Fr, Λ, we arrive at

$$Re \sim 10^4, \quad Sc \sim 1, \quad Da \leq 10^{-6}, \quad Fr \sim 1, \quad \Lambda \leq 10^{-2},$$

so that $\delta \sim 10^{-2}$ and $\epsilon \leq 10^{-3}$. We note here that some of these parameters have been encountered before in conjunction with the modelling of flow in solid oxide fuel cells [**7, 11**]: in particular, the Reynolds number, *Re*, which represents the ratio of inertial to viscous forces, and the product Schmidt *ReSc*, which is the ratio of gas flow rate to the rate of diffusion (in fact *ReSc* in our formulation corresponds to the parameter Q in [**7, 11**]). Furthermore, the parameter Λ is a measure of the ratio of the electrochemical flux of oxygen to the gas flow rate, and thus corresponds to the combination E/Q in [**7, 11**]. For compeleteness, we mention that the Froude number, *Fr,* is the ratio of inertial to gravitational forces, whereas the Darcy number, *Da*, is the ratio of the porous medium permeability to the square of the length scale of the entire geometry.

3.3. Narrow-gap approximation. Typically, $h_f/L, h_p/L \ll 1$, which leads us to further rescaling as follows. Writing

$$\begin{aligned} X &= x, \quad Y = \frac{y}{\sigma}, \quad U = u, \; V = \frac{v}{\sigma}, \quad \langle U\rangle = \langle u\rangle\,, \quad \langle V\rangle = \frac{\langle v\rangle}{\sigma}, \\ P &= p, \; P' = p', \quad \langle P\rangle = \langle p\rangle\,, \quad \langle P'\rangle = \langle p'\rangle\,, \end{aligned}$$

where $\sigma = h_f/L$, we simplify further by neglecting terms in $O(\sigma)$ or lower, although we retain for the time being terms which contain multiples of σ and the other dimensionless parameters. We introduce the dimensionless parameters Δ, Σ and Ω, given by

$$\Delta = \delta^2/\sigma^2, \; \Sigma = \sigma^2/\varepsilon, \; \Omega = \Lambda/\sigma,$$

and that an alternative expression for Δ is $\Delta = \left(Re\sigma^2\right)^{-1}$, i.e. the reciprocal of the reduced Reynolds number. We have now, for the channel,

$$\frac{\partial}{\partial X}\left(\rho U\right) + \frac{\partial}{\partial Y}\left(\rho V\right) = 0, \tag{3.18}$$

$$\rho\left(U\frac{\partial U}{\partial X} + V\frac{\partial U}{\partial Y}\right) = -\frac{\partial P'}{\partial X} + \Delta\frac{\partial^2 U}{\partial Y^2}, \tag{3.19}$$

$$0 = -\frac{\partial P'}{\partial Y}, \tag{3.20}$$

$$\left(\rho U\frac{\partial}{\partial X} + \rho V\frac{\partial}{\partial Y}\right)\left[\begin{array}{cc}1 & x_{O_2}\\ \mathcal{M} & x_{H_2O}\end{array}\right] = \frac{\Delta}{Sc}\frac{\partial}{\partial Y}\left(\frac{\rho}{\mathcal{M}^2}\mathbf{M}\frac{\partial}{\partial Y}\left[\begin{array}{c}x_{O_2}\\ x_{H_2O}\end{array}\right]\right), \tag{3.21}$$

and for the porous medium,

$$0 = \frac{\partial}{\partial X}\left(\langle\rho\rangle^{(\mathrm{g})}\langle U\rangle\right) + \frac{\partial}{\partial Y}\left(\langle\rho\rangle^{(\mathrm{g})}\langle V\rangle\right), \tag{3.22}$$

$$\langle U\rangle = -\frac{\epsilon}{\Delta\Sigma}\frac{\partial\langle P'\rangle^{(\mathrm{g})}}{\partial X} + \frac{\varepsilon}{\Sigma\gamma}\frac{\partial^2\langle U\rangle}{\partial Y^2}, \tag{3.23}$$

$$\langle V\rangle = -\frac{1}{\Delta\Sigma^2}\frac{\partial\langle P'\rangle^{(\mathrm{g})}}{\partial Y} + \frac{\varepsilon}{\Sigma\gamma}\frac{\partial^2\langle V\rangle}{\partial Y^2}, \tag{3.24}$$

$$\left(\langle\rho\rangle^{(\mathrm{g})}\langle U\rangle\frac{\partial}{\partial X} + \langle\rho\rangle^{(\mathrm{g})}\langle V\rangle\frac{\partial}{\partial Y}\right)\left(\frac{1}{\langle\mathcal{M}\rangle^{(\mathrm{g})}}\left[\begin{array}{c}\langle x_{O_2}\rangle^{(\mathrm{g})}\\ \langle x_{H_2O}\rangle^{(\mathrm{g})}\end{array}\right]\right)$$
$$= \frac{\Delta}{Sc}\frac{\partial}{\partial Y}\left(\frac{\gamma^{\frac{3}{2}}\langle\rho\rangle^{(\mathrm{g})}}{\left(\langle\mathcal{M}\rangle^{(\mathrm{g})}\right)^2}\langle\mathbf{M}\rangle^{(\mathrm{g})}\frac{\partial}{\partial Y}\left[\begin{array}{c}\langle x_{O_2}\rangle^{(\mathrm{g})}\\ \langle x_{H_2O}\rangle^{(\mathrm{g})}\end{array}\right]\right). \tag{3.25}$$

Note also that

$$P' = P + O\left(\delta^2\right), \quad \langle P'\rangle^{(\mathrm{g})} = \langle P\rangle^{(\mathrm{g})} + O\left(\delta^2\right),$$

and since $\delta^2 \ll 1$, henceforth, we use the actual pressure rather than the modified pressure. In addition, the gravitational terms in (3.20) and (3.24) are $O\left(Fr^{-1}\sigma\right)$ and have therefore been dropped. The boundary conditions are: for $0 \le X \le 1, Y = 1$,

$$U = V = \frac{\partial x_{O_2}}{\partial Y} = \frac{\partial x_{H_2O}}{\partial Y} = 0; \tag{3.26}$$

for $0 \le X \le 1, \quad Y = 0$,

$$V = \langle V\rangle, \tag{3.27}$$

$$P = \langle P\rangle^{(\mathrm{g})}, \tag{3.28}$$

$$U = \langle U\rangle, \tag{3.29}$$

$$\frac{1}{\gamma}\frac{\partial\langle U\rangle}{\partial Y} - \frac{\partial U}{\partial Y} = \left(\frac{\beta_1\sigma}{\varepsilon}\right)U + \left(\frac{\beta_2\sigma}{\delta^2}\right)\rho U^2, \tag{3.30}$$

$$\langle x_{O_2}\rangle^{(\mathrm{g})} = x_{O_2}, \quad \langle x_{H_2O}\rangle^{(\mathrm{g})} = x_{H_2O}, \tag{3.31}$$

$$\gamma^{\frac{3}{2}}\frac{\partial}{\partial Y}\begin{bmatrix}\langle x_{O_2}\rangle^{(\mathrm{g})}\\ \langle x_{H_2O}\rangle^{(\mathrm{g})}\end{bmatrix}=\frac{\partial}{\partial Y}\begin{bmatrix}x_{O_2}\\ x_{H_2O}\end{bmatrix}; \tag{3.32}$$

for $0\le X\le 1,\quad Y=-\mathcal{H}\,(=h_p/h_f)$,

$$\langle U\rangle=0,\quad \langle\rho\rangle^{(\mathrm{g})}\langle V\rangle=\Omega\left\{\frac{I}{4}\left(2(1+2\alpha)\mathcal{M}_{H_2O}-\mathcal{M}_{O_2}\right)\right\}, \tag{3.33}$$

$$\frac{\langle\rho\rangle^{(\mathrm{g})}\langle V\rangle}{\langle\mathcal{M}\rangle^{(\mathrm{g})}}\begin{bmatrix}\langle x_{O_2}\rangle^{(\mathrm{g})}\\ \langle x_{H_2O}\rangle^{(\mathrm{g})}\end{bmatrix}-\frac{\Delta\gamma^{\frac{3}{2}}\langle\rho\rangle^{(\mathrm{g})}}{Sc\left(\langle\mathcal{M}\rangle^{(\mathrm{g})}\right)^2}\langle\mathbf{M}\rangle^{(\mathrm{g})}\frac{\partial}{\partial Y}\begin{bmatrix}\langle x_{O_2}\rangle^{(\mathrm{g})}\\ \langle x_{H_2O}\rangle^{(\mathrm{g})}\end{bmatrix}$$
$$=\frac{\Omega I}{4}\begin{bmatrix}-1\\ 2(1+2\alpha)\end{bmatrix}, \tag{3.34}$$

The neglect of streamwise diffusion terms will of course imply that not all of the original boundary conditions at $X=0$ and 1 in this reduced formulation can be satisfied and those terms would need to be reinstated for $X\sim O(\sigma)$ and $1-X\sim O(\sigma)$. This is beyond the scope of interest here and for a consistent formulation we simply retain

$$U=1,\quad x_{O_2}=x_{O_2}^{in},\quad x_{H_2O}=x_{H_2O}^{in},\quad \text{at}\quad X=0,\quad 0\le Y\le 1; \tag{3.35}$$

$$\langle U\rangle=\frac{\partial\langle x_{O_2}\rangle^{(\mathrm{g})}}{\partial X}=\frac{\partial\langle x_{H_2O}\rangle^{(\mathrm{g})}}{\partial X}=0,\quad \text{at}\quad X=0,\quad -\mathcal{H}\le Y\le 0. \tag{3.36}$$

For the initial discussion, we proceed under the assumption that $\Sigma,\Delta,\Omega\sim O(1)$; later, we will require $\Omega\gg 1$ also. Further simplification is now possible by noting from (3.23) that $\langle U\rangle=0$ to leading order, which reduces (3.22), (3.24) and (3.25) still further. Turning to the porous region near $Y=0_-$, there is no reason *a priori* to suppose that the porous core flow should satisfy $(3.27)-(3.30)$; if it did, we would arrive at $U=\frac{\partial U}{\partial Y}=0$ at $Y=0$, and there would be too many boundary conditions for (U,V,P) in the channel. Instead, we require a porous boundary layer for which $Y\sim\varepsilon^{\frac{1}{2}}$, $\langle U\rangle\sim\varepsilon^{\frac{1}{2}}$; writing

$$Y=\varepsilon^{\frac{1}{2}}\widetilde{Y},\quad \langle U\rangle=\varepsilon^{\frac{1}{2}}\left\langle\widetilde{U}\right\rangle,\quad \langle P\rangle^{(\mathrm{g})}=\left\langle\widetilde{P}\right\rangle^{(\mathrm{g})},\quad \langle V\rangle=\left\langle\widetilde{V}\right\rangle,$$

we have, to leading order, in this layer

$$\frac{\partial}{\partial\widetilde{Y}}\left(\langle\rho\rangle^{(\mathrm{g})}\left\langle\widetilde{V}\right\rangle\right)=0, \tag{3.37}$$

$$\left\langle\widetilde{U}\right\rangle=\frac{\partial^2}{\partial\widetilde{Y}^2}\left(\frac{\left\langle\widetilde{U}\right\rangle}{\gamma}\right), \tag{3.38}$$

$$0=-\frac{\partial\left\langle\widetilde{P}\right\rangle^{(\mathrm{g})}}{\partial\widetilde{Y}}, \tag{3.39}$$

subject to the matching conditions as $\widetilde{Y}\longrightarrow-\infty$

$$\left\langle \widetilde{V} \right\rangle \longrightarrow \langle V \rangle (X,0), \quad \left\langle \widetilde{U} \right\rangle \longrightarrow 0, \quad \left\langle \widetilde{P} \right\rangle^{(\mathrm{g})} \longrightarrow \langle P \rangle^{(\mathrm{g})} (X,0),$$

where

$$\langle V \rangle (X,0) = \lim_{Y \to 0_-} \langle V \rangle, \quad \langle P \rangle^{(\mathrm{g})} (X,0) = \lim_{Y \to 0_-} \langle P \rangle^{(\mathrm{g})}.$$

At $Y = \widetilde{Y} = 0$, we have

$$V = \left\langle \widetilde{V} \right\rangle, \tag{3.40}$$

$$P = \langle P \rangle^{(\mathrm{g})}, \tag{3.41}$$

$$U = \varepsilon^{\frac{1}{2}} \left\langle \widetilde{U} \right\rangle, \tag{3.42}$$

$$\frac{1}{\gamma} \frac{\partial \left\langle \widetilde{U} \right\rangle}{\partial \widetilde{Y}} - \frac{\partial U}{\partial Y} = \left(\frac{\beta_1 \sigma}{\varepsilon} \right) U + \left(\frac{\beta_2 \sigma}{\delta^2} \right) \rho U^2. \tag{3.43}$$

These equations are then used in the following order. First, the channel flow is determined with boundary conditions, to leading order,

$$U = 0, \; V = \left\langle \widetilde{V} \right\rangle.$$

This gives $P(X)$ which serves a boundary condition for $\langle P \rangle^{(\mathrm{g})}$, and finally $\left\langle \widetilde{U} \right\rangle$ can be computed, the boundary condition for this being, at leading order, simply

$$\frac{\partial \left\langle \widetilde{U} \right\rangle}{\partial \widetilde{Y}} = \gamma \left(\frac{\partial U}{\partial Y} \right)_{Y=0} \text{ at } \widetilde{Y} = 0.$$

As for the species equations, no such boundary layer in ε is necessary, with (3.25) being valid all the way up to $Y = 0_-$. In addition, we note that the leading order equations are independent of β_1 and β_2.

3.4. Further simplifications and observations. Invoking the constitutive relation for an ideal gas in dimensionless variables, with

$$\rho = \mathcal{M} + \left(\frac{[\rho] \left(U^{in} \right)^2}{p^{out}} \right) P, \quad \langle \rho \rangle^{(\mathrm{g})} = \langle \mathcal{M} \rangle^{(\mathrm{g})} + \left(\frac{[\rho] \left(U^{in} \right)^2}{p^{out}} \right) \langle P \rangle^{(\mathrm{g})} \tag{3.44}$$

for the channel and porous medium respectively, which can be reduced to just $\rho = \mathcal{M}$, $\langle \rho \rangle^{(\mathrm{g})} = \langle \mathcal{M} \rangle^{(\mathrm{g})}$, respectively, for the pressures and velocities being considered here. The reduced system of equations is now, for $0 \leq X \leq 1$, $0 \leq Y \leq 1$,

$$\frac{\partial}{\partial X} (\rho U) + \frac{\partial}{\partial Y} (\rho V) = 0, \tag{3.45}$$

$$\rho \left(U \frac{\partial U}{\partial X} + V \frac{\partial U}{\partial Y} \right) = -\frac{dP}{dX} + \Delta \frac{\partial^2 U}{\partial Y^2}, \tag{3.46}$$

$$\frac{\partial}{\partial X}\left(U\begin{bmatrix} x_{O_2} \\ x_{H_2O}\end{bmatrix}\right)+\frac{\partial}{\partial Y}\left(V\begin{bmatrix} x_{O_2} \\ x_{H_2O}\end{bmatrix}\right) = \frac{\Delta}{Sc}\frac{\partial}{\partial Y}\left(\frac{\mathbf{M}}{\mathcal{M}}\frac{\partial}{\partial Y}\begin{bmatrix} x_{O_2} \\ x_{H_2O}\end{bmatrix}\right), \quad (3.47)$$

for $0 \le X \le 1$, $-\mathcal{H} \le Y \le 0$,

$$\begin{aligned} \langle\rho\rangle^{(\mathrm{g})}\langle V\rangle &= \Omega\left\{\frac{I}{4}\left(2(1+2\alpha)\mathcal{M}_{H_2O}-\mathcal{M}_{O_2}\right)\right\}, \\ \langle V\rangle &= -\frac{1}{\Delta\Sigma^2}\frac{\partial\langle P\rangle^{(\mathrm{g})}}{\partial Y}, \end{aligned} \quad (3.48)$$

$$\langle V\rangle\begin{bmatrix}\langle x_{O_2}\rangle^{(\mathrm{g})} \\ \langle x_{H_2O}\rangle^{(\mathrm{g})}\end{bmatrix}-\frac{\Delta\gamma^{\frac{3}{2}}}{Sc\langle\mathcal{M}\rangle^{(\mathrm{g})}}\langle\mathbf{M}\rangle^{(\mathrm{g})}\frac{\partial}{\partial Y}\begin{bmatrix}\langle x_{O_2}\rangle^{(\mathrm{g})} \\ \langle x_{H_2O}\rangle^{(\mathrm{g})}\end{bmatrix} = \frac{\Omega I}{4}\begin{bmatrix}-1 \\ 2(1+2\alpha)\end{bmatrix}. \quad (3.49)$$

Note here that (3.48), as well a consideration of the physical parameters, now helps to justify neglecting inertia terms between (2.12) and (2.22), as well as dispersion terms in (2.18) and (2.19). First, the Forchheimer correction term (see Whitaker [**46**]) will be of the order of magnitude of the Reynolds number, Re_γ, based on l_γ, loosely defined by

$$Re_\gamma = \frac{\langle\rho\rangle^{(\mathrm{g})}\langle v\rangle^{(\mathrm{g})}l_\gamma}{\mu}; \quad (3.50)$$

it is justified to use $\langle v\rangle^{(\mathrm{g})}$ for the velocity scale since the foregoing analysis indicates that flow in the porous backing will be unidirectional. Consequently, using (2.37),

$$Re_\gamma \sim \frac{I}{4F\mu}\left(2(1+2\alpha)M_{H_2O}-M_{O_2}\right)l_\gamma \ll 1,$$

as required. In addition, considerations based on this length scale provide some justification for neglecting dispersion effects in the porous backing, as compared to molecular diffusion. Experimental results for one-dimensional flows (e.g. [2, pp. 606-9]) indicate that dispersion will be negligible if the Peclet number of molecular diffusion, Pe_γ, in the porous medium, defined here by

$$Pe_\gamma = \frac{\langle v\rangle^{(\mathrm{g})}l_\gamma}{[D]},$$

is much smaller than one; using the parameters given in Section 3.2, this indeed turns out to be the case.

The boundary conditions are: for $0 \le X \le 1$, $Y = 1$,

$$U = V = \frac{\partial x_{O_2}}{\partial Y} = \frac{\partial x_{H_2O}}{\partial Y} = 0; \quad (3.51)$$

and for $X = 0, \quad 0 \leq Y \leq 1$,

$$U = 1, \quad x_{O_2} = x_{O_2}^{in}, \quad x_{H_2O} = x_{H_2O}^{in}, \quad \text{at} \quad X = 0, \quad 0 \leq Y \leq 1; \tag{3.52}$$

no boundary conditions as such prove to be necessary for $X = 0, \quad -\mathcal{H} \leq Y \leq 0$ since only ordinary differential equations are solved for $-\mathcal{H} \leq Y \leq 0$. At $Y = 0$ for $0 \leq X \leq 1$, porous and fluid quantities are matched through

$$U = 0, \quad V = \langle V \rangle, \quad P = \langle P \rangle, \tag{3.53}$$

$$\langle x_{O_2} \rangle^{(\mathrm{g})} = x_{O_2}, \quad \langle x_{H_2O} \rangle^{(\mathrm{g})} = x_{H_2O}, \tag{3.54}$$

$$\gamma^{\frac{3}{2}} \frac{\partial}{\partial Y} \begin{bmatrix} \langle x_{O_2} \rangle^{(\mathrm{g})} \\ \langle x_{H_2O} \rangle^{(\mathrm{g})} \end{bmatrix} = \frac{\partial}{\partial Y} \begin{bmatrix} x_{O_2} \\ x_{H_2O} \end{bmatrix}. \tag{3.55}$$

In general, I will not be constant; even more generally, it cannot be described *a priori*, but is determined by considering the transport of species in the catalyst, membrane and the anode side also. However, a common practice in studies which emphasize the investigation of flow in the porous backing and the gas channel is simply to prescribe a current density as a function of mole fraction. For example. if we use the dimensional form of the Tafel law given by He, Yi and Nguyen [**23**],

$$I = \frac{a\rho}{M} \exp\left(\frac{\alpha_c F \eta}{RT}\right),$$

where α_c $(= 2)$ is the transfer coefficient of the oxygen reduction reaction (1.2), η is the overpotential for the oxygen reaction and a $\left(= 10^{-6} \text{ Am mol}^{-1}\right)$ is a constant related to the exchange current density and oxygen reference concentration for the oxygen reaction, we obtain the appropriate scale for $[I]$ as

$$[I] = \frac{a\,[\rho]}{[M]} \exp\left(\frac{\alpha_c F \eta}{RT}\right); \tag{3.56}$$

consequently, in dimensionless form,

$$I\left(\langle \rho \rangle^{(\mathrm{g})}, \langle x_{O_2} \rangle^{(\mathrm{g})}, \langle x_{H_2O} \rangle^{(\mathrm{g})}\right) = \frac{\langle \rho \rangle^{(\mathrm{g})} \langle x_{O_2} \rangle^{(\mathrm{g})}}{\langle \mathcal{M} \rangle^{(\mathrm{g})}} = \langle x_{O_2} \rangle^{(\mathrm{g})}. \tag{3.57}$$

A dimensional quantity of importance for the determination of polarization curves is the average current density, I_{av}, which is then given by

$$I_{av} = [I] \int_0^1 I dX.$$

This completes the formulation and necessary definitions. As a next step, we consider the possibility of finding analytical soluton in certain parameter ranges; an obvious choice, in view of the geometry, would be the lubrication theory limit $\left(\Delta^{-1} \ll 1\right)$. The data given in Table 1 for the base case physical parameters indicates that $\Delta^{-1} \sim O(1)$. Obviously, taking channels with smaller aspect ratio, or operating the fuel cell at lower inlet gas velocity would reduce Δ^{-1}, motivating us to then consider the lubrication theory limit, since

it provides qualitatively useful analytical solutions, as well as a quantitative comparison with our numerical method (see Section 6).

Table 1: Parameters for the base case Geometry and operating parameters	
$x_{O_2}^{in}$	0.21
$x_{H_2O}^{in}$	0
h_f	10^{-3}m
h_p	3×10^{-4}m
L	0.1 m
κ	10^{-12} m^2
γ	0.3
U^{in}	1 ms^{-1}
p^{out}	1 atm
T	353 K
μ	10^{-5}kgm^{-1}s^{-1}
Scales for nondimensionalization	
$[\rho]$	1 kgm^{-3}
$[M]$	$[\rho]\,RT/p^{out}$
$[I]$	10^4 Am^{-2}
Physical parameters	
M_{O_2}	0.032 kgmol^{-1}
M_{H_2O}	0.018 kgmol^{-1}
M_{N_2}	0.028 kgmol^{-1}
$\mathcal{D}_{O_2,H_2O}$	$3.749[M]\,/RT$
$\mathcal{D}_{O_2,N_2}$	$2.827[M]\,/RT$
$\mathcal{D}_{H_2O,N_2}$	$3.923[M]\,/RT$

4. Asymptotics for $\frac{[\rho]\left(U^{in}\right)^2}{p^{out}} \ll \Delta^{-1} \ll 1$

Assume $\frac{[\rho]\left(U^{in}\right)^2}{p^{out}} \ll \Delta^{-1} \ll 1$, and rescale according to

$$\langle P\rangle^{(\mathrm{g})} = \Delta\,\langle P\rangle^{(\mathrm{g})}\,,\ P = \Delta P;$$

note here that we require a lower restriction on Δ^{-1} for the following development to hold, otherwise the simplifications following (3.44) will not apply and ρ will depend on P; in practice, the restriction is not unreasonable. Introducing the following asymptotic series

$$\begin{aligned}
\chi &= \chi_0 + \Delta^{-1}\chi_1 + O\left(\Delta^{-2}\right), \quad \text{where } \chi = (U,V,P,\rho)\,,\\
\langle\chi\rangle &= \langle\chi_0\rangle + \Delta^{-1}\langle\chi_1\rangle + O\left(\Delta^{-2}\right), \text{ where } \chi = (V,P)\,,\\
\chi &= \chi^{(0)} + \Delta^{-1}\chi^{(1)} + O\left(\Delta^{-2}\right), \text{ where } \chi = (x_{O_2}, x_{H_2O}, \mathbf{M})\,,
\end{aligned}$$

$$\begin{aligned}\langle\chi\rangle^{(\mathrm{g})} &= \langle\chi_0\rangle^{(g)} + \Delta^{-1}\langle\chi_1\rangle^{(g)} + O\left(\Delta^{-2}\right), \text{ where } \chi = (\rho),\\ \langle\chi\rangle^{(\mathrm{g})} &= \left\langle\chi^{(0)}\right\rangle^{(\mathrm{g})} + \Delta^{-1}\left\langle\chi^{(1)}\right\rangle^{(\mathrm{g})} + O\left(\Delta^{-2}\right), \text{ where } \chi = (x_{O_2}, x_{H_2O}, \mathbf{M}),\end{aligned}$$

we observe that, at leading order, the governing equations permit a solution of the form

$$\begin{aligned}x_{O_2}^{(0)} &= \left\langle x_{O_2}^{(0)}\right\rangle^{(\mathrm{g})} = F_{O_2}(X),\\ x_{H_2O}^{(0)} &= \left\langle x_{H_2O}^{(0)}\right\rangle^{(\mathrm{g})} = F_{H_2O}(X),\end{aligned}$$

with $F_{O_2}(0) = x_{O_2}^{in}$, $F_{H_2O}(0) = x_{H_2O}^{in}$. Then

$$U_0(X,Y) = \frac{1}{2}\frac{dP_0}{dX}\left(Y^2 - Y\right),$$

whereupon, writing $\Phi = (2(1+2\alpha)\mathcal{M}_{H_2O} - \mathcal{M}_{O_2})$ (NB: $\Phi > 0$) and using,

$$\frac{d}{dX}\left(\int_0^1 \rho_0 U_0 dY\right) = \frac{\Omega\Phi I\left(F_{O_2}(X)\right)}{4},$$

where

$$\rho_0(X) = \mathcal{M}_{N_2} + \left(\mathcal{M}_{O_2} - \mathcal{M}_{N_2}\right)F_{O_2}(X) + \left(\mathcal{M}_{H_2O} - \mathcal{M}_{N_2}\right)F_{H_2O}(X),$$

we have

$$\int_0^1 \rho_0 U_0 dY = \frac{\Omega\Phi}{4}J(X) + \rho_0(0),$$

where

$$J(X) = \int_0^X I\left(F_{O_2}(X')\right)dX'.$$

Hence

$$\frac{dP_0}{dX} = -\frac{12}{\rho_0(X)}\left[\frac{\Omega\Phi}{4}J(X) + \rho_0(0)\right],$$

and so

$$\begin{aligned}U_0(X,Y) &= \frac{6}{\rho_0(X)}\left[\frac{\Omega\Phi}{4}J(X) + \rho_0(0)\right]\left(Y - Y^2\right),\\ V_0(X,Y) &= -\frac{3\Omega\Phi}{2}\frac{I\left(F_{O_2}(X)\right)}{\rho_0(X)}\left(\frac{Y^2}{2} - \frac{Y^3}{3} - \frac{1}{6}\right),\\ \langle V_0(X)\rangle &= \Omega\Phi\frac{I\left(F_{O_2}(X)\right)}{4\langle\rho_0(X)\rangle},\\ \langle P_0(X,Y)\rangle &= -\Sigma^2\Omega\left\{\frac{\Phi I\left(F_{O_2}(X)\right)}{4\langle\rho_0(X)\rangle}\right\}Y - 12\left[\frac{\Omega\Phi J(X)}{\langle\rho_0(X)\rangle} + X\right].\end{aligned}$$

At this stage, $F_{O_2}(X)$ and $F_{H_2O}(X)$ (and hence $U_0, V_0, \langle V_0\rangle, \langle P_0\rangle, \rho_0$) remain undetermined, indicating that the problem at $O(1)$ is degenerate; this appears to be because the boundary conditions for x_{O_2} and x_{H_2O} at $Y = -\mathcal{H}, 1$ at this order are both of Neumann-type. This indeterminacy is remedied, however, at $O\left(\Delta^{-1}\right)$, as follows.

At $O\left(\Delta^{-1}\right)$, (3.47) gives

$$\frac{\partial}{\partial X}\left(U_0\left[\begin{array}{c} F_{O_2}(X) \\ F_{H_2O}(X) \end{array}\right]\right)+\frac{\partial}{\partial Y}\left(V_0\left[\begin{array}{c} F_{O_2}(X) \\ F_{H_2O}(X) \end{array}\right]\right)= \tag{4.1}$$

$$\frac{1}{Sc}\frac{\partial}{\partial Y}\left(\frac{\mathbf{M}^{(0)}}{\rho_0(X)}\frac{\partial}{\partial Y}\left[\begin{array}{c} x_{O_2}^{(1)} \\ x_{H_2O}^{(1)} \end{array}\right]\right);$$

for $0 \le X \le 1$, $-\mathcal{H} \le Y \le 0$,

$$\frac{\Omega\Phi I\left(F_{O_2}(X)\right)}{4\langle\rho_0(X)\rangle}\left[\begin{array}{c} F_{O_2}(X) \\ F_{H_2O}(X) \end{array}\right]-\frac{\gamma^{\frac{3}{2}}}{Sc}\frac{\left\langle\mathbf{M}^{(0)}\right\rangle^{(\mathrm{g})}}{\langle\rho_0(X)\rangle}\frac{\partial}{\partial Y}\left[\begin{array}{c} \left\langle x_{O_2}^{(1)}\right\rangle^{(\mathrm{g})} \\ \left\langle x_{H_2O}^{(1)}\right\rangle^{(\mathrm{g})} \end{array}\right]= \tag{4.2}$$

$$\frac{\Omega I\left(F_{O_2}(X)\right)}{4}\left[\begin{array}{c} -1 \\ 2(1+2\alpha) \end{array}\right].$$

(4.1) can be rewritten as

$$U_0\left[\begin{array}{c} F'_{O_2}(X) \\ F'_{H_2O}(X) \end{array}\right]+\left(\frac{\partial U_0}{\partial X}+\frac{\partial V_0}{\partial Y}\right)\left[\begin{array}{c} F_{O_2}(X) \\ F_{H_2O}(X) \end{array}\right]=\frac{1}{Sc}\frac{\mathbf{M}^{(0)}}{\rho_0(X)}\frac{\partial^2}{\partial Y^2}\left[\begin{array}{c} x_{O_2}^{(1)} \\ x_{H_2O}^{(1)} \end{array}\right],$$

and then, on using

$$\frac{\partial}{\partial X}\left(\rho_0 U_0\right)+\frac{\partial}{\partial Y}\left(\rho_0 V_0\right)=0,$$

we have

$$U_0\left\{\left[\begin{array}{c} F'_{O_2}(X) \\ F'_{H_2O}(X) \end{array}\right]-\frac{1}{\rho_0(X)}\frac{\partial\rho_0}{\partial X}\left[\begin{array}{c} F_{O_2}(X) \\ F_{H_2O}(X) \end{array}\right]\right\}=\frac{1}{Sc}\frac{\mathbf{M}^{(0)}}{\rho_0(X)}\frac{\partial^2}{\partial Y^2}\left[\begin{array}{c} x_{O_2}^{(1)} \\ x_{H_2O}^{(1)} \end{array}\right].$$

Integrating once with respect to Y, we have

$$\lambda_0(X)\left\{\left[\begin{array}{c} F'_{O_2}(X) \\ F'_{H_2O}(X) \end{array}\right]-\frac{1}{\rho_0(X)}\frac{\partial\rho_0}{\partial X}\left[\begin{array}{c} F_{O_2}(X) \\ F_{H_2O}(X) \end{array}\right]\right\}\left(\frac{Y^2}{2}-\frac{Y^3}{3}-\frac{1}{6}\right)$$
$$=\frac{1}{Sc}\frac{\mathbf{M}^{(0)}}{\rho_0(X)}\frac{\partial}{\partial Y}\left[\begin{array}{c} x_{O_2}^{(1)} \\ x_{H_2O}^{(1)} \end{array}\right], \tag{4.3}$$

where we have written $U_0=\frac{\lambda_0(X)}{\rho_0(X)}\left(Y-Y^2\right)$, with

$$\lambda_0(X)=6\left[\frac{\Omega\Phi}{4}J(X)+\rho_0(0)\right],$$

and have already implemented (3.51) at $O\left(\Delta^{-1}\right)$. Requiring now, at $Y=0$,

$$\gamma^{\frac{3}{2}}\frac{\partial}{\partial Y}\left[\begin{array}{c} \left\langle x_{O_2}^{(1)}\right\rangle^{(\mathrm{g})} \\ \left\langle x_{H_2O}^{(1)}\right\rangle^{(\mathrm{g})} \end{array}\right]=\frac{\partial}{\partial Y}\left[\begin{array}{c} x_{O_2}^{(1)} \\ x_{H_2O}^{(1)} \end{array}\right],$$

we combine (4.2) and (4.3) to give

$$\begin{aligned} & -\frac{2\lambda_0(X)}{3\Omega\rho_0(X)I\left(F'_{O_2}(X)\right)}\left\{\begin{bmatrix} F'_{O_2}(X) \\ F'_{H_2O}(X) \end{bmatrix} - \frac{1}{\rho_0(X)}\frac{\partial\rho_0}{\partial X}\begin{bmatrix} F_{O_2}(X) \\ F_{H_2O}(X) \end{bmatrix}\right\} \\ = \quad & \frac{\Phi}{\rho_0(X)}\begin{bmatrix} F_{O_2}(X) \\ F_{H_2O}(X) \end{bmatrix} - \begin{bmatrix} -1 \\ 2(1+2\alpha) \end{bmatrix}. \end{aligned}$$

Note that this has led to the elimination of $x_{O_2}^{(1)}$ and $x_{H_2O}^{(1)}$ and has instead led to a pair of non-linear ODEs for $F_{O_2}(X)$ and $F_{H_2O}(X)$.

Next, defining

$$\zeta_{O_2}(X) = F_{O_2}(X)/\rho_0(X),\ \zeta_{H_2O}(X) = F_{H_2O}(X)/\rho_0(X),$$

we simplify to

$$\begin{aligned} & \frac{-4}{\Omega I\left(F_{O_2}(X)\right)}\left[\frac{\Omega\Phi}{4}J(X) + \rho_0(0)\right]\frac{\partial}{\partial X}\begin{bmatrix} \zeta_{O_2}(X) \\ \zeta_{H_2O}(X) \end{bmatrix} \\ & = \Phi\begin{bmatrix} \zeta_{O_2}(X) \\ \zeta_{H_2O}(X) \end{bmatrix} - \begin{bmatrix} -1 \\ 2(1+2\alpha) \end{bmatrix}, \end{aligned}$$

with initial conditions

$$\begin{aligned} \zeta_{O_2}(0) &= \frac{x_{O_2}^{in}}{\mathcal{M}_{N_2} + (\mathcal{M}_{O_2} - \mathcal{M}_{N_2})x_{O_2}^{in} + (\mathcal{M}_{H_2O} - \mathcal{M}_{N_2})x_{H_2O}^{in}}, \\ \zeta_{H_2O}(0) &= \frac{x_{H_2O}^{in}}{\mathcal{M}_{N_2} + (\mathcal{M}_{O_2} - \mathcal{M}_{N_2})x_{O_2}^{in} + (\mathcal{M}_{H_2O} - \mathcal{M}_{N_2})x_{H_2O}^{in}}. \end{aligned}$$

Replacing the partial derivative, we can simplify to

$$\frac{d\zeta_{O_2}}{d\zeta_{H_2O}} = \frac{\Phi\zeta_{O_2} + 1}{\Phi\zeta_{H_2O} - 2(1+2\alpha)},$$

whence, on applying the inlet conditions,

$$\left[\Phi\zeta_{O_2}(0) + 1\right]\zeta_{H_2O}(X) - \left[\Phi\zeta_{H_2O}(0) - 2(1+2\alpha)\right]\zeta_{O_2}(X) = \tag{4.4}$$

$$2(1+2\alpha)\zeta_{O_2}(0) + \zeta_{H_2O}(0).$$

Note, in addition, that this result holds regardless of the expression used for the current density.

Returning now to

$$\frac{-4}{\Omega I\left(F_{O_2}(X)\right)}\left[\frac{\Omega}{4}\Phi J(X) + \rho_0(0)\right]\frac{d\zeta_{O_2}}{dX} = \Phi\zeta_{O_2} + 1,$$

this too can be integrated regardless of the form of I. We have, since $J(0) = 0$ for any current density we care to choose,

$$\zeta_{O_2}(X) = \frac{1}{\Phi}\left\{\left(\Phi\zeta_{O_2}(0) + 1\right)\left(\frac{4\rho_0(0)}{4\rho_0(0) + \Omega\Phi J(X)}\right) - 1\right\}, \tag{4.5}$$

which is effectively an integral equation for $\zeta_{O_2}(X)$. More convenient is a first-order ODE for $\zeta_{O_2}(X)$, which is obtained after rearranging and differentiating, as

$$I\left(\frac{\mathcal{M}_{N_2}\zeta_{O_2}(X)}{1-\left(\mathcal{M}_{O_2}-\mathcal{M}_{N_2}\right)\zeta_{O_2}(X)-\left(\mathcal{M}_{H_2O}-\mathcal{M}_{N_2}\right)\zeta_{H_2O}(X)}\right)$$
$$=-\frac{4\rho_0(0)}{\Omega}\frac{\left(\Phi\zeta_{O_2}(0)+1\right)}{\left(\Phi\zeta_{O_2}(X)+1\right)^2}\frac{d\zeta_{O_2}}{dX},$$

and then

$$I\left(\frac{\zeta_{O_2}(X)}{\mathcal{A}+\mathcal{B}\zeta_{O_2}(X)}\right)=-\frac{4\rho_0(0)}{\Omega}\frac{\left(\Phi\zeta_{O_2}(0)+1\right)}{\left(\Phi\zeta_{O_2}(X)+1\right)^2}\frac{d\zeta_{O_2}}{dX}, \tag{4.6}$$

where

$$\mathcal{A} = \frac{1}{\mathcal{M}_{N_2}}\left(\left(\mathcal{M}_{H_2O}-\mathcal{M}_{N_2}\right)\left(\frac{2(1+2\alpha)\zeta_{O_2}(0)+\zeta_{H_2O}(0)}{\left[\Phi\zeta_{O_2}(0)+1\right]}\right)-1\right),$$
$$\mathcal{B} = \frac{1}{\mathcal{M}_{N_2}}\left(\left(\mathcal{M}_{O_2}-\mathcal{M}_{N_2}\right)+\left(\mathcal{M}_{H_2O}-\mathcal{M}_{N_2}\right)\frac{\left[\Phi\zeta_{H_2O}(0)-2(1+2\alpha)\right]}{\left[\Phi\zeta_{O_2}(0)+1\right]}\right).$$

Note that (4.6) implies that if oxygen is fully depleted, at which point (say $X=X_0$) $\zeta_{O_2}=I=0$, then we will necessarily have $\frac{d\zeta_{O_2}}{dX}=0$ there also.

As an example, and for later use, we note a closed-form solution when $I\equiv\langle x_{O_2}\rangle^{(g)}$; in this case,

$$\frac{\zeta_{O_2}(X)}{\mathcal{A}+\mathcal{B}\zeta_{O_2}(X)}=-\frac{4\rho_0(0)}{\Omega}\frac{\left(\Phi\zeta_{O_2}(0)+1\right)}{\left(\Phi\zeta_{O_2}(X)+1\right)^2}\frac{d\zeta_{O_2}}{dX},$$

which can be integrated exactly to give

$$\mathcal{A}\log\left(\frac{\zeta_{O_2}(X)\left(\Phi\zeta_{O_2}(0)+1\right)}{\zeta_{O_2}(0)\left(\Phi\zeta_{O_2}(X)+1\right)}\right)-(\mathcal{A}\Phi-\mathcal{B})\left(\frac{\zeta_{O_2}(X)-\zeta_{O_2}(0)}{\left(\Phi\zeta_{O_2}(X)+1\right)\left(\Phi\zeta_{O_2}(0)+1\right)}\right)$$
$$=\frac{\Omega X}{4\rho_0(0)\left(\Phi\zeta_{O_2}(0)+1\right)}. \tag{4.7}$$

This formula suggests that for $\Omega\sim O(1)$ there is no possibility for oxygen depletion $\left(\zeta_{O_2}=0\right)$, since the first-term on the left-hand side of (4.7) could not then be balanced by either of the other two terms. In addition, for $\Omega\gg 1$ (and noting that $\mathcal{A}<0$),

$$\mathcal{A}\log\left(\frac{\zeta_{O_2}(X)\left(\Phi\zeta_{O_2}(0)+1\right)}{\zeta_{O_2}(0)\left(\Phi\zeta_{O_2}(X)+1\right)}\right)\sim\frac{\Omega X}{4\rho_0(0)\left(\Phi\zeta_{O_2}(0)+1\right)},$$

whence

$$\frac{\zeta_{O_2}(X)}{\left(\Phi\zeta_{O_2}(X)+1\right)}\sim\frac{\zeta_{O_2}(0)}{\left(\Phi\zeta_{O_2}(0)+1\right)}\exp\left(\frac{\Omega X}{4\mathcal{A}\rho_0(0)\left(\Phi\zeta_{O_2}(0)+1\right)}\right),$$

and thus

$$\zeta_{O_2}(X) \sim \frac{1}{\left(\Phi + \frac{1}{\zeta_{O_2}(0)}\right)\exp\left(\frac{-\Omega X}{4\mathcal{A}\rho_0(0)\left(\Phi\zeta_{O_2}(0)+1\right)}\right) - \Phi};$$

in this regime, we also have

$$\zeta_{H_2O}(X) \sim \frac{2}{\Phi}(1+2\alpha) + \frac{\zeta_{H_2O}(0) - \frac{2}{\Phi}(1+2\alpha)}{\left(\Phi\zeta_{O_2}(0)+1\right) - \Phi\zeta_{O_2}(0)\exp\left(\frac{\Omega X}{4\mathcal{A}\rho_0(0)\left(\Phi\zeta_{O_2}(0)+1\right)}\right)}.$$

Note also that, this far, the results are independent of whether or not crossed diffusion is assumed, or if non-linear diffusion coefficients are used or not.

As a corollary, we observe that the solution at $O\left(\Delta^{-1}\right)$, i.e. for $x_{O_2}^{(1)}$, $x_{H_2O}^{(1)}$, $\left\langle x_{O_2}^{(1)}\right\rangle^{(g)}$, $\left\langle x_{H_2O}^{(1)}\right\rangle^{(g)}$ still remains undetermined, since consideration of the field equations and boundary conditions at $O\left(\Delta^{-1}\right)$ merely leads to the solution being fully determined at $O(1)$. By analogy, to determine the solutions at $O\left(\Delta^{-1}\right)$ completely, we would need to consider the field equations and boundary conditions at $O\left(\Delta^{-2}\right)$; by this stage, however, the algebra becomes lengthy and in the interests of brevity we omit further discussion. In fact, one does not really gain so much by finding these solutions anyway, since there is no compact solution as there is at $O(1)$, and we proceed instead to a numerical solution for the general case when $\Delta^{-1} \sim O(1)$.

5. Numerical method and results

To complement the asymptotics for $\Delta^{-1} \ll 1$, so as to account for regimes when $\Delta^{-1} \sim O(1)$, the simplified parabolized equations were solved numerically using the Keller-Box discretisation scheme and Newton iteration (see, for example, Cebeci and Bradshaw [**10**]). The system of partial differential equations to be solved in the channel is of 8th order, and this is coupled to a 6th order system of ordinary differential equations in the porous region. As is well-known, the scheme is second-order accurate in both time-like and space-like variables, and we omit any further details here. As an indication of the speed of the computations, we note that a typical run with 500 points across, and 200 points along, the channel required around 100 CPU seconds on a 500 MHz Compaq Alphaserver with 3GB RAM.

Results are presented for the Tafel law given in dimensionless form by (3.57), and used previously for PEFC studies by [**23, 14, 33, 49**]. Throughout, we keep $\gamma = 0.3, T = 353K$, and concentrate more on the effect of changes in channel height and length, porous backing thickness and permeability, pressure, inlet speed and composition. Physically realistic and implementable changes in any of these will result in, at most, an order of magnitude change in the relevant dimensionless parameter. The most sensitive parameter is Ω, which varies over several orders of magnitude as the cell voltage E_{cell} decreases; note

here that we revert to using the cell voltage rather than the overpotential, η, with the two being related by

$$E_{cell} = E_0 - \eta,$$

where $E_0 (= 1.1V)$ is termed the open circuit voltage of the fuel cell.

5.1. Effect of Δ and Ω. We show first results for $E_{cell} = 0.75V$, corresponding to $\Omega = 10.2$, ranging over several orders of magnitude in Δ, and compare these with the analytical results in the lubrication theory limit. Figures 3 and 4 are for intrinsic oxygen and water mole fraction at $Y = -\mathcal{H}$, respectively, and demonstrate that the lubrication solution works well for Δ^{-1} as high as $O\left(10^{-2}\right)$.

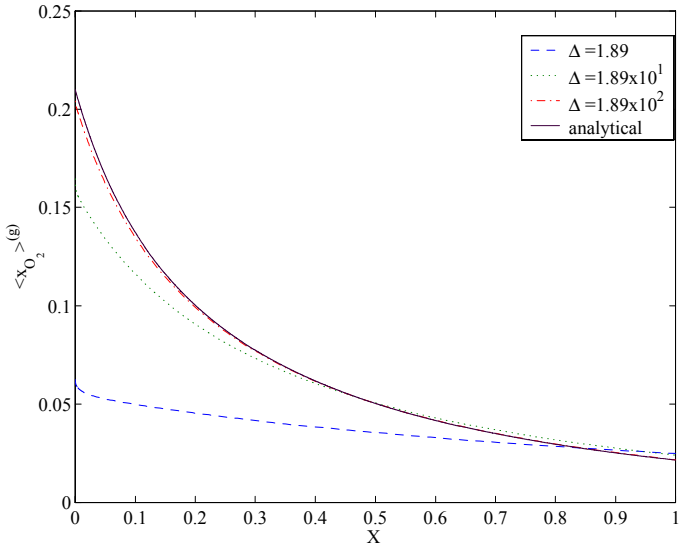

Figure 3. Comparison of analytical solution for $\langle x_{O_2} \rangle^{(g)}$ at $Y = -\mathcal{H}$ with numerical solutions for $\Delta = 1.89, 1.89 \times 10^1, 1.89 \times 10^2$ $(E_{cell} = 0.75V)$.

On the other hand, the base case physical values given in Table 1 correspond to $\Delta = 1.89$. Figure 5 shows the streamwise velocity U at $Y = \frac{1}{2}$, and illustrates the extent of deviation from the classical value $\frac{3}{2}$. An interesting limit occurs as E_{cell} is decreased.
In this case, Ω increases although the quantity $\Omega \langle x_{O_2} \rangle^{(g)}$ at $Y = -\mathcal{H}$ remains $O(1)$; this corresponds to the attainment of the limiting current and the corresponding plots are given in Figures 6-8; observe that in Figures 6 and 7 the limiting values for intrinsic oxygen and water mole fraction for the analytical solution are reached very rapidly, so that in Figure 6 the curve for $\langle x_{O_2} \rangle^{(g)}$ effectively lies on the X-axis.

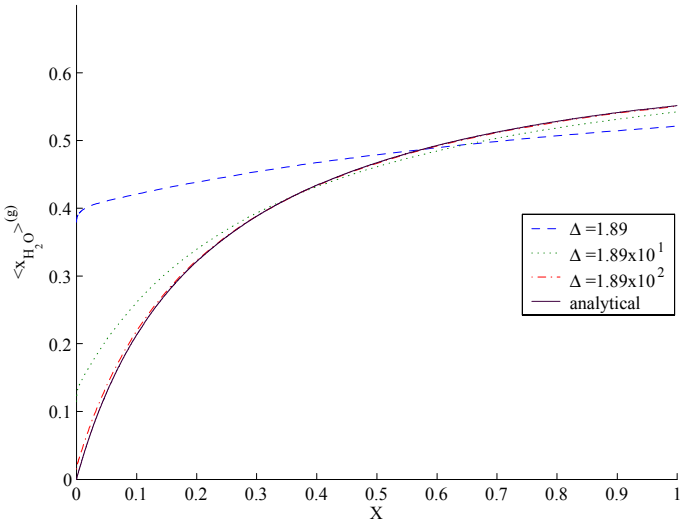

Figure 4. Comparison of analytical solution for $\langle x_{H_2O} \rangle^{(g)}$ at $Y = -\mathcal{H}$ with numerical solutions for $\Delta = 1.89, 1.89 \times 10^1, 1.89 \times 10^2$ $(E_{cell} = 0.75V)$.

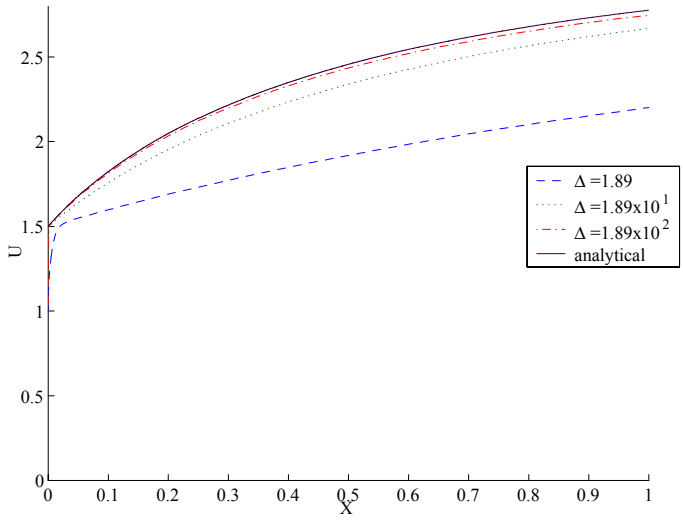

Figure 5. Comparison of analytical solution for U at $Y = \frac{1}{2}$ with numerical solutions for $\Delta = 1.89, 1.89 \times 10^1, 1.89 \times 10^2$ $(E_{cell} = 0.75V)$.

As regards the numerics, it was found that considerably more outer loop iterations for the density were required as Ω was increased. For instance, whereas 4 iterations sufficed for $E_{cell} = 0.75V$, it was common for 20-30 to be necessary for $E_{cell} = 0.65V$. In addition, there were difficulties in initiating the marching scheme at $X = 0$ for higher values of Ω; we surmise this to be due to increased non-linearity near X=0, since x_O2 changes more abruptly for higher values of Omega. Whilst setting the channel inlet values as an initial guess for the first step along the channel was adequate for lower values of Ω, this was found not be sufficient for E_{cell} lower than $0.71V$; for those cases, the first-step solution for $E_{cell} = 0.71V$ had to be used instead, then enabling numerical solutions to be obtained for higher and higher values of Ω until the limiting current was reached.

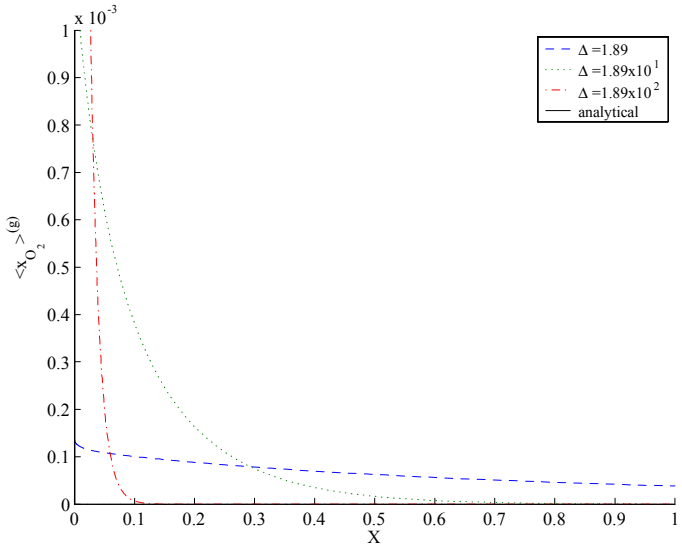

Figure 6. Comparison of analytical solution for $\langle x_{O_2} \rangle^{(g)}$ at $Y = -\mathcal{H}$ with numerical solutions for $\Delta = 1.89, 1.89 \times 10^1, 1.89 \times 10^2$ $(E_{cell} = 0.65V)$.

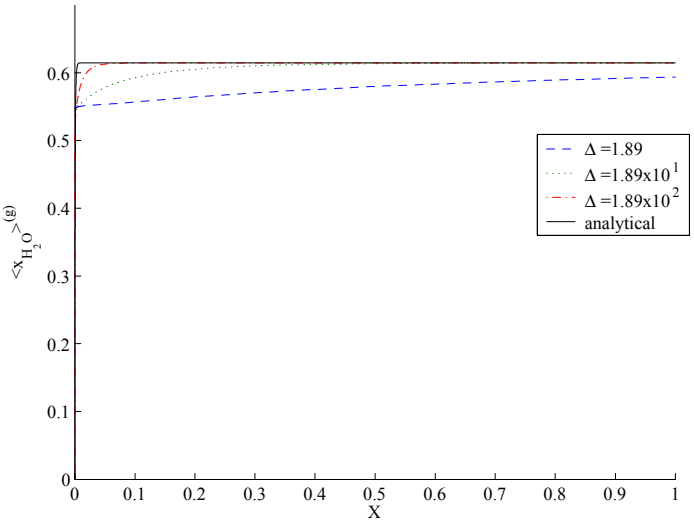

Figure 7. Comparison of analytical solution for $\langle x_{H_2O} \rangle^{(g)}$ at $Y = -\mathcal{H}$ with numerical solutions for $\Delta = 1.89, 1.89 \times 10^1, 1.89 \times 10^2$ $(E_{cell} = 0.65V)$.

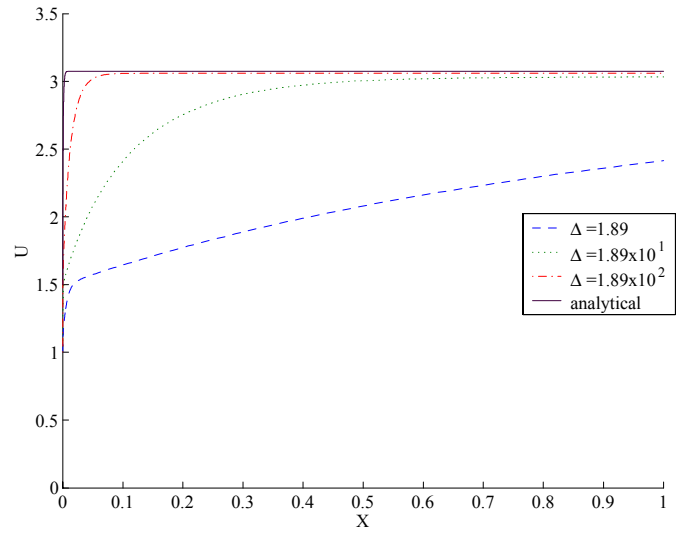

Figure 8. Comparison of analytical solution for U at $Y = \frac{1}{2}$ with numerical solutions for $\Delta = 1.89, 1.89 \times 10^1, 1.89 \times 10^2$ $(E_{cell} = 0.65V)$.

5.2. 'Polarization surfaces'. It is customary for fuel cell performance to be given in terms of a polarization curve where the cell potential, E_{cell}, is given as function of the average current density, I_{av}. Generally speaking, if the analysis is done dimensionally, this leads to a vast number of graphs for each alteration made in one of the physical parameters. However, a major benefit of the nondimensional analysis carried out here is that the results can be expressed considerably more compactly by plotting polarization 'surfaces'; individual polarization curves will therefore be curves lying on those surfaces. We explain this as follows. From the nondimensionalization given above, the emergent nondimensional parameters were Δ, Σ, Ω and Sc. In addition, there is γ, which we hold fixed in this study, and $x_{O_2}^{in}$,$x_{H_2O}^{in}$ and $\mathcal{H}$, whose effect on fuel cell performance one would like to explore. First, we observe that, in the parameter range of interest, Σ has no effect on I_{av}, since the dimensionless density is independent of pressure and the pressure in the channel serves as a boundary condition for the pressure in the porous medium. In addition, a change in Sc can only be effected by changes in $[\rho]$, which only occurs if the cathode is run at a different pressure. Consequently, a tidy representation of I_{av} is to plot it as a function of Δ and Ω, for fixed $Sc, x_{O_2}^{in}$,$x_{O_2}^{in}$ and $\mathcal{H}$, the benefit of this being that the effect of four parameters, h_f, L, U^{in} and E_{cell}, are displayed on one graph; since Ω can vary over several orders of magnitude, it proves more convenient to use $\log(\Omega)$ as a variable. Examples of this are given below.

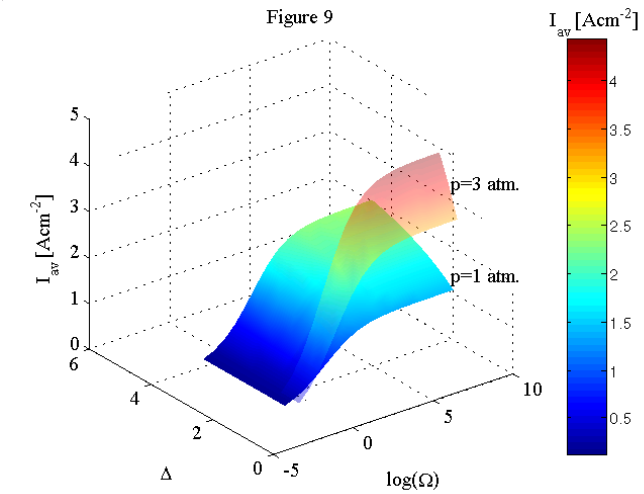

Figure 9. Polarization surfaces for $p^{out} = 1, 3$ atm $(\mathcal{H} = 0.3)$.

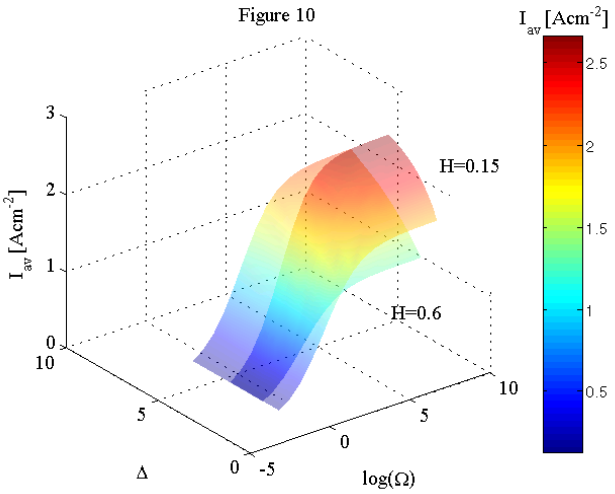

Figure 10. Polarization surfaces for $\mathcal{H} = 0.15, 0.6$ ($p^{out} = 1$ atm).

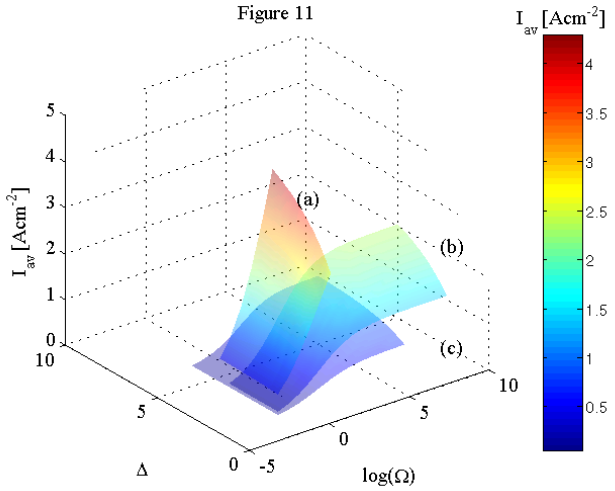

Figure 11. Polarization surfaces for $p^{out} = 1$ atm with: (a) $x^{in}_{O_2} = 1$, $x^{in}_{H_2O} = 0$; (b) $x^{in}_{O_2} = 0.21$, $x^{in}_{H_2O} = 0$; (c) $x^{in}_{O_2} = 0.13$, $x^{in}_{H_2O} = 0.36$.

Figure 9 gives polarization surfaces for $\mathcal{H} = 0.3$, with the pressure at 1 and 3 atmospheres. The limiting current phenomenon is observed as Ω increases, and its value is observed to increase moderately with increasing Δ, but strongly with increasing pressure. Figure 10 shows a similar plot, except with computations

now for $p^{out} = 1$ atm, for $\mathcal{H} = 0.15$ and $\mathcal{H} = 0.6$. Average current densities are found to be higher for the thinner porous backing, and in both cases a limiting value is evident as Ω is increased. Figure 11 compares the base case for $p^{out} = 1$ atm and $x_{O_2}^{in} = 0.21$ with two other cases at 1 atm which have differing inlet compositions: dry oxygen $\left(x_{O_2}^{in} = 1\right)$ and partially humidified air, for which $x_{O_2}^{in} = 0.13$ and $x_{H_2O}^{in} = 0.36$ (corresponding to 76% relative humidity) [**20, 18, 7**]. As is evident, increased oxygen content at the inlet raises the average current density; for $x_{O_2}^{in} = 1$, convergence difficulties were experienced for quite low values of Ω, which explains the rather narrow range of values presented for this case, but nonetheless the average current density is much higher than that for the other two cases.

6. Conclusions

In this paper, we have considered a 2-D model for three-component gaseous flow in the cathode of a polymer electrolyte fuel cell. Assuming a slender geometry, we have derived analytical solutions where possible, and complemented these with a numerical study. By choosing to perform the study nondimensionally, we have identified several features that are not evident from earlier work done dimensionally. In summary, we identify four main dimensionless parameters ($\Delta, \Omega, \Sigma, Sc$; see Sections 2 and 3 for definitions); other parameters that are present in this model are the porous backing porosity, γ (held fixed at 0.3 in this study), the temperature T (held fixed at 353K), the ratio of channel and porous backing heights ($\mathcal{H}$), the inlet oxygen and water content ($x_{O_2}^{in}$ and $x_{H_2O}^{in}$ respectively) and the number of water molecules affiliated to each proton that passes across the membrane to the cathode (α). We find that the flow in the porous backing is essentially unidirectional, although it interacts with a fully 2-D flow in the gas channel. Furthermore, Σ is found to play a secondary role, having next to no effect on the gas mole fraction distribution in the porous backing; physically, this implies an insensivity to porous backing permeability. The fact that the cathode is more or less isobaric gives that the density is a multiple of the molecular weight. In addition, the Schmidt number, Sc, can only be affected by variations in the operating pressure, and we find that a convenient and compact way to understand fuel cell performance is to plot average current density as a function of Δ and Ω for different values of Sc and $\mathcal{H}$; this gives a surface which implicitly contains an infinite family of polarization curves, which is the customary way to assess cell performance. These surfaces have been generated numerically, and in comparatively rapid fashion, using the Keller Box scheme for systems of parabolic partial differential equations, to provide a rather comprehensive parameter study.

The present work was, needless to say, limited in several respects. To begin with, and has often been stated before, at higher current densities two-phase flow can be expected as water droplets form at the catalytic layer; this will be the starting point for future work. Also, we limited ourselves here to prescribing an often-used Tafel law for the current density relation at the catalytic layer, for

one temperature value and one value of porosity; in addition, α was assumed to be constant along the length of the cell. Naturally, the question arises as to whether more sophisticated modeling would lead to a qualitative change in the results. Essentially, such an approach would involve attempting to represent the catalytic layer more faithfully, e.g as has been attempted for molten carbonate fuel cells [**37**]. A characteristic of this approach would be that a Tafel law is used for reactions across this layer, which would be treated as consisting of the material of which the gas-diffusion electrode, as well as polymer electrolyte. Combined with the fact that this layer is much thinner than the gas-diffusion electrode, it is likely that the functional form for the current density would not be much different from what we have used here. On the other hand, if the overpotential and/or temperature are no longer treated as constant, then the exponential term involving these quantities in the expression for the current density could indeed affect the results significantly. Needless to say, this also is the subject of future work.

Acknowledgment

Financial support from the Swedish Foundation for Strategic Environmental Research (MISTRA) is gratefully acknowledged. The work was done within the framework of the Jungner Centre.

Bibliography

[1] B. Alazmi and K. Vafai, *Analysis of fluid flow and heat transfer interfacial conditions between a porous layer and a fluid layer,* Int. J. Heat and Mass Transfer, 44 (2001) pp. 1735-1749.

[2] J. Bear, *Dynamics of Fluids in Porous Media,* Dover, New York (1988).

[3] J. Bear and J. M. Buchlin, *Modeling and Applications of Transport Phenomena in Porous Media,* Kluwer Academic Publishers, Boston (1991).

[4] G. S. Beavers and D. D. Joseph, Boundary conditions at a naturally permeable wall, *J. Fluid Mech.* 30 (1967) pp. 197-207.

[5] D. M. Bernardi and M. W. Verbrugge, *Mathematical model of a gas diffusion electrode bonded to a polymer electrolyte*, AIChE Journal 37 (1991), pp. 1151-1163.

[6] D. M. Bernardi and M. W. Verbrugge, *A mathematical model of the solid-polymer-electrolyte fuel cell*, J. Electrochem. Soc. 139 (1992), pp. 2477-2491.

[7] J. Billingham, A. C. King, R. C. Copcutt and K. Kendall, *Analysis of a model for a loaded, planar, solid oxide fuel cell*, SIAM J. Appl. Math., 60 (2000) pp. 574-601.

[8] R. B. Bird, W. E. Stewart and E. N. Lightfoot, *Transport Phenomena*, Wiley, New York, 1960.

[9] E. Birgersson, J. Nordlund, H. Ekström, M. Vynnycky and G. Lindbergh, *A reduced two-dimensional one-phase model for analysis of the anode of a DMFC,* submitted to J. Electrochem. Soc.

[10] T. Cebeci and P. Bradshaw, *Momentum Transfer in Boundary Layers,* Washington: Hemisphere Publishing Corporation, 1977.

[11] R. J. Cooper, J. Billingham and A. C. King, *Flow and reaction in solid oxide fuel cells,* J. Fluid Mech., 411 (2000) pp. 233-262.

[12] E. L. Cussler, *Diffusion: Mass Transfer in Fluid Systems,* Cambridge University Press, New York, 1984.

[13] K. Dannenberg, P. Ekdunge and G. Lindbergh, *Mathematical model of the PEMFC,* Journal of Applied Electrochemistry, 30 (2000) pp. 1377-1387.

[14] P. De Vidts and R. E. White, *Governing equations for transport in porous electrodes*, J. Electrochem. Soc., 144 (1997) pp. 1343-1353.

[15] S. Dutta, S. Shimpalee and J. W. van Zee, *Three-dimensional numerical simulation of straight channel PEM cells*, Journal of Applied Electrochemistry, 30 (2000) pp. 135-146.

[16] S. Dutta, S. Shimpalee and J. W. van Zee, *Numerical prediction of mass exchange between cathode and anode channels in a PEM fuel cell,* Int. J. Heat and Mass Transfer, 44 (2001) pp. 2029-2042.

[17] A. Fischer, J. Jindra and H. Wendt, *Porosity and catalyst utilization of thin layer cathodes in air operated PEM-fuel cells,* Journal of Applied Electrochemistry, 28 (1998) pp. 277-282.

[18] T. F. Fuller and J. Newman, *Water and thermal management in solid-polymer-electrolyte fuel cells*, J. Electrochem. Soc. 140 (1993), pp. 1218-1225.

[19] P. Futerko and I-M. Hsing, *Two-dimensional finite-element study of the resistance of membranes in polymer electrolyte fuel cells*, Electrochimica Acta, 45 (2000), pp. 1741-1751.
[20] V. Gurau, H. Liu and S. Kakac, *Two-dimensional model for proton exchange membrane fuel cells*, AIChE Journal, 44 (1998), pp. 2410-2422.
[21] V. Gurau, F. Barbir and H. Liu, *An analytical solution of a half-cell model for PEM fuel cells,* J. Electrochem. Soc. 147 (2000), pp. 2468-2477.
[22] W. He and Q. Chen, *Three-dimensional simulation of a molten carbonate fuel cell stack using computational fluid dynamics technique*, Journal of Power Sources, 55 (1995), pp. 25-32.
[23] W. He, J. S. Yi and T. V. Nguyen, *Two-phase flow model of the cathode of PEM fuel cells using interdigitated flow fields,* AIChE Journal 46 (2000) pp. 2053-2064.
[24] I-M. Hsing and P. Futerko, *Two-dimensional simulation of water transport in polymer electrolyte fuel cells*, Chemical Engineering Science, 55 (2000), pp. 4209-4218.
[25] W. Jäger and A. Mikelić, *On the interface boundary condition of Beavers, Joseph, and Saffman,* SIAM J. Appl. Math., 60 (2000) pp. 1111-1127.
[26] M. Kaviany, *Principles of Heat Transfer in Porous Media*, Springer-Verlag, 1991.
[27] A. Kazim, H. T. Liu and P. Forges, *Modelling of performance of PEM fuel cells with conventional and interdigitated flow fields*, Journal of Applied Electrochemistry 29 (1999), pp. 1409-1416.
[28] A. C. King, J. Billingham and R. J. Cooper, *Performance modelling of solid oxide fuel cells,* Combustion theory and modelling, 5 (2001) pp. 639-667.
[29] J. H. Lee, T. R. Lalk and A. J. Appleby, *Modeling electrochemical performance in large scale proton exchange membrane fuel cell stacks,* Journal of Power Sources, 70 (1998) pp. 258-268.
[30] J. H. Lee and T. R. Lalk, *Modeling fuel cell stack systems,* Journal of Power Sources, 73 (1998) pp. 229-241.
[31] G. Maggio, V. Recupero and C. Mantegaza, *Modelling of temperature distribution in a solid polymer electrolyte fuel cell stack,* Journal of Power Sources, 62 (1996) pp. 167-174.
[32] M. J. Morgan and H. N. Shapiro, *Fundamentals of Engineering Thermodynamics*, Wiley, New York, 1993.
[33] T. V. Nguyen, *Modeling two-phase flow in the porous electrodes of proton exchange membrane fuel cells using the interdigitated flow fields,* Electrochemical Society Proceedings, 99-14 (2000) pp. 222-241.
[34] T. V. Nguyen and R. E. White, *A water and heat management model for proton-exchange-membrane fuel cells*, J. Electrochem. Soc. 140 (1993), pp. 2178-2186.
[35] J. A. Ochoa-Tapia and S. Whitaker, *Momentum jump condition at the boundary between a porous medium and a homogeneous fluid: inertial effects*, J. Porous Media, 1 (1998) pp. 201-217.
[36] J. A. Ochoa-Tapia and S. Whitaker, *Heat transfer at the boundary between a porous medium and a homogeneous fluid: the one-equation model*, J. Porous Media, 1 (1998) pp. 31-46.
[37] J. A. Prins-Jansen, J. D. Fehribach, K. Hemmes and J. H. W. deWit, *A three-phase homogeneous model for porous electrodes in molten-carbonate fuel cells,* J. Electrochem. Soc. 143 (1996), pp. 1617-1628.
[38] S. Shimpalee and S. Dutta, *Numerical prediction of temperature distribution in PEM fuel cells,* Numerical Heat Transfer, Part A, 38 (2000), pp. 111-128.
[39] D. Singh, D. M. Lu and N. Djilali, *A two-dimensional analysis of mass transport in proton exchange membrane fuel cells*, International Journal of Engineering Science 37 (1999), pp. 431-452.
[40] T. E. Springer, T. A. Zawodzinski and S. Gottesfeld, *Polymer electrolyte fuel cell model*, J. Electrochem. Soc. 138 (1991), pp. 2334-2342.
[41] R. Taylor and R. Krishna, *Multicomponent Mass Transfer,* Wiley, New York, 1993.

[42] D. Thirumalai and R. E. White, *Mathematical modeling of proton-exchange-membrane fuel-cell stacks,* J. Electrochem. Soc. 144 (1997), pp. 1717-1723.

[43] M. Uchida, Y. Fukuoka, Y. Sugawara, N. Eda and A. Ohta, *Effects of mictrostructure of carbon support in the catalyst layer on the performance of polymer-electrolyte fuel cells,* J. Electrochem. Soc. 143 (1996), pp. 2245-2252.

[44] M. W. Verbrugge and R. F. Hill, *Transport phenomena in perfluorosulfonic acid membranes during the passage of a current*, J. Electrochem. Soc. 137 (1990), pp. 1131-1138.

[45] Z. H. Wang, C. Y. Wang and K. S. Chen, *Two-phase flow and transport in the air cathode of proton exchange membrane fuel cells,* Journal of Power Sources, 94 (2001) pp. 40-50.

[46] S. Whitaker, *The Forchheimer equation: a theoretical development,* Transport in Porous Media, 25 (1996) pp. 27-61.

[47] S. Whitaker, *The method of volume averaging,* Kluwer, Dordrecht, 1999.

[48] J. S. Yi and T. V. Nguyen, *An along-the-channel model for proton exchange membrane fuel cells,* J. Electrochem. Soc. 145 (1998), pp. 1149-1159.

[49] J. S. Yi and T. V. Nguyen, *Multicomponent transport in porous electrodes of proton exchange membrane fuel cells using the interdigitated gas distributors*, J. Electrochem. Soc. 146 (1999), pp. 38-45.

Paper 2

A quantitative study of the effect of flow-distributor geometry in the cathode of a PEM fuel cell

Erik Birgersson and Michael Vynnycky

Department of Mechanics, FaxénLaboratoriet, KTH,
SE-100 44, Stockholm, Sweden

Abstract. An isothermal three-dimensional model describing mass, momentum and species transfer in the cathode of a proton exchange membrane fuel cell has been used to study four different flow distributors: interdigitated, coflow and counterflow channels, and a foam. A quantitative comparison of the results shows that the interdigitated channels can sustain the highest current densities, followed in descending order by the foam, the counterflow and the coflow channels. The foam yields the most uniform current density distribution at higher currents, but also induces the greatest pressure drop.

1. Introduction

In view of ever increasing levels of environmental pollution and thus a desire to replace the fossil-fuel-based economy with a cleaner alternative, the fuel cell has in recent years become a prime candidate as a power source for transport and stationary applications. The potential use of fuel cells range from distributed power sources and portable applications, such as laptops [**1**] or even for the future dismounted soldier [**2**], to vehicles.

One such type of cell is the proton exchange membrane fuel cell (PEMFC), a schematic representation of which is shown in figure 1. The basic cell consists of two porous electrodes, termed the anode and the cathode, separated by a proton conducting membrane. The porous electrodes are made of a composite material, containing carbon cloth and a hydrophobic agent, such as polytetrafluorethylene. Each electrode has a thin layer containing an electrocatalyst, such as platinum, that is dispersed on the carbon cloth and is in contact with the membrane, usually a hydrated perfluorinated sulfonic acid polymer. In addition a bipolar plate, essentially graphite into which flow and cooling channels have been machined, is situated adjacent to each electrode. In the course of operation, an oxidant, usually oxygen from air which is either dry or humidified to some extent, is fed at the inlet on the cathode side and transported to the electrolyte/cathode interface; the fuel on the other hand, normally hydrogen, is fed at the anode inlet and is transported to the electrolyte/anode interface. The reactions occurring at these interfaces are then

$$2H_2 \rightarrow 4H^+ + 4e^- \quad \text{at the anode,} \tag{1.1}$$

$$O_2 + 4H^+ + 4e^- \rightarrow 2H_2O \quad \text{at the cathode,} \tag{1.2}$$

which are termed the hydrogen oxidation reaction (HOR) and the oxygen reduction reaction (ORR), respectively. Thus, the protons produced at the anode

are transported through the membrane to the cathode, whilst the electrons can drive a load through an external circuit.

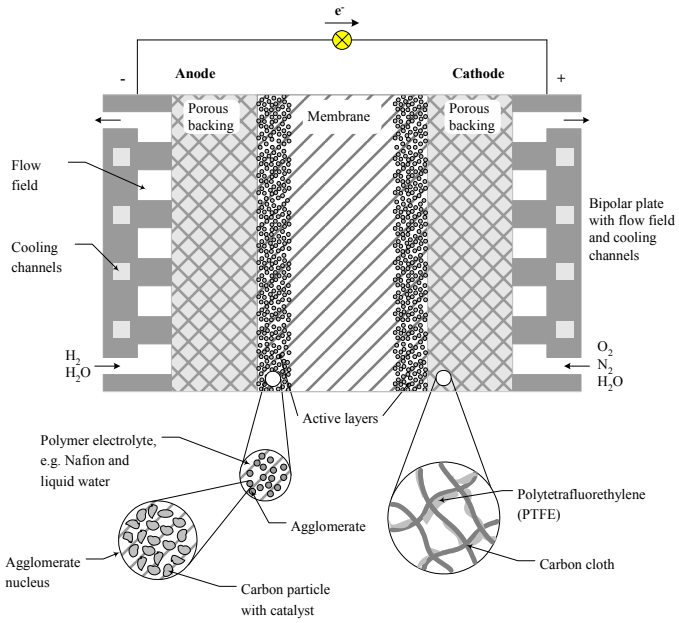

Figure 1. Schematic of a proton exchange membrane fuel cell.

During recent years, a number of mathematical models have been developed in an attempt to understand the phenomena occurring in a PEM fuel cell. Since a complete fuel cell model would have to address mass, momentum, species and heat transfer in gas and liquid phases in a three-dimensional geometry, as well as the electrokinetics for the ORR and HOR, most models choose to focus on only some of these aspects at a time. The first models to appear were one-dimensional followed by two-dimensional, see [**11**] for a list of these models; lately three-dimensional models, based on computational fluid dynamics, have also begun to appear [**5-9**]. Dutta, Shimpalee and van Zee considered first a straight channel flow under isothermal conditions [**5**], followed later by a model for flow in a serpentine channel [**6**]; most recent work extends [**5**] to take into account heat transfer for a straight channel flow [**7**]. Costamagna considers non-isothermal conditions and treats the flow distributor as a porous material [**8**]. Berning [**9**] introduces a non-isothermal two-phase model for a straight channel, with a simplified two-phase treatment in the porous backings, neglecting the interaction between the liquid and gaseous phase and assuming one-phase flow in the flow channel. However, none of the above consider in a quantitative and comparative way the effect of flow distributor geometry on fuel cell performance.

To extend the work on three-dimensional modelling, we have conducted a quantitative comparison of the performance of four common flow distributors: parallel channels, run in both coflow and counterflow, interdigitated channels and a porous distributor, such as a foam. To limit the computational requirements, we assume that the anode side is run at such conditions that it is able to fully sustain any current created at the cathode, i.e. a fully moisturized anode that is run at high stoichiometry. In addition, we assume that sufficient cooling is provided to keep the cathode isothermal, a not unreasonable preliminary assumption in view of the temperature distributions obtained by [**7, 9**], which show that the temperature only varies by a couple of degrees in the cathode. These assumptions enable us then to consider isothermal, 3-component, gas-phase, three-dimensional laminar flow in the flow distributor and adjacent porous backing on the cathode side only.

The mathematical model, consisting of mass, momentum and species transport equations, as well as the geometries of the flow distributors considered, are introduced in Section 2. We focus also on how a rather detailed agglomerate model for the electrochemical aspects of the active layer, derived by [**3**], can be simply implemented into the present formulation. Details of the numerical solver used, CFX-4.4 [**10**], followed by its verification against an asymptotic solution obtained previously [**11**], are given in Section 3. The results from different flow distributors are then compared and discussed in Section 4. We finish with conclusions in Section 5.

2. Model description

2.1. Flow-distributor geometry. The electrochemical reactions that occur at the active layers depend on a sufficiently fast transport of reactants to, and products away from, the active sites so as to limit concentration overpotentials. Towards this end, the bipolar plates contain grooved channels, which can take a number of different shapes. Amongst the most common designs today are:

- **(a):** *parallel channels*, with only one pass over the porous backing, run in coflow, as shown in figure 2a.
- **(b):** *parallel channels*, with only one pass over the porous backing, run in counterflow, as shown in figure 2a.
- **(c):** *interdigitated channels*, where channels are terminated, in order to force the flow into the porous backing, see figure 2b.
- **(d):** *a porous material*, such as a foam; here, the entire surface of the porous backing is in contact with the gas flow, see figure 2c, in contrast to the channel based flow distributors, which contain 'dead' zones between the channels.
- **(e):** *serpentine flow channels*, comprising one long channel with many passes over the porous backing.
- **(f):** *a combination of some of the above*, e.g. (a) and (e), (b) and (e).

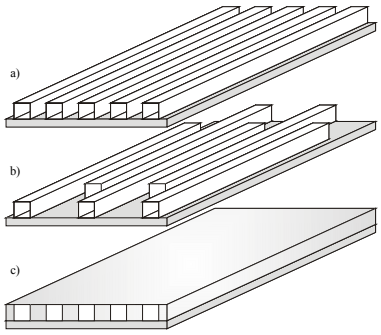

Figure 2. Schematic of the flow distributors considered: a) parallel channels which can be run in coflow or counterflow; b) interdigitated flow channels; c) foam.

We focus here on (a)-(d).

2.2. Governing equations.

2.2.1. *Flow channels.* In the flow channels, we solve for the momentum and continuity of mass, given by

$$\nabla \cdot (\rho \mathbf{v}) = 0, \tag{2.1}$$

$$\nabla \cdot (\rho \mathbf{v} \otimes \mathbf{v}) = -\nabla \left(p + \frac{2}{3}\mu \nabla \cdot \mathbf{v} \right) + \nabla \cdot \left(\mu \left((\nabla \mathbf{v}) + (\nabla \mathbf{v})^{\mathrm{T}} \right) \right), \tag{2.2}$$

where $\mathbf{v}$ is the velocity, ρ is the density, p is the pressure and μ is the dynamic viscosity. The transport equations for the ternary gas mixture, comprising oxygen, water and nitrogen are

$$\nabla \cdot \left(\rho \mathbf{v} \begin{pmatrix} w_{\mathrm{O_2}} \\ w_{\mathrm{H_2O}} \end{pmatrix} \right) = \nabla \cdot \left(\rho \mathbf{D} \begin{bmatrix} \nabla w_{\mathrm{O_2}} \\ \nabla w_{\mathrm{H_2O}} \end{bmatrix} \right), \tag{2.3}$$

where $w_{\mathrm{O_2}}$ and $w_{\mathrm{H_2O}}$ are the mass fractions of oxygen and water and $\mathbf{D}$ is the diffusion tensor.

2.2.2. *Porous backing/Foam.* For porous regions, we have to define superficial and intrinsic properties. Superficial averages are defined as

$$\langle \phi \rangle \equiv \frac{1}{\mathcal{V}} \int_{\mathcal{V}} \phi \mathrm{d}\mathcal{V}, \tag{2.4}$$

and intrinsic as

$$\langle \phi \rangle^{(\mathrm{g})} \equiv \frac{1}{\mathcal{V}^{(\mathrm{g})}} \int_{\mathcal{V}} \phi \mathrm{d}\mathcal{V}, \tag{2.5}$$

where $\mathcal{V}$ is the total volume of the **R**epresentative **E**lementary **V**olume (**REV**) and $\mathcal{V}^{(\mathrm{g})}$ is the volume of the gas in the REV. With the porosity, $\gamma = \mathcal{V}^{(\mathrm{g})}/\mathcal{V}$, the two averages are related through

$$\langle \phi \rangle = \gamma \langle \phi \rangle^{(\mathrm{g})}. \tag{2.6}$$

Conservation of mass and momentum is given respectively by

$$\nabla \cdot \left(\langle \rho \rangle^{(\mathrm{g})} \langle \mathbf{v} \rangle \right) = 0, \tag{2.7}$$

$$\nabla \cdot \left(\langle \rho \rangle^{(\mathrm{g})} \langle \mathbf{v} \rangle \otimes \langle \mathbf{v} \rangle \right) + \mu \mathbf{K}^{-1} \cdot \langle \mathbf{v} \rangle = -\nabla \left(\langle p \rangle^{(\mathrm{g})} + \frac{2}{3} \frac{\mu}{\gamma} \nabla \cdot \langle \mathbf{v} \rangle \right) + \nabla \cdot \left(\frac{\mu}{\gamma} \left(\nabla \langle \mathbf{v} \rangle + \left(\nabla \langle \mathbf{v} \rangle \right)^{\mathrm{T}} \right) \right), \tag{2.8}$$

where $\mathbf{K}$ is the permeability tensor.

The species transport equations are described by

$$\nabla \cdot \left(\langle \rho \rangle^{(\mathrm{g})} \langle \mathbf{v} \rangle \begin{pmatrix} \langle w_{\mathrm{O_2}} \rangle^{(g)} \\ \langle w_{\mathrm{H_2O}} \rangle^{(g)} \end{pmatrix} \right) = \nabla \cdot \left(\langle \rho \rangle^{(\mathrm{g})} \gamma \langle \mathbf{D} \rangle^{(\mathrm{g})} \begin{bmatrix} \nabla \langle w_{\mathrm{O_2}} \rangle^{(\mathrm{g})} \\ \nabla \langle w_{\mathrm{H_2O}} \rangle^{(\mathrm{g})} \end{bmatrix} \right), \tag{2.9}$$

where $\langle \mathbf{D} \rangle^{(\mathrm{g})}$ is the total mass diffusion tensor, containing contributions from an intrinsic effective mass diffusion tensor and an intrinsic hydrodynamic dispersion tensor. For a more detailed discussion of these, see [**11**].

2.3. Boundary conditions.

2.3.1. *Inlet.* At the inlet, we prescribe the normal velocity and the gas composition for the channel distributors:

$$\mathbf{v} \cdot \mathbf{e_x} = U^{\mathrm{in}}, \ \mathbf{v} \cdot \mathbf{e_y} = \mathbf{v} \cdot \mathbf{e}_z = 0, \ w_{\mathrm{O_2}} = w_{\mathrm{O_2}}^{\mathrm{in}}, \ w_{\mathrm{H_2O}} = w_{\mathrm{H_2O}}^{\mathrm{in}}; \tag{2.10}$$

in addition, for the counterflow distributor, we require

$$\mathbf{v} \cdot \mathbf{e_x} = -U^{\mathrm{in}}, \ \mathbf{v} \cdot \mathbf{e_y} = \mathbf{v} \cdot \mathbf{e}_z = 0, \ w_{\mathrm{O_2}} = w_{\mathrm{O_2}}^{\mathrm{in}}, \ w_{\mathrm{H_2O}} = w_{\mathrm{H_2O}}^{\mathrm{in}}, \tag{2.11}$$

for the second channel (see figure 3b);

For the foam:

$$\langle \mathbf{v} \rangle \cdot \mathbf{e_x} = U^{\mathrm{in}}, \ \langle \mathbf{v} \rangle \cdot \mathbf{e_y} = \langle \mathbf{v} \rangle \cdot \mathbf{e_z} = 0, \ \langle w_{\mathrm{O_2}} \rangle^{(\mathrm{g})} = w_{\mathrm{O_2}}^{\mathrm{in}}, \ \langle w_{\mathrm{H_2O}} \rangle^{(\mathrm{g})} = w_{\mathrm{H_2O}}^{\mathrm{in}}. \tag{2.12}$$

2.3.2. *Outlet.* At the outlet, we specify the pressure and the streamwise gradients of the velocities and species are set to zero, corresponding to fully developed flow conditions. For the channels:

$$p = p^{\mathrm{out}}, \tag{2.13}$$

$$\mathbf{e_x} \cdot \left(\nabla \mathbf{v} + (\nabla \mathbf{v})^{\mathrm{T}} \right) \cdot \mathbf{e_y} = 0, \tag{2.14}$$

$$\mathbf{e_x} \cdot \left(\nabla \mathbf{v} + (\nabla \mathbf{v})^{\mathrm{T}} \right) \cdot \mathbf{e_z} = 0, \tag{2.15}$$

$$\mathbf{e_x} \cdot \nabla w_{\mathrm{O_2}} = \mathbf{e_x} \cdot \nabla w_{\mathrm{H_2O}} = 0; \tag{2.16}$$

correspondingly, for the foam:

$$\langle p \rangle^{(\mathrm{g})} = p^{\mathrm{out}}, \tag{2.17}$$

$$\mathbf{e_x} \cdot \left(\nabla \langle \mathbf{v} \rangle + (\nabla \langle \mathbf{v} \rangle)^{\mathrm{T}} \right) \cdot \mathbf{e_y} = 0, \tag{2.18}$$

$$\mathbf{e_x} \cdot \left(\nabla \langle \mathbf{v} \rangle + (\nabla \langle \mathbf{v} \rangle)^{\mathrm{T}} \right) \cdot \mathbf{e_z} = 0, \tag{2.19}$$

$$\mathbf{e_x} \cdot \nabla \langle w_{\mathrm{O_2}} \rangle^{(\mathrm{g})} = \mathbf{e_x} \cdot \nabla \langle w_{\mathrm{H_2O}} \rangle^{(\mathrm{g})} = 0. \tag{2.20}$$

2.3.3. *Walls.* At the walls of the channels, we specify no-slip, no normal flow and no componental flux:

$$\mathbf{v} = \mathbf{0}, \tag{2.21}$$

$$\mathbf{n} \cdot \nabla w_{\mathrm{O_2}} = \mathbf{n} \cdot \nabla w_{\mathrm{H_2O}} = 0, \tag{2.22}$$

where $\mathbf{n}$ is the unit normal to a wall. In the porous backing and foam, zero shear stress, no normal flow and no componental flux conditions are applied; these are, respectively,

$$\mathbf{n} \cdot \left(\nabla \langle \mathbf{v} \rangle + (\nabla \langle \mathbf{v} \rangle)^{\mathrm{T}} \right) \cdot \mathbf{t} = 0, \tag{2.23}$$

$$\mathbf{n} \cdot \langle \mathbf{v} \rangle = 0, \tag{2.24}$$

$$\mathbf{n} \cdot \nabla \langle w_{\mathrm{O_2}} \rangle^{(\mathrm{g})} = \mathbf{n} \cdot \nabla \langle w_{\mathrm{H_2O}} \rangle^{(\mathrm{g})} = 0, \tag{2.25}$$

where $\mathbf{t}$ is the unit tangent to a wall.

2.3.4. *Symmetry conditions.* The flow distributors considered in this paper are all of periodic character, see figure 2, allowing us to reduce the computational domain for each by introducing unit cells, see figure 3, with the appropriate symmetry conditions. For the foam and porous backing:

$$\mathbf{n} \cdot \left(\nabla \langle \mathbf{v} \rangle + (\nabla \langle \mathbf{v} \rangle)^{\mathrm{T}} \right) \cdot \mathbf{t} = 0, \tag{2.26}$$

$$\mathbf{n} \cdot \langle \mathbf{v} \rangle = 0, \tag{2.27}$$

$$\mathbf{n} \cdot \nabla \langle w_{\mathrm{O_2}} \rangle^{(\mathrm{g})} = \mathbf{n} \cdot \nabla \langle w_{\mathrm{H_2O}} \rangle^{(\mathrm{g})} = 0; \tag{2.28}$$

correspondingly, for the channels:

$$\mathbf{n} \cdot \left(\nabla \mathbf{v} + (\nabla \mathbf{v})^{\mathrm{T}} \right) \cdot \mathbf{t} = 0, \tag{2.29}$$

$$\mathbf{n} \cdot \mathbf{v} = 0, \tag{2.30}$$

$$\mathbf{n} \cdot \nabla w_{\mathrm{O_2}} = \mathbf{n} \cdot \nabla w_{\mathrm{H_2O}} = 0. \tag{2.31}$$

2.3.5. *Channel/porous backing interface.* At the interface between the porous backing and the flow channels, we couple the point wise velocities, normal and shear stresses in the plain fluid (flow channels) with their superficial counterparts in the porous medium. The mass fractions and fluxes of oxygen and water are continuous across the interface.

2.3.6. *Active region/porous backing interface.* The active region in the cathode is sufficiently thin to allow us to treat it as a boundary condition for the porous backing. Using Faraday's Law, the mass fluxes of oxygen and water can be found as

$$\langle \mathbf{n}_{\mathrm{O_2}} \rangle \cdot \mathbf{e_y} = -\frac{M_{\mathrm{O_2}} \langle \mathbf{i} \rangle \cdot \mathbf{e_y}}{4F}, \tag{2.32}$$

$$\langle \mathbf{n}_{\mathrm{H_2O}} \rangle \cdot \mathbf{e_y} = \frac{(1+2\alpha) M_{\mathrm{H_2O}} \langle \mathbf{i} \rangle \cdot \mathbf{e_y}}{2F}, \tag{2.33}$$

where $\langle \mathbf{n}_{\mathrm{O_2}} \rangle$ and $\langle \mathbf{n}_{\mathrm{H_2O}} \rangle$ are the mass fluxes, α is the amount of water dragged through the membrane with each proton, M_{i} is the molecular mass of species i, $\langle \mathbf{i} \rangle$ is the superficial current density and F is Faraday's constant. The superficial velocity from the reaction can be derived from the the theory of multicomponent mass transfer as

$$\langle \rho \rangle^{(\mathrm{g})} \langle \mathbf{v} \rangle \cdot \mathbf{e_y} = \frac{\langle \mathbf{i} \rangle \cdot \mathbf{e_y}}{4F} \left((2+4\alpha) M_{\mathrm{H_2O}} - M_{\mathrm{O_2}} \right). \tag{2.34}$$

2.4. Constitutive relations. Assuming an ideal gas, the gas density can be found from

$$\rho = \frac{pM}{RT}, \tag{2.35}$$

where $M = (w_{\mathrm{O_2}}/M_{\mathrm{O_2}} + w_{\mathrm{H_2O}}/M_{\mathrm{H_2O}} + w_{\mathrm{N_2}}/M_{\mathrm{N_2}})^{-1}$ is the mean molecular mass, R is the universal gas constant and T is the temperature. The mass fraction of nitrogen is given by

$$w_{\mathrm{N_2}} = 1 - w_{\mathrm{O_2}} - w_{\mathrm{H_2O}}. \tag{2.36}$$

We note here that the molar fractions x_{i} are related to the mass fractions w_{i} by

$$x_{\mathrm{i}} = \frac{w_{\mathrm{i}} M}{M_{\mathrm{i}}}. \tag{2.37}$$

Furthermore, in the most general case, the dynamic viscosity, μ, is also a function of the composition, but for simplicity it is considered constant in this paper. The corresponding constitutive properties in the porous backing and foam are the same, but based on intrinsic values.

An expression for the diffusion tensor [**15**] can be found from the diffusion coefficients $\widetilde{D}_{ij}$ for the molar diffusion flux, relative to a molar-averaged velocity frame, as

$$\widetilde{D}_{11} = \mathcal{D}_{\mathrm{O_2,N_2}} (x_{\mathrm{O_2}} \mathcal{D}_{\mathrm{H_2O,N_2}} + (1 - x_{\mathrm{O_2}}) \mathcal{D}_{\mathrm{O_2,H_2O}})/S, \tag{2.38}$$

$$\widetilde{D}_{12} = x_{\mathrm{O_2}} \mathcal{D}_{\mathrm{H_2O,N_2}} (\mathcal{D}_{\mathrm{O_2,N_2}} - \mathcal{D}_{\mathrm{O_2,H_2O}})/S, \tag{2.39}$$

$$\widetilde{D}_{21} = x_{\mathrm{H_2O}} \mathcal{D}_{\mathrm{O_2,N_2}} (\mathcal{D}_{\mathrm{H_2O,N_2}} - \mathcal{D}_{\mathrm{O_2,H_2O}})/S, \tag{2.40}$$

$$\widetilde{D}_{22} = \mathcal{D}_{\mathrm{H_2O,N_2}} (x_{\mathrm{H_2O}} \mathcal{D}_{\mathrm{O_2,N_2}} + (1 - x_{\mathrm{H_2O}}) \mathcal{D}_{\mathrm{O_2,H_2O}})/S, \tag{2.41}$$

$$S = x_{\mathrm{O_2}} \mathcal{D}_{\mathrm{H_2O,N_2}} + x_{\mathrm{H_2O}} \mathcal{D}_{\mathrm{O_2,N_2}} + x_{\mathrm{N_2}} \mathcal{D}_{\mathrm{O_2,H_2O}}, \tag{2.42}$$

where $\mathcal{D}_{ij}$ are the binary Maxwell-Stefan diffusion coefficients. Since we use the mass diffusion flux relative to the mass-averaged velocity**,** the following transformation is required:

$$\mathbf{D} = \mathbf{B}\mathbf{W}\mathbf{X}^{-1}\widetilde{\mathbf{D}}\mathbf{X}\mathbf{W}^{-1}\mathbf{B}^{-1}, \tag{2.43}$$

$$\mathbf{B} = \delta_{\mathrm{ij}} - w_{\mathrm{i}}\left(1 - \frac{w_{\mathrm{n}}x_{\mathrm{j}}}{x_{\mathrm{n}}w_{\mathrm{j}}}\right), \quad \mathrm{i,j} = 1,2,\ \mathrm{n} = 3, \tag{2.44}$$

$$\mathbf{X} = x_{\mathrm{i}}\delta_{\mathrm{ij}}, \quad \mathrm{i,j} = 1,2, \tag{2.45}$$

$$\mathbf{W} = w_{\mathrm{i}}\delta_{\mathrm{ij}}, \quad \mathrm{i,j} = 1,2, \tag{2.46}$$

where δ_{ij} is the Kronecker delta. The binary Maxwell-Stefan diffusion coefficients are corrected for pressure and temperature via

$$\mathcal{D}_{\mathrm{ij}}(T,p) = \frac{p_0}{p}\left(\frac{T}{T_0}\right)^{\frac{3}{2}}\mathcal{D}_{\mathrm{ij}}(T_0,p_0), \tag{2.47}$$

stemming from kinetic gas theory [**12**]. The cross terms in the diffusion tensor $\mathbf{D}$ are around one to two orders of magnitude lower for the operating parameters in this study than the diagonal terms, allowing us to neglect their contributions, whence

$$\mathbf{D} = \begin{bmatrix} D_{11} & 0 \\ 0 & D_{22} \end{bmatrix}. \tag{2.48}$$

In the porous media, i.e. in the foam and porous backing, we apply a Bruggeman correlation for the superficial effective mass diffusion tensor

$$\langle\mathbf{D}\rangle = \gamma^{\frac{3}{2}}\mathbf{D}. \tag{2.49}$$

The permeabilities of the porous backing and foam are taken to be isotropic

$$\mathbf{K} = \kappa\delta_{\mathrm{ij}}, \tag{2.50}$$

where κ is the permeability.

2.5. Electrokinetics and the active layer. An expression is still required for the current density $\langle\mathbf{i}\rangle\cdot\mathbf{e_y}$ given in equation (2.34) . A novel feature of this paper is to implement an expression from an agglomerate model derived by Jaouen *et al.* [**3**], and subsequently validated experimentally [**4**]. Although [**3**] considers an active layer of finite thickness, it is possible to demonstrate that, for our purposes, the active layer need not be resolved explicitly, but rather can be treated implicitly as a boundary condition. Some further details are as follows.

The volumetric current density $\langle i_{\mathrm{v}}\rangle$, given by [**3**], is approximated as

$$\langle i_{\mathrm{v}}\rangle = \mathcal{A}i_0\left(1-\gamma_{\mathrm{pol}}\right)\left(1-\gamma_{\mathrm{a}}\right)\exp\left(-\frac{\alpha_{\mathrm{r}}F}{RT}\eta\right)\mathfrak{F}\frac{\langle c_{\mathrm{O_2}}\rangle^{(\mathrm{g})}}{c_{\mathrm{O_2}}^{\mathrm{ref}}} \tag{2.51}$$

where $\mathcal{A}i_0$ is the volumetric exchange current density in the agglomerates, γ_{pol} is the volume fraction of the polymer electrolyte in the agglomerate nucleus, $\langle c_{\mathrm{O_2}}\rangle^{(\mathrm{g})} = \langle w_{\mathrm{O_2}}\rangle^{(\mathrm{g})}\langle\rho\rangle^{(\mathrm{g})}/M_{\mathrm{O_2}}$ is the molar concentration of oxygen, α_r is the cathodic transfer coefficient for the ORR, n is the number of electrons consumed

in the ORR per oxygen molecule, η is the overpotential at the cathode (defined negative), and γ_{a} is the volume fraction of pores in the active layer. $\mathfrak{F}$ is the nucleus effectiveness factor, defined as

$$\mathfrak{F} = \frac{3}{\Upsilon r}\left(\frac{1}{\tanh(\Upsilon r)} - \frac{1}{\Upsilon r}\right), \tag{2.52}$$

with Υ given by

$$\Upsilon = \sqrt{\frac{\mathcal{A} i_0 \left(1-\gamma_{\mathrm{pol}}\right) \exp\left(-\frac{\alpha_{\mathrm{a}} F}{RT}\eta\right)}{nF\mathfrak{D}}}, \tag{2.53}$$

where $\mathfrak{D}$ is an effective oxygen permeability in the agglomerates and r is the radius of the agglomerate nucleus. This agglomerate model was validated by [**4**] for a small PEM fuel cell with an area of 2 cm^2 at conditions well above the stoichiometric flow rate, allowing the cell there to be modelled one-dimensionally, since concentration gradients in the streamwise direction in the cathode can be neglected. In this paper, however, the aim is to capture and study two- and three-dimensional effects. The one-dimensional agglomerate model can be used for this purpose by noting that the geometry of the active layer studied is slender, i.e. its thickness, h_{a}, is much smaller than its width (w) and breadth (L), implying that only gradients in the normal direction in the active layer will contribute to mass transfer; consequently, this allows us to treat the active layer locally as one-dimensional. Although we omit the details here, it is possible to show by scale analysis that we will not have any gradients of oxygen in the normal direction in the active layer, since the magnitude of the diffusion coefficient in the agglomerates is $O(10^{-11})$ $\mathrm{m}^2\mathrm{s}^{-1}$, as compared to $O(10^{-5})$ $\mathrm{m}^2\mathrm{s}^{-1}$ in the pores. The additional approximation of reducing the active layer to a boundary condition corresponds to an infinite effective proton conductivity in the the active layer. The total current density is then given locally by $\langle \mathbf{i} \rangle \cdot \mathbf{e_y} = \langle i \rangle = \langle i_{\mathrm{v}} \rangle \, h_{\mathrm{a}}$.

Jaouen *et al.* [**3**] discerned four different regimes, where the Tafel slope doubles or even quadruples, and subsequently supplied the experimental validation to support these [**4**]. In regime 1, the active layer is controlled by Tafel kinetics and is first order in the oxygen concentration. Regime 2 displays a doubling of the Tafel slope, due to the active layer being governed by Tafel kinetics and oxygen diffusion in the agglomerates, but still remains first order in the oxygen concentration. A doubling of the Tafel slope is observed in the third regime, where the active layer is controlled by the Tafel kinetics, in addition to proton migration. The oxygen dependence here is half-order. The final regime, the fourth, shows a quadrupling of the Tafel slope, and is attributable to an active layer controlled by Tafel kinetics, proton migration and oxygen diffusion in the agglomerates. The oxygen dependence is half-order, as in regime 3.

By assuming that we have no resistance to proton migration, we limit the validity of the expression to regimes 1 and 2, i.e. to an active layer controlled by Tafel kinetics at low overpotentials, and at higher overpotentials by Tafel kinetics coupled with oxygen diffusion resistance in the agglomerates. We are

thus able to capture the doubling of the Tafel slope due to mass transfer limitations in the agglomerates, although the doubling due to proton migration resistance and a quadrupling of the slope are not modelled.

Finally, we note that of more use, as regards judging fuel cell performance, than the overpotential, η, is the cell voltage, E_{cell}, where

$$\eta = E_{\text{cell}} - E_0, \tag{2.54}$$

and E_0 is the equilibrium potential.

3. Numerics and verification

A commercial computational fluid dynamics code, CFX-4.4, based on finite volumes, was used to implement the model outlined above. As can be seen in figure 2, all of the flow distributors are periodic in the spanwise direction. Hence, a representative computational unit cell, with symmetry boundary conditions on both sides in the spanwise coordinate, can be introduced. The unit cells for the distributors are chosen so that the area of the active layer and the contact area between the channels and porous backing are the same for all, with the exception of the foam, which covers the entire porous backing as depicted in figure 3.

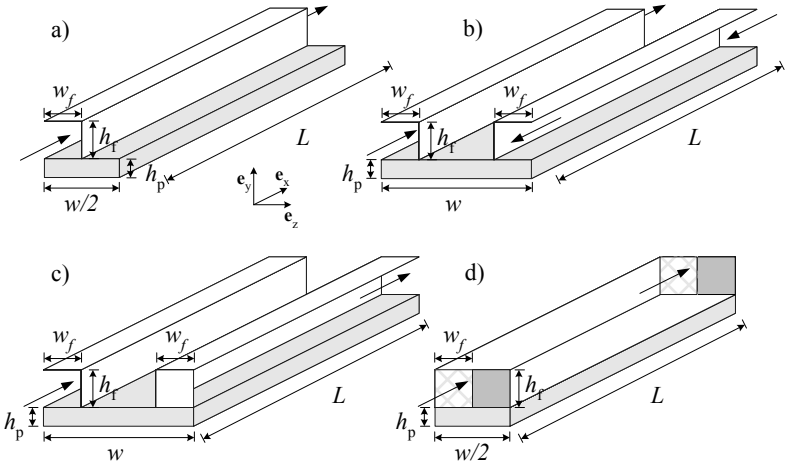

Figure 3. Schematic of the computational unit cells: a) parallel channels run in coflow; b) parallel channels run in counterflow; c) interdigitated channels; d) foam.

Using a structured mesh, each flow distributor with porous backing was resolved as follows:

(a): *parallel channels run in coflow*; the channel contained 10^4 computational cells and the porous backing 2×10^4 cells, giving a total of

3×10^4 cells. Mesh independence was assured by comparing with a mesh comprising 1.2×10^5 cells and the difference was found to be $\sim 1\%$ for the average current density.

(b): *parallel channels run in counterflow*; the two channels with 10^4 cells each and the porous backing with 4×10^4 cells, giving a total of 6×10^4 cells. Mesh independence was assured by comparing with a mesh comprising 2×10^5 cells and the difference was found to be $\sim 1\%$ for the average current density.

(c): *interdigitated channels*; the two channels with 10^4 cells each and the porous backing with 4×10^4, giving a total of 6×10^4 cells. Mesh independence was assured by comparing with a mesh comprising 2×10^5 cells and the difference was found to be $\sim 4\%$ for the average current density. At higher currents, i.e. $\langle i \rangle > 4$ Acm^{-2}, more than 6×10^4 cells were necessary to resolve the flow in the porous backing. We did not pursue these higher current densities, however.

(d): *foam*; the foam and porous backing, each with 2×10^4 cells, giving a total of 4×10^4 cells. Mesh independence was assured by comparing with a mesh comprising 1.6×10^5 cells and the difference was found to be $\sim 1\%$ for the average current density.

The computations, carried out on a 500 MHz Compaq Alphaserver with 3 GB RAM, required about 1-2 hours for lower current densities and about 12 hours for higher.

The numerical code was verified via asymptotic solutions [**11**]. [**11**] showed that for a slender two-dimensional geometry, consisting of a flow channel adjacent to the porous backing, closed form solutions could be found for $\Delta = 1/\left(Re\sigma^2\right) \gg 1$, where $Re\left(= \frac{\rho U^{\text{in}} L}{\mu}\right)$ is the Reynolds number, and $\sigma = h_{\text{f}}/L$, with h_{f} and L as the height and length of the flow distributor. The geometry is depicted in figure 4 in dimensional form.

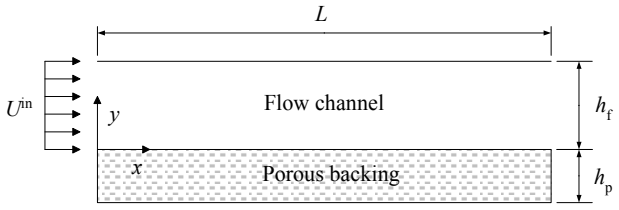

Figure 4. The two-dimensional cathode with a flow distributor above the porous backing.

For the asymptotic analysis, the governing equations are scaled so that $X = x/L$, $Y = y/h_{\text{f}}$. For a current density which can be written nondimensionally on the form $I = \langle x_{\text{O}_2} \rangle^{(\text{g})}$, where $I = \langle i \rangle / [i]$ and $[i]$ is the current density scale,

the leading order solution was found to be given by

$$\mathcal{A}\log\left(\frac{\zeta_{\mathrm{O_2}}(X)\left(\Phi\zeta_{\mathrm{O_2}}(0)+1\right)}{\zeta_{\mathrm{O_2}}(0)\left(\Phi\zeta_{\mathrm{O_2}}(X)+1\right)}\right)-(\mathcal{A}\Phi-\mathcal{B})\left(\frac{\zeta_{\mathrm{O_2}}(X)-\zeta_{\mathrm{O_2}}(0)}{\left(\Phi\zeta_{\mathrm{O_2}}(X)+1\right)\left(\Phi\zeta_{\mathrm{O_2}}(0)+1\right)}\right) = \frac{\Omega X}{4\rho_0(0)\left(\Phi\zeta_{\mathrm{O_2}}(0)+1\right)},$$

where

$$\mathcal{A} = \frac{1}{\mathcal{M}_{\mathrm{N_2}}}\left[(\mathcal{M}_{\mathrm{H_2O}}-\mathcal{M}_{\mathrm{N_2}})\left(\frac{(2+4\alpha)\,\zeta_{\mathrm{O_2}}(0)+\zeta_{\mathrm{H_2O}}(0)}{\Phi\zeta_{\mathrm{O_2}}(0)+1}\right)-1\right],$$

$$\mathcal{B} = \frac{1}{\mathcal{M}_{\mathrm{N_2}}}\left[(\mathcal{M}_{\mathrm{O_2}}-\mathcal{M}_{\mathrm{N_2}})+(\mathcal{M}_{\mathrm{H_2O}}-\mathcal{M}_{\mathrm{N_2}})\left(\frac{\Phi\zeta_{\mathrm{H_2O}}(0)-(2+4\alpha)}{\Phi\zeta_{\mathrm{O_2}}(0)+1}\right)\right],$$

and

$$\zeta_{\mathrm{O_2}} = \frac{x_{\mathrm{O_2}}}{\mathcal{M}},$$

$$\zeta_{\mathrm{H_2O}} = \frac{\left(1+\Phi\zeta_{\mathrm{O_2}}(X)\right)\zeta_{\mathrm{H_2O}}(0)+(2+4\alpha)\left(\zeta_{\mathrm{O_2}}(0)-\zeta_{\mathrm{O_2}}(X)\right)}{\Phi\zeta_{\mathrm{O_2}}(0)+1},$$

with $\mathcal{M}_{\mathrm{i}} = M_{\mathrm{i}}/[M]$, $\mathcal{M}$ $=M/[M]$, where $[M]$ is a molecular weight scale, $\Omega = \frac{[i][M]}{[\rho]U^{\mathrm{in}}F\sigma}$ and $\Phi = (2+4\alpha)\mathcal{M}_{H_2O} - \mathcal{M}_{O_2}$.

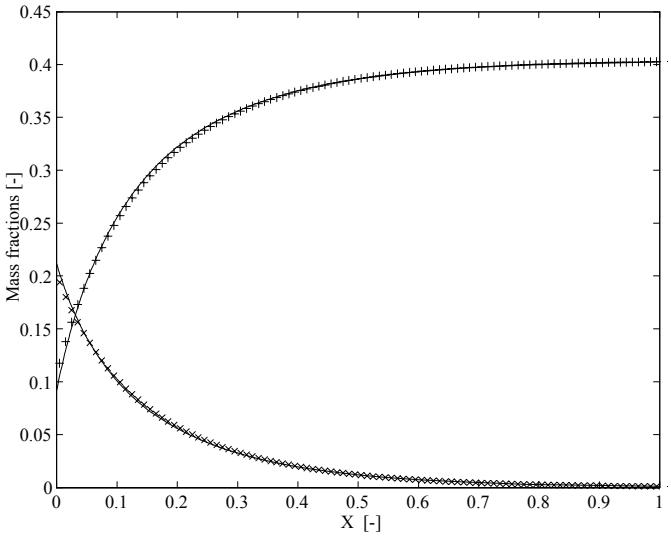

Figure 5. Verification of the CFX-4.4 code. (—) corresponds to analytical solutions and markers are for the CFX-4.4 solutions: water mass fraction (+); oxygen mass fraction (x).

For the agglomerate model applied here, we obtain the current density scale

$$[i] = \mathcal{A} i_0 \left(1 - \gamma_{\mathrm{pol}}\right) \left(1 - \gamma_{\mathrm{a}}\right) \exp\left(-\frac{\alpha_{\mathrm{r}} F}{RT}\eta\right) \mathfrak{F} \frac{h_{\mathrm{a}}[\rho]}{c_{\mathrm{O_2}}^{\mathrm{ref}}[M]},$$

whence $I \equiv \langle x_{\mathrm{O_2}} \rangle^{(\mathrm{g})}$ as required for the solution above.

Comparison, shown in figure 5, was carried out in terms of mass fraction profiles along the cathode. All parameters from the base case were used, see table I, but with $\Delta = 960$, $\sigma = 10^{-3}$ and $\Omega = 28.2$. The number of cells used for this 2D calculation in CFX-4.4 were 2000. The mass fractions obtained with CFX-4.4 agree well the ones obtained analytically.

Table I. Base-case parameters

Physical parameters:	
γ_{b}	0.3
γ_{f}	0.99
$\mathcal{D}_{\mathrm{O_2,H_2O}}$	3.98×10^{-5} m^{2}s^{-1} at 363 K, 1 atm [**3**]
$\mathcal{D}_{\mathrm{O_2,N_2}}$	2.95×10^{-5} m^{2}s^{-1} at 363 K, 1 atm [**3**]
$\mathcal{D}_{\mathrm{H_2}O,\mathrm{N_2}}$	4.16×10^{-5} m^{2}s^{-1} at 363 K, 1 atm [**3**]
E_0	1.18 V
$M_{\mathrm{O_2}}$	2.8×10^{-2} kg mol^{-1}
$M_{\mathrm{H_2O}}$	1.8×10^{-2} kg mol^{-1}
$M_{\mathrm{N_2}}$	3.2×10^{-2} kg mol^{-1}
κ_{p}	10^{-12} m^2
κ_{f}	10^{-10} m^2
μ	1.812×10^{-5} kgm^{-1}s^{-1}
F	96487 As mol^{-1}
α	0.3
R	8.314 Jmol^{-1}K^{-1}
$[M]$	10^{-2} kg/mol
$[\rho]$	1.0 kgm^{-3}
$p_{\mathrm{H_2O}}^{\mathrm{vap}}$	4.7×10^4 Nm^{-2} [**16**]

Operating conditions:	
p^{out}	1 atm
L	0.1 m
$\mathfrak{h}^{\text{in}}$	30%
T	80°C
h_{f}	10^{-3} m
h_{p}	3×10^{-4} m
w_{f}	5×10^{-4} m
w	2×10^{-3} m

Agglomerate model parameters:	
r	5×10^{-7} m
α_{r}	0.78
$\mathcal{A}i_0$	3×10^3 Am^{-3}
$\mathfrak{D}$	10^{-11} mol m^{-1}s^{-1}
h_{a}	10^{-5} m
γ_{a}	0.3
γ_{pol}	0.3
n	4
$c_{\text{O}_2}^{\text{ref}}$	6.2 mol m^{-3} at $\mathfrak{h} = 30\%$, 1 atm and 353 K

4. Results & Discussion

For each flow distributor, simulations were carried out for six different cell potentials, E_{cell}. However, rather than specifying the inlet velocity, U^{in}, we specify instead, as tends to be the practice in experimental work with fuel cells, the stoichiometry, ξ, which is defined by

$$\xi = \frac{\int_{A^{\text{in}}} n^{\text{in}}_{\text{O}_2} \, \text{dA}}{\int_{A^{\text{cat}}} \left\langle n^{\text{cat}}_{\text{O}_2} \right\rangle \text{dA}} = \frac{\rho U^{\text{in}} w^{\text{in}}_{\text{O}_2} A^{\text{in}}}{\frac{M_{\text{O}_2}}{4F} \int_{A^{\text{cat}}} \langle i \rangle \, \text{dA}'}, \tag{4.1}$$

where $n^{\text{in}}_{\text{O}_2}$ and $\left\langle n^{\text{cat}}_{\text{O}_2} \right\rangle$ are the mass fluxes of oxygen into the cathode and of the oxygen being consumed at the active layer, respectively, and A^{cat} and A^{in} are the total areas of the active layer and the inlet. This formulation implies that the inlet velocity is iterated for, its value depending on the current density obtained at the catalytic layer on the previous iteration. We also specify the relative humidity at the inlet, $\mathfrak{H}^{\text{in}}$, given by

$$\mathfrak{H}^{\text{in}} = \frac{x^{\text{in}}_{\text{H}_2\text{O}} p^{\text{in}}}{p^{\text{vap}}_{\text{H}_2\text{O}}}, \tag{4.2}$$

where $p^{\text{vap}}_{\text{H}_2\text{O}}$ is the vapour pressure of water; furthermore, since $x_{\text{O}_2}/x_{\text{N}_2} = 21/79$ and $x_{\text{O}_2} + x_{\text{H}_2O} + x_{\text{N}_2} = 1$, we have the inlet compositions for a given relative humidity as

$$x^{\text{in}}_{\text{H}_2\text{O}} = \mathfrak{H}^{\text{in}} \frac{p^{\text{vap}}_{\text{H}_2\text{O}}}{p^{\text{in}}}, \; x^{\text{in}}_{\text{O}_2} = \frac{1 - x^{\text{in}}_{\text{H}_2\text{O}}}{1 + 79/21}. \tag{4.3}$$

Consequently, $x^{\text{in}}_{\text{H}_2\text{O}}$ and $x^{\text{in}}_{\text{O}_2}$ must also be updated at every iteration.

Earlier work [**13, 14**] suggests that the interdigitated design should be capable of yielding higher current densities than either one of the straight channel designs considered here. Also, we expect that either the foam or the interdigitated channels give rise to the highest average current densities, since the interdigitated design forces the flow into the porous backing, whereas the foam covers the whole surface of the porous backing. Parallel channels run in counterflow might be expected to perform better than channels in coflow, as the former allows for alternating inlets and outlets, reducing the level of oxygen depletion along the channels. This is indeed the case, as can be seen in figure 6, where the polarization curves for the stoichiometries 1.5, 3 and 5 are shown. The interdigitated design allows for average current densities of 4 Acm^{-2} for cell potentials between 0.3 V and 0.4 V, depending on stoichiometry. Current densities ranging from 2 to 3.2 Acm^{-2} are obtainable with the foam. The counterflow gives somewhat higher current densities than the coflow design, especially for the higher stoichiometry.

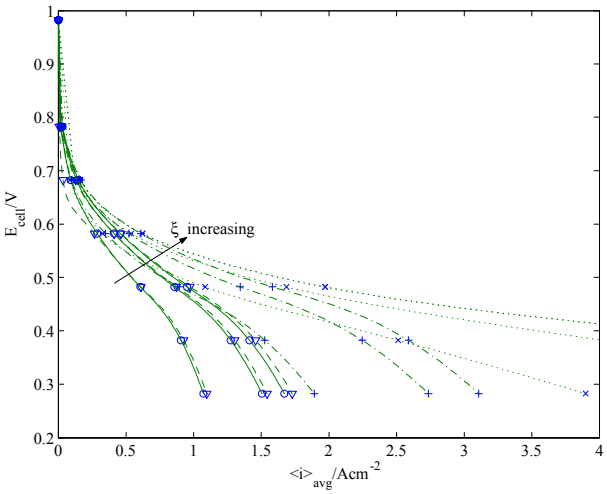

Figure 6. Polarisation curves for the different flow distributors at stoichiometry $\xi = 1.5$, 3, 5: coflow channels (o), counterflow channels (∇), interdigitated channels (x), foam (+).

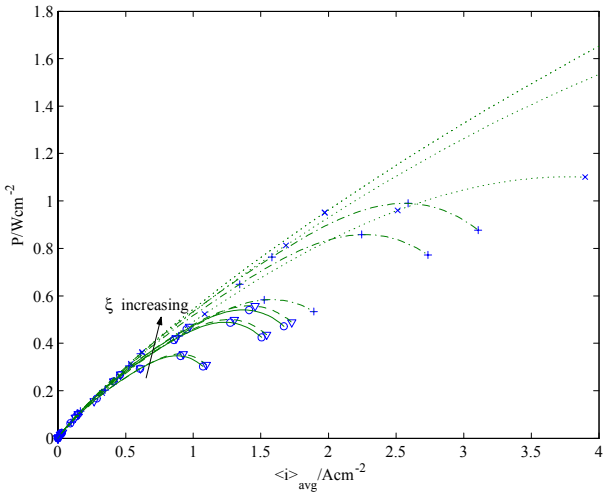

Figure 7. Power density, P, for the different flow distributors at stoichiometry $\xi = 1.5$, 3, 5: coflow channels (o), counterflow channels (∇), interdigitated channels (x), foam (+).

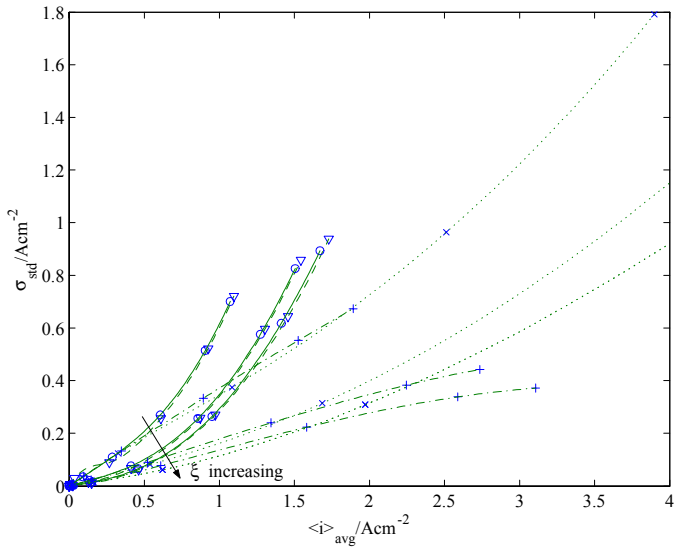

Figure 8. Standard deviation of the current density, σ_{std}, for the different flow distributors at stoichiometry $\xi = 1.5$, 3, 5: coflow channels (o), counterflow channels (∇), interdigitated channels (x), foam (+).

Figure 7 depicts the power density for the flow distributors. In the lower ranges of current density, $0 \sim 0.4$ Acm^{-2}, the power density is independent of the type of distributor used. As the current density is increased, differences between the flow designs become readily apparent, with the interdigitated sustaining the highest power densities, followed by the foam. The counterflow channels perform marginally better than the coflow channels.

The performance of a fuel cell is judged not only on the magnitude of current density that can be generated, but also on the uniformity of the current distribution at the active layer, since uniformity is linked to catalyst utilization and degradation. As a measure of the uniformity, we compare the standard deviation of the current density for each flow design, σ_{std}, defined by

$$\sigma_{\mathrm{std}} = \left(\frac{1}{A^{\mathrm{cat}}} \int_{A^{\mathrm{cat}}} \left(\langle i \rangle - \langle i \rangle_{\mathrm{avg}} \right)^2 \mathrm{dA}' \right)^{\frac{1}{2}}, \text{ where } \langle i \rangle_{\mathrm{avg}} = \frac{1}{A^{\mathrm{cat}}} \int_{A^{\mathrm{cat}}} \langle i \rangle \, \mathrm{dA}', \tag{4.4}$$

as illustrated in figure 8.

For all flow distributors, the distribution becomes more uniform as the stoichiometry is increased. At a stoichiometry of 1, all the oxygen that enters the cathode would be consumed; by increasing the stoichiometry, the flow becomes less depleted of oxygen, and is hence able to sustain higher current and a more uniform distribution. The parallel channels, run in co- and counterflow, exhibit

the highest deviations at current densities above ~ 0.4 Acm^{-2}, with the coflow being the less uniform of the two. At current densities below 1.5-2 Acm^{-2}, depending on stoichiometry, greatest uniformity is obtained for the interdigitated design, but the extent of the non-uniformity increases with the current; ultimately, the foam design gives the greatest uniformity. These findings are also reflected in figures A1-A4, where the local current density for different cell potentials is given. All distributors exhibit a more non-uniform current density as the overpotential is increased, i.e. as the cell voltage decreases. For coflow (see figure A1), the areas under the flow channels can sustain local higher current densities than those under the "rib" of the bipolar plate, where mass transfer becomes increasingly limiting with increasing overpotential. The cathode operated in counterflow behaves similarly (figure A2), but delivers a somewhat higher overall performance, as the counterflow arrangement allows for exiting air with a lower oxygen concentration in one channel to be balanced by incoming fresh air in the two adjacent channels. For the foam (figure A3), the local current density is a function of the streamwise coordinate only, although there are minor inlet and exit effects, which become somewhat more pronounced at higher current densities. This simplification is attributable to the inherent characteristic of the foam to cover the surface of the porous backing, in contrast to grooved channels in a bipolar plate comprising alternating regions of channels and ribs. Finally, the interdigitated arrangement (figure A4) displays an increasingly spanwise behaviour for the local current density at higher overpotentials. The overall flow increases for a given stoichiometry at higher current densities, leading to increased forced convective flow in the porous backing, whence the local current density becomes more even in the spanwise direction.

Keeping the pressure drop, $\Delta p \left(= p^{\text{in}} - p^{\text{out}}\right)$, at a minimum is of interest in terms of reducing operating costs for the fuel cell, whence the optimal flow distributor should be able to sustain high even current densities, whilst keeping the pressure drop to a minimum. The foam, as shown in figure 9, requires the highest pressure drop to drive the flow; this can be attributed to the rather low permeability chosen for the foam in this study. An increase in permeability to 10^{-8} m^2 would lead to a reduction of the pressure drop by approximately 2 orders of magnitude, as can be estimated from Darcy's law. The pressure drop for the interdigitated distributor is higher than for the coflow and counterflow, which is to be expected since the flow is being forcibly driven through the porous backing, in this study with a permeability of 10^{-12} m^2. The lowest pressure drops are obtained with the parallel channels, with no discernible difference in the magnitude of the pressure drop between the two.

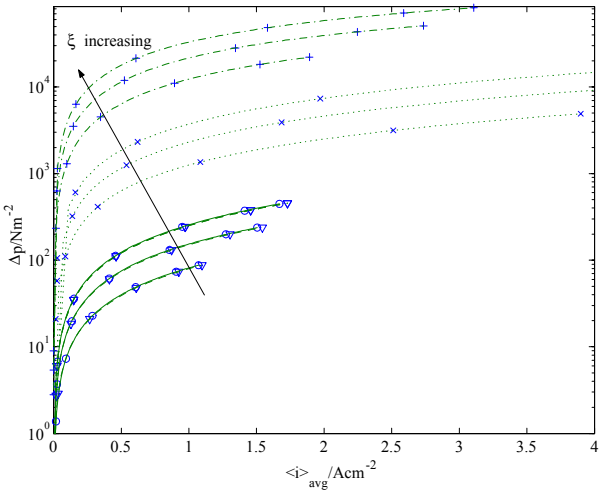

Figure 9. Pressure drop, Δp, for the different flow distributors at stoichiometry $\xi = 1.5$, 3, 5: coflow channels (o), counterflow channels (∇), interdigitated channels (x), foam (+).

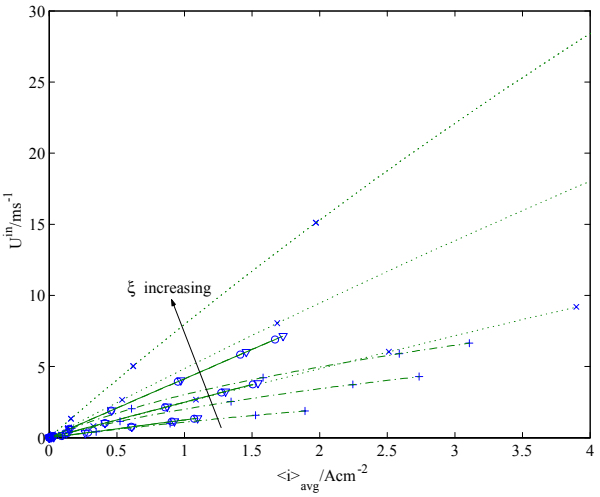

Figure 10. Obtained inlet velocity, U^{in}, for the different flow distributors at stoichiometry $\xi = 1.5$, 3, 5: coflow channels (o), counterflow channels (∇), interdigitated channels (x), foam (+).

Since we do not specify the inlet velocity, but rather iterate on it to obtain a given stoichiometry for a specified cell potential, it is of interest to see how the inlet velocity changes with current density and stoichiometry; this is shown in figure 10. The inlet velocity is almost proportional to the average current density, and only starts to deviate from linear when the density at the inlet changes due to the pressure drop obtained. The reason why the inlet velocities for the interdigitated channels are higher is because the inlet area is half as large as for the other flow distributors.

5. Conclusions

A study of different flow distributors, based on a gas-phase model for mass, momentum and species transport in the cathode of a PEM fuel cell, has been considered. Special attention was given to the treatment of the active layer, for which an agglomerate model developed previously [**3**] was used. The numerical code used was verified with an analytical solution also developed previously [**11**]. The novel features of this study are: 1) a direct quantitative comparison of the performance of different flow distributors; 2) the use of a new Tafel law which agrees well with experimental observations for a small fuel cell [**4**]. The complete validation of the gas-phase model considered here would require more detailed information about the local current density distribution; in future, this will be obtainable via experiments with a segmented cell.

The aim of the study was to compare the performance of different flow distributors for a given cell at a given potential, in terms of four different quantities: the obtained average current density, power density, standard deviation of the current density distribution and pressure drop. The results show that the interdigitated flow distributor can sustain the highest current densities, but at a higher pressure drop than the counterflow and coflow channels. Furthermore, to function properly, the interdigitated channels would have to be in contact with the porous backing in such a way that channeling effects are kept at a minimum; given the high velocities required, even the slightest gap might lead to most of the flow going through the gap and not through the porous backing, with a resulting loss of power density. A foam distributor is able to give the lowest standard deviation for the current at high current densities, but care should be taken as to its permeability to avoid an unreasonably high pressure drop.

The present work was limited to gas-phase flow and isothermal conditions. Future work will seek to incorporate both the possible production of liquid water at the catalytic layer and non-isothermal effects.

Acknowledgements

Financial support from the Swedish Foundation for Strategic Environmental Research, MISTRA, and from the Swedish National Energy Administration is gratefully acknowledged. The work was done within the framework of the Jungner Center.

Bibliography

[1] C. K. Dyer, *J. Power Sources, Proceedings of the Seventh Grove Fuel Cell Symposium*, **106**, 31 (2002).

[2] J. M. Moore, J. B. Lakeman and G. O. Mepsted, *J. Power Sources, Proceedings of the Seventh Grove Fuel Cell Symposium*, **106**, 16 (2002).

[3] F. Jaouen, G. Lindbergh and G. Sundholm, *J. Electrochem. Soc.*, **149**, A437 (2002).

[4] J. Ihonen, F. Jaouen, G. Lindbergh, A. Lundblad and G. Sundholm, *J. Electrochem. Soc.*, **149**, A448 (2002).

[5] S. Dutta, S. Shimpalee and J. W. van Zee, *J. Appl. Electrochem.*, **30**, 135 (2000).

[6] S. Dutta, S. Shimpalee and J. W. van Zee, *Int. J. Heat and Mass Transfer*, **44**, 2029 (2001).

[7] S. Shimpalee and S. Dutta, *Numerical Heat Transfer*, **38**, Part A, 111 (2000).

[8] P. Costamagna, Chem. Eng. Science, **56**, 323 (2001).

[9] T. Berning, D. M. Lu and N. Djilali, *J. Power Sources*, **106**, 284 (2002).

[10] CFX-4.4, http://www.cfx.aeat.com.

[11] M. Vynnycky and E. Birgersson, *accepted for publication in SIAM J. Applied Mathematics.*

[12] J. R. Welty, C. E. Wicks and R. E. Wilson, *Fundamentals of Momentum, Heat, and Mass Transfer*, 3rd edition, John Wiley & Sons, USA (1984).

[13] J.S.Yi and T. Van Nguyen, *J. Electrochem. Soc.*, **146**, 1 (1999).

[14] A. Kazim, H.T. Liu and P. Forges, *J. Appl. Electrochem.*, **29**, 1409 (1999) .

[15] R. Taylor and R. Krishna, *Multicomponent Mass Transfer*, John Wiley & Sons, USA (1993).

[16] M. J. Moran and H. N. Shapiro, *Fundamentals of Engineering Thermodynamics*, 2nd edition, John Wiley & Sons, USA (1993).

List of symbols

A	Area, m^2
$\mathcal{A}$	Integration constant for asymptotic solution
$\mathcal{A}i_0$	Volumetric exchange current density, $\mathrm{A\ m}^{-3}$
$\mathbf{B}$	Transformation tensor
$\mathcal{B}$	Integration constant for asymptotic solution
c	Molar concentration, $\mathrm{mol\ m}^{-3}$
$\mathbf{D}$	Diffusion tensor, $\mathrm{m}^2\mathrm{s}^{-1}$
$\widetilde{D}_{\mathrm{ij}}$	Diffusion coefficients for molar diffusive flux relative to a molar-averaged velocity, $\mathrm{m}^2\mathrm{s}^{-1}$
D_{ij}	Diffusion coefficients for mass diffusive flux relative to a mass-averaged velocity, $\mathrm{m}^2\mathrm{s}^{-1}$
$\mathcal{D}_{\mathrm{ij}}$	Binary Maxwell-Stefan diffusion coefficients, $\mathrm{m}^2\mathrm{s}^{-1}$
$\mathfrak{D}$	Effective oxygen permeability in the agglomerates, $\mathrm{mol\ m}^{-1}\mathrm{s}^{-1}$
Δp	Pressure drop, Nm^{-2}
$\mathbf{e}_{\mathrm{x}}$, $\mathbf{e}_{\mathrm{y}}$, $\mathbf{e}_{\mathrm{z}}$	Coordinate vectors
E	Potential, V
F	Faraday's constant, $\mathrm{As\ mol}^{-1}$
$\mathfrak{F}$	Nucleus effectiveness factor for the agglomerate model
h	Height, m
$\mathfrak{h}$	Relative humidity
i	Current density, $\mathrm{A\ m}^{-2}$
$\langle i_{\mathrm{v}} \rangle$	Volume current density, $\mathrm{A\ m}^{-3}$
$\mathcal{I}$	Dimensionless current density
$\mathbf{K}$	Permeability tensor, m^2
L	Length, m
M	Mean molecular mass, $\mathrm{kg\ mol}^{-1}$
$\mathcal{M}$	Dimensionless mean molecular mass
M_{i}	Molecular mass of species i, $\mathrm{kg\ mol}^{-1}$
$\mathcal{M}_{\mathrm{i}}$	Dimensionless molecular mass of species i
n	Number of electrons consumed in the ORR per oxygen molecule
$\mathbf{n}$	Unit vector in the normal direction
$\mathbf{n}_{\mathrm{i}}$	Mass flux of species i, $\mathrm{kg\ m}^{-2}\mathrm{s}^{-1}$
p	Pressure, Nm^{-2}
P	Power density, Wm^{-2}
r	Radius of agglomerate nucleus, m
R	Gas constant, $\mathrm{J\ mol}^{-1}\ \mathrm{K}^{-1}$
Re	Reynolds number
S	Denominator for transformation of diffusion coefficients, $\mathrm{m}^2\mathrm{s}^{-1}$
$\mathbf{t}$	Unit vector in the tangential direction
T	Temperature, K
$\mathbf{v}$	Velocity, ms^{-1}
$\mathcal{V}$	Volume of the representative elementary volume, m^3
w	Width, m
w_{i}	Mass fraction of species i

$\mathbf{W}$	Transformation tensor
x_{i}	Molar fraction of species i
X, Y	Dimensionless coordinates
$\mathbf{X}$	Transformation tensor
Greek	
α	Coefficient for water transport by electro-osmosis in the membrane
α_{r}	Cathodic transfer coefficient for the ORR
γ	Porosity
δ_{ij}	Kronecker delta
$\Delta = 1/(\mathrm{Re}\,\sigma^2)$	Dimensionless parameter
ζ_{i}	Dimensionless fraction of species i
η	Overpotential, V
κ	Permeability, m^2
μ	Dynamic viscosity, kg m^{-1} s^{-1}
ξ	Stoichiometry
ρ	Density, kg m^{-3}
$\sigma = h_{\mathrm{f}}/L$	Dimensionless number
σ_{std}	Standard deviation for current density, Am^{-2}
Υ	Parameter for current density expression
ϕ	General tensor
$\Phi = (2+4\alpha)\mathcal{M}_{H_2O} - \mathcal{M}_{O_2}$	Dimensionless number
$\Omega = \Lambda/\sigma$	Dimensionless number
Subscripts	
0	Equilibrium, Reference
a	Active layer
cell	Cell
p	Porous backing
pol	Polymer electrolyte in the active layer
f	Flow channel
$\mathrm{H_2O}$	Water
$\mathrm{O_2}$	Oxygen
$\mathrm{N_2}$	Nitrogen
avg	Average
Superscripts	
cat	Catalytic region
g	Gas
in	Inlet
out	Outlet
ref	Reference
vap	Vaporisation
Miscellaneous symbols	
$\langle\,\rangle$	Superficial average
$\langle\,\rangle^{(\mathrm{g})}$	Intrinsic average
$[\,]$	Scale

Appendix A. Local current density distributions

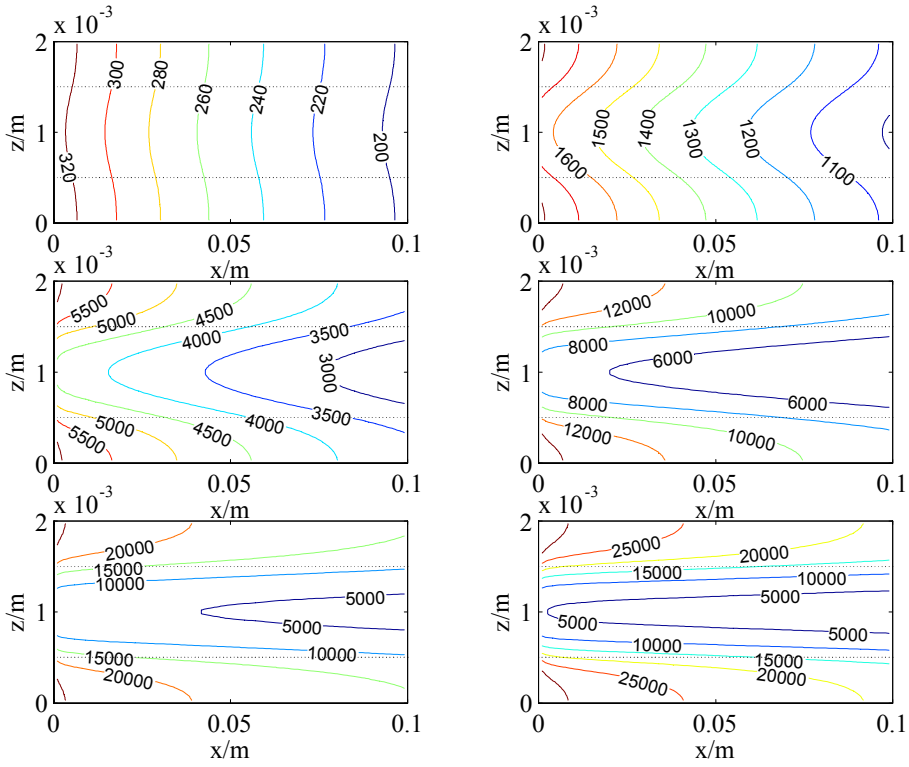

Figure A1. The local current density distribution for the coflow distributor at the active layer for different potentials at stoichiometry $\xi = 3$: a) $E_{\text{cell}} = 0.782$ V; b) $E_{\text{cell}} = 0.682$ V; c) $E_{\text{cell}} = 0.582$ V; d) $E_{\text{cell}} = 0.482$ V; e) $E_{\text{cell}} = 0.382$ V; f) $E_{\text{cell}} = 0.282$ V.

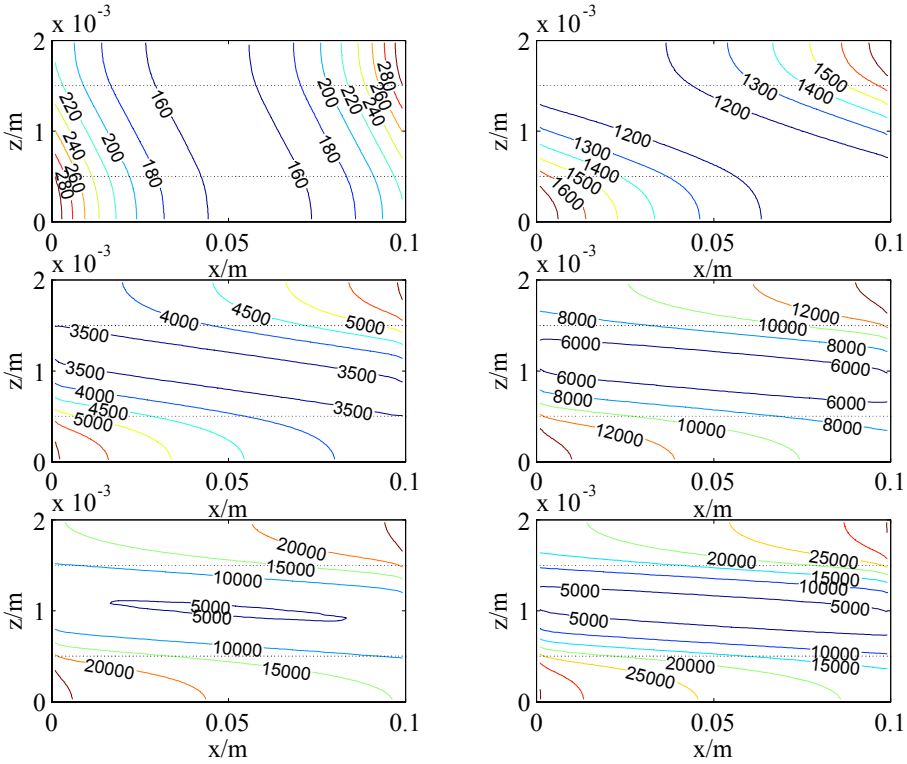

Figure A2. The local current density distribution for the counterflow distributor at the active layer for different potentials at stoichiometry $\xi = 3$: a) $E_{\text{cell}} = 0.782$ V; b) $E_{\text{cell}} = 0.682$ V; c) $E_{\text{cell}} = 0.582$ V; d) $E_{\text{cell}} = 0.482$ V; e) $E_{\text{cell}} = 0.382$ V; f) $E_{\text{cell}} = 0.282$ V.

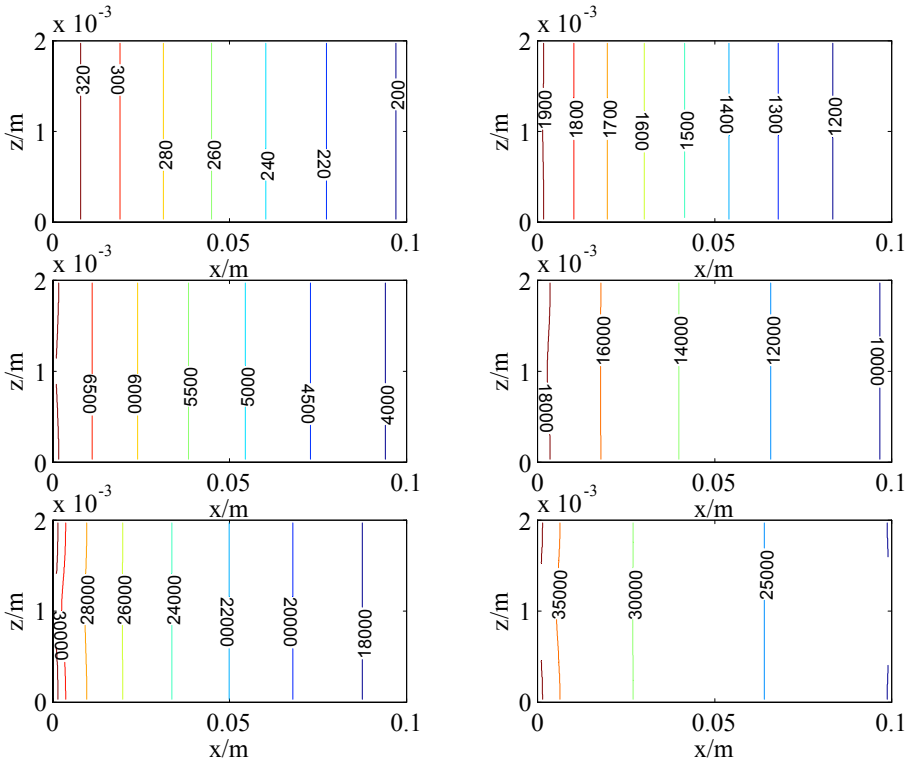

Figure A3. The local current density distribution for the foam distributor at the active layer for different potentials at stoichiometry $\xi = 3$: a) $E_{\text{cell}} = 0.782$ V; b) $E_{\text{cell}} = 0.682$ V; c) $E_{\text{cell}} = 0.582$ V; d) $E_{\text{cell}} = 0.482$ V; e) $E_{\text{cell}} = 0.382$ V; f) $E_{\text{cell}} = 0.282$ V.

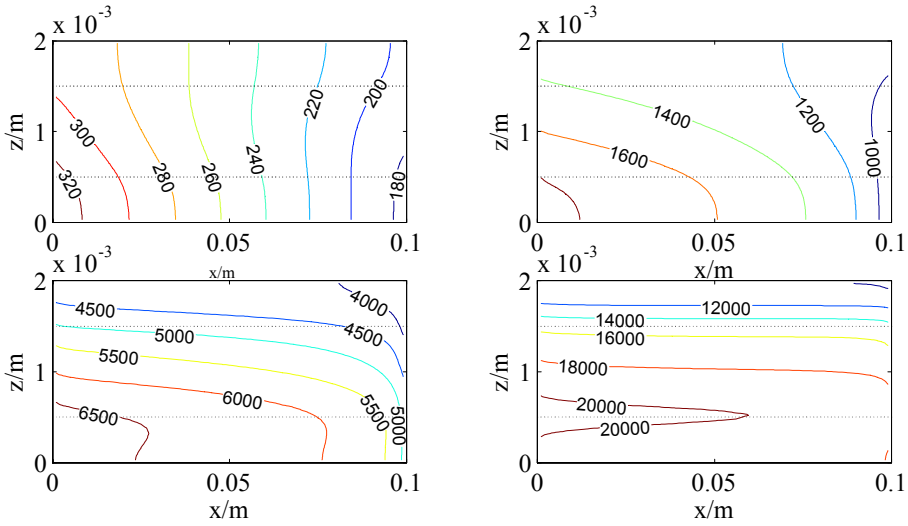

Figure A4. The local current density distribution for the interdigitated flow distributor at the active layer for different potentials at stoichiometry $\xi = 3$: a) $E_{\text{cell}} = 0.782$ V; b) $E_{\text{cell}} = 0.682$ V; c) $E_{\text{cell}} = 0.582$ V; d) $E_{\text{cell}} = 0.482$ V.

Paper 3

A Reduced Two-Dimensional One-Phase Model for Analysis of the Anode of a DMFC

E. Birgersson[a], J. Nordlund[b], H. Ekström[b], M. Vynnycky[a] and G. Lindbergh[b]

[a]Department of Mechanics, FaxénLaboratoriet, The Royal Institute of Technology, SE-100 44, Stockholm, Sweden

[b]Department of Chemical Engineering and Technology, Applied Electrochemistry, The Royal Institute of Technology, SE-100 44 Stockholm, Sweden

Abstract. An isothermal 2-D liquid-phase model for the electrokinetics and the transport of mass, momentum and species in the anode of a DMFC is presented and analysed. The model is developed for the case when the geometry aspect ratio is small, and it is shown that, under realistic operating conditions, a reduced model, which nonetheless still describes all the essential physics of the full model, can be derived. The significant benefits of this approach are that physical trends become much more apparent than in the full model, and the considerable reduction in the time required to compute numerical solutions - a fact especially useful for wide-ranging parameter studies. Such a study is then performed in terms of the three nondimensional parameters that emerge from the analysis, and we subsequently interpret our results in terms of the dimensional design and operating parameters. In particular, we highlight the effect of these on methanol mass transfer in the flow channel and on the current density. The results indicate the relative importance of mass transfer resistance in both the flow channel and the adjacent porous backing.

1. Introduction

The direct methanol fuel cell (DMFC) is an attractive power source for low power applications. High power and energy density, low emissions, operation at or near ambient conditions, fast and convenient refuelling and a potentially renewable fuel source are some of the features that make the fuel cell promising. The main advantage of the DMFC, compared to other types of fuel cells, is the simplicity of the entire power system: there is no need to store a gas or to reform a liquid fuel at elevated temperatures, with the liquid fuel simply being pumped through the anode of the fuel cell. The anode side of a DMFC can schematically be described as in Figure 1: methanol and water enter at the left-hand side and react at the active layer to form carbon dioxide, protons and electrons, according to

$$CH_3OH + H_2O \rightarrow CO_2 + 6H^+ + 6e^-. \tag{1.1}$$

An important tool for acquiring knowledge about the physical processes that occur in the anode is theoretical modeling, since it is difficult to measure potential and concentration gradients within the thin active layer or the porous backing directly. There are already some models of the DMFC that aim to

describe the processes occurring, including the electrochemistry [**1-14**]. The treatment of the mass transfer varies considerably in these models, and only a few of these models account for the mass transfer limitation on performance in both the porous backing and the active layer [**4-8,11-14**]. None of the previous models, with the exception of [**12-14**], are two-dimensional with respect to the length of the electrode, nor do they take mass transfer in the channel into account. The Kulikovsky model [**12, 13**] is a gas-phase model that neglects the influence of the spanwise gradients in the channel. Most recently, Wang and Wang [**14**] have modelled the DMFC using a multiphase mixture theory developed in earlier work for other physical applications [**15**].

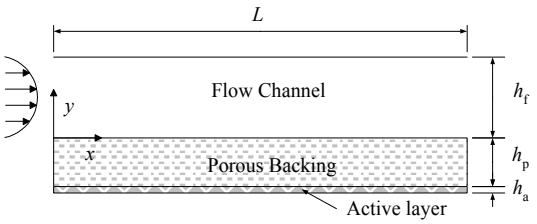

Figure 1. A schematic of the anode side of a DMFC.

Mass transfer has been shown experimentally to be important [**11**], and it is the aim of this paper to investigate this in detail by means of a two-dimensional liquid-phase model that accounts for the mass transfer in the whole anode. The influence of fuel flow on cell performance will also be analysed in a parameter study. In addition to mass transfer, the model will include all of the important known physics in the liquid-phase anode, including the porous backing and the porous active layer; however, the approach that we adopt, as distinct from all earlier work, is to use scaling arguments and elementary asymptotic techniques to yield a reduced model which requires minimal computing time, a factor which makes the model suitable for inclusion in system studies, where computational time is of the essence.

Although the one-phase mass transfer described in this paper is geared towards the direct methanol fuel cell application, the equations are general and could equally well describe the mass transfer in a one-phase fuel cell-based electrochemical reactor. It is the view of the authors that electrochemical synthesis will benefit from the development in the polymer electrolyte fuel cell area, including DMFC. Thus, the formulation presented may become of interest for applications other than the DMFC.

The mathematical model is a modified version of the reduced PEFC model derived by [**16**]. After a brief detour through the basics of flow in porous media, dimensionless quantities are introduced, followed by the governing equations and corresponding boundary conditions. We consider laminar one-phase flow in the anode, governed by the Navier Stokes equations in the channel and Darcy's law in the porous backing, coupled with multicomponent mass transfer equations for methanol and carbon dioxide. The flow can be treated as a dilute

mixture. In a previous paper [**11**], the pore diffusion, finite ionic conductivity and the complex methanol oxidation kinetics of the anode electrode were all taken into account. In the present paper, we use that model to derive an expression that can be used to reduce the governing equations in the active layer to a boundary condition for the flow in the rest of geometry; as a consequence, the present model implicitly accounts for the porous effects and the reaction kinetics of the previous study. The modeled electrode is 23 μm thick and is comprised of 0.8 mg/cm^2 of PtRu (1:1, 40% on carbon) and 1.7 mg/cm^2 of Nafion®. The model, as all previous DMFC models [**1-14**], is isothermal. For very low fuel flow rates, this is not a particularly good assumption, although it becomes so if the cell is tempered. Since the kinetic equations used were derived at 70°C, all physical properties are also taken at that temperature. Adaption of the reduced model to the anode shows the conditions for which the the velocity field in the channel decouples from the rest of the flow and can be solved *a priori*. The operating conditions at the anode enable a reduction of the mass transfer equations to just one scalar transport equation for methanol in the flow channel; the solutions in the active layer and porous backing are then given by elementary analytical expressions involving a function that requires the numerical solution of a simple transcendental equation. The reduced model, solved numerically with a Modified Box discretization scheme, is verified against two commercial codes which solve for the full set of governing equations and boundary conditions. The results from a parameter study of the anode are discussed and conclusions are drawn.

2. Mathematical formulation

A reduced model for tricomponent flow in the slender cathode of a polymer electrolyte fuel cell (PEFC) has been derived recently by [**16**]. This reduced model is based on a rigorous mathematical reduction of the full elliptic governing equations for two-dimensional one-phase conservation of mass, species and momentum in the flow channel and adjacent porous backing. Furthermore, that model is general enough to be adaptable, after minor modifications, to the anode of the DMFC. To limit the algebra, however, we will here give only the modified equations as they pertain to the anode once the slenderness of the geometry has been invoked, and refer to [**16**] for the full derivation of these. The dimensional equations are shown in Appendix A, together with the dimensional boundary conditions in Appendix B.

In the channel, see Figure 1, conservation of momentum is given by the Navier Stokes equation for an incompressible fluid and in the porous backing by Darcy's law. Continuity of mass and species transport equations are solved for the liquid mixture, containing methanol, water and carbon dioxide.

These are nondimensionalised with the parameters given below. Recognizing the slenderness of the geometry, i.e. that the ratio of the heights of the flow channel, porous backing and active layer to the length is much smaller than one, $h_{\mathrm{f}}/L << 1$, $h_{\mathrm{p}}/L << 1$, $h_{\mathrm{a}}/L << 1$, we rescale once more to obtain

what is called the narrow-gap approximation. Mathematically, this additional scaling essentially entails the reduction of elliptic PDEs to parabolic PDEs in the flow channel and ODEs in the porous backing. The resulting equations are outlined below.

2.1. Basics of flow in porous media. A proper description of the transport processes in a porous medium requires the introduction of volume-averaged equations and associated intrinsic and superficial properties, and we introduce these details first; see e.g. [**17-19**] for more details on volume averaging.

We let $\langle\phi\rangle$ and $\langle\phi\rangle^{(\mathrm{l})}$ denote superficial and intrinsic properties, defined as

$$\langle\phi\rangle \equiv \frac{1}{\mathcal{V}}\int_{\mathcal{V}} \phi \mathrm{d}\mathcal{V}', \tag{2.1}$$

and

$$\langle\phi\rangle^{(\mathrm{l})} \equiv \frac{1}{\mathcal{V}^{(\mathrm{l})}}\int_{\mathcal{V}} \phi \mathrm{d}\mathcal{V}', \tag{2.2}$$

where $\mathcal{V}$ is the total volume of the **R**epresentative **E**lementary **V**olume (REV) and $\mathcal{V}^{(\mathrm{l})}$ is the volume of the void in the REV. Introducing the porosity, $\gamma = \mathcal{V}^{(\mathrm{l})}/\mathcal{V}$, the two averages are related through

$$\langle\phi\rangle = \gamma\langle\phi\rangle^{(\mathrm{l})}. \tag{2.3}$$

2.2. Dimensionless quantities. The model is based on the following nondimensionalization:

$$\widetilde{y} = \frac{y}{L},\ \widetilde{x} = \frac{x}{L},\ \widetilde{p} = \frac{p - p^{\mathrm{out}}}{\rho\left(U^{\mathrm{in}}\right)^2},\ \langle\widetilde{p}\rangle^{(\mathrm{l})} = \frac{\langle p\rangle^{(\mathrm{l})} - p^{\mathrm{out}}}{\rho\left(U^{\mathrm{in}}\right)^2},\ \mathcal{M}_{\mathrm{i}} = \frac{M_{\mathrm{i}}}{[M]},$$
$$\langle\mathcal{I}\rangle = \frac{\langle i\rangle}{[i]},\ \widetilde{\mathbf{D}} = \frac{\mathbf{D}}{[D]},\ \left\langle\widetilde{\mathbf{D}}\right\rangle^{(\mathrm{l})} = \frac{\langle\mathbf{D}\rangle^{(\mathrm{l})}}{[D]},\ \widetilde{\mathbf{v}} = \frac{\mathbf{v}}{U^{\mathrm{in}}},\ \langle\widetilde{\mathbf{v}}\rangle = \frac{\langle\mathbf{v}\rangle}{U^{\mathrm{in}}}.$$

Here, p is the pressure (with p^{out} as the outlet pressure), M_{i} is the molecular mass of species i with typical scale $[M]$, $\mathbf{D}$ and $\langle\mathbf{D}\rangle^{(\mathrm{l})}$ are the diffusion tensors in the channel and porous backing with characteristic scale $[D]$, i is the current density with scale $[i]$, L is the length of the channel, U^{in} is the maximum velocity for a fully developed laminar velocity profile at the inlet, $\mathbf{v} = (u, v)$ is the velocity in the channel, $\langle\mathbf{v}\rangle = (\langle u\rangle, \langle v\rangle)$ is the superficial velocity in the porous backing. In what follows we will take the density to be constant and equal to that of water; this is justified on physical grounds at the start of the subsection on "Constitutive relations". The dimensionless parameters which appear are

$$\mathrm{Re} \equiv \frac{\rho U^{\mathrm{in}} L}{\mu},\ \mathrm{Sc} \equiv \frac{\mu}{[D]\rho},\ \mathrm{Da} \equiv \frac{\kappa_{\mathrm{p}}}{L^2},\ \Lambda \equiv \frac{[i][M]}{\rho U^{\mathrm{in}} F},$$

where Re, Sc and Da are the Reynolds, Schmidt and Darcy numbers, respectively, and Λ describes the ratio of the mass flux of the electrochemical reaction to the convective mass flux, whence it can be viewed as a Damköhler number.

Here, κ_p is the permeability of the porous backing, μ is the dynamic viscosity and F is Faraday's constant.

Since the typical anode is slender, i.e. h_p/L, $h_\mathrm{f}/L << 1$, we scale further with

$$X = \widetilde{x},\ Y = \frac{\widetilde{y}}{\sigma},\ U = \widetilde{u},\ V = \frac{\widetilde{v}}{\sigma},$$

where $\sigma \equiv h_\mathrm{f}/L$ and h_p is the height of the porous backing. We will later also use the notation $\mathcal{H}$ for the ratio $h_\mathrm{p}/h_\mathrm{f}$.

We neglect terms of $\mathcal{O}(\sigma)$ or lower, although combinations of σ and other dimensionless properties are retained, and introduce the additional dimensionless numbers

$$\Delta \equiv \frac{1}{\mathrm{Re}\,\sigma^2},\ \Omega \equiv \frac{\Lambda}{\sigma},\ \Sigma \equiv \frac{\sigma^2}{\mathrm{Da}^{\frac{1}{2}}};$$

here, Δ is the reciprocal of the reduced Reynolds number and Ω is the modified Damköhler number.

2.3. Governing equations. With the simplifications outlined above, the dimensionless form of the dimensional equations given in Appendix A is, for the channel,

$$\frac{\partial U}{\partial X} + \frac{\partial V}{\partial Y} = 0, \tag{2.4}$$

$$U\frac{\partial U}{\partial X} + V\frac{\partial U}{\partial Y} = -\frac{\partial P}{\partial X} + \Delta\frac{\partial^2 U}{\partial Y^2}, \tag{2.5}$$

$$\frac{\partial P}{\partial Y} = 0, \tag{2.6}$$

$$\left(U\frac{\partial}{\partial X} + V\frac{\partial}{\partial Y}\right)\begin{pmatrix} w_\mathrm{MeOH} \\ w_{\mathrm{CO_2}} \end{pmatrix} = \frac{\Delta}{\mathrm{Sc}}\frac{\partial}{\partial Y}\left[\widetilde{\mathbf{D}}\frac{\partial}{\partial Y}\begin{pmatrix} w_\mathrm{MeOH} \\ w_{\mathrm{CO_2}} \end{pmatrix}\right], \tag{2.7}$$

where w_MeOH and $w_{\mathrm{CO_2}}$ are the mass fractions of methanol and carbon dioxide, respectively. The species transport equation, Eq. 2.7, is written in a compact form, to be read as two equations, one for methanol and the other for carbon dioxide, which are coupled through the diffusion tensor, $\widetilde{\mathbf{D}}$.

The equations to be solved in the porous backing are

$$\frac{\partial \langle U\rangle}{\partial X} + \frac{\partial \langle V\rangle}{\partial Y} = 0, \tag{2.8}$$

$$\langle U\rangle = 0, \tag{2.9}$$

$$\frac{\partial \langle P\rangle^{(\mathrm{l})}}{\partial Y} = -\Delta\Sigma^2 \langle V\rangle, \tag{2.10}$$

$$\left(\langle U\rangle\frac{\partial}{\partial X} + \langle V\rangle\frac{\partial}{\partial Y}\right)\begin{pmatrix} \langle w_\mathrm{MeOH}\rangle^{(\mathrm{l})} \\ \langle w_{\mathrm{CO_2}}\rangle^{(\mathrm{l})} \end{pmatrix} = \frac{\Delta}{\mathrm{Sc}}\frac{\partial}{\partial Y}\left[\gamma\left\langle\widetilde{\mathbf{D}}\right\rangle^{(\mathrm{l})}\frac{\partial}{\partial Y}\begin{pmatrix} \langle w_\mathrm{MeOH}\rangle^{(\mathrm{l})} \\ \langle w_{\mathrm{CO_2}}\rangle^{(\mathrm{l})} \end{pmatrix}\right]. \tag{2.11}$$

We point out that the details of the derivation of Eqs. 2.8-2.10 from Eqs. A.4 and A.5 can be found in [**16**]. Briefly, these equations require a permeability $\kappa_\mathrm{p} \lesssim 10^{-10}$ m^2, so that the shear-stress-induced velocity in the streamwise

direction at the interface between the porous backing and the flow channel is negligible, and hence can be set to zero at leading order, Eq. 2.9; typical permeabilities for the porous backing found in literature range from 10^{-11} m^2 [**14**] to 10^{-14} m^2 [**12**].

2.4. Boundary conditions. The full boundary conditions are given in Appendix B, and here we give only those that are needed for our reduced model. In particular, this means that the boundary conditions at the outlet of the channel and at the right-hand end of the porous backing are redundant, and we therefore do not include them here.

At the inlet ($X = 0$, $0 \le Y \le 1$), we specify

$$U = 4\left(Y - Y^2\right), \tag{2.12}$$

which corresponds to fully developed laminar flow, and

$$\begin{pmatrix} w_{\mathrm{MeOH}} \\ w_{\mathrm{CO_2}} \end{pmatrix} = \begin{pmatrix} w^{\mathrm{in}}_{\mathrm{MeOH}} \\ w^{\mathrm{in}}_{\mathrm{CO_2}} \end{pmatrix}. \tag{2.13}$$

At the upper wall in the channel ($0 \le X \le 1$, $Y = 1$), there is no slip and no normal flow, so that

$$U = V = 0, \tag{2.14}$$

and no componental flux, so that

$$\frac{\partial w_{\mathrm{MeOH}}}{\partial Y} = \frac{\partial w_{\mathrm{CO_2}}}{\partial Y} = 0. \tag{2.15}$$

At the left wall of the porous backing, ($X = 0$, $-\mathcal{H} \le Y \le 0$), we prescribe no normal flow and no componental flux, so that

$$\langle U \rangle = \frac{\partial \langle w_{\mathrm{MeOH}} \rangle^{(\mathrm{l})}}{\partial X} = \frac{\partial \langle w_{\mathrm{CO_2}} \rangle^{(\mathrm{l})}}{\partial X} = 0. \tag{2.16}$$

At the channel/porous backing interface ($0 \le X \le 1$, $Y = 0$), the reduced model requires continuity of streamwise and normal velocity components:

$$U = \langle U \rangle, \tag{2.17}$$

$$V = \langle V \rangle. \tag{2.18}$$

For the species, continuity of mass fractions and fluxes are prescribed

$$\begin{pmatrix} w_{\mathrm{MeOH}} \\ w_{\mathrm{CO_2}} \end{pmatrix} = \begin{pmatrix} \langle w_{\mathrm{MeOH}} \rangle^{(\mathrm{l})} \\ \langle w_{\mathrm{CO_2}} \rangle^{(\mathrm{l})} \end{pmatrix}, \tag{2.19}$$

$$\widetilde{\mathbf{D}} \frac{\partial}{\partial Y} \begin{pmatrix} w_{\mathrm{MeOH}} \\ w_{\mathrm{CO_2}} \end{pmatrix} = \gamma \left\langle \widetilde{\mathbf{D}} \right\rangle^{(\mathrm{l})} \frac{\partial}{\partial Y} \begin{pmatrix} \langle w_{\mathrm{MeOH}} \rangle^{(\mathrm{l})} \\ \langle w_{\mathrm{CO_2}} \rangle^{(\mathrm{l})} \end{pmatrix}. \tag{2.20}$$

At the interface between the porous backing and the active layer ($0 \le X \le 1$, $Y = -\mathcal{H}$), we specify

$$\langle V \rangle = -\frac{\Omega \langle \mathcal{I} \rangle \Phi}{6}, \tag{2.21}$$

$$\langle V\rangle \begin{pmatrix} \langle w_{\mathrm{MeOH}}\rangle^{(\mathrm{l})} \\ \langle w_{\mathrm{CO_2}}\rangle^{(\mathrm{l})} \end{pmatrix} - \frac{\Delta}{\mathrm{Sc}}\gamma \left\langle \widetilde{\mathbf{D}} \right\rangle^{(\mathrm{l})} \frac{\partial}{\partial Y} \begin{pmatrix} \langle w_{\mathrm{MeOH}}\rangle^{(\mathrm{l})} \\ \langle w_{\mathrm{CO_2}}\rangle^{(\mathrm{l})} \end{pmatrix} = \frac{\Omega \langle \mathcal{I}\rangle}{6} \begin{pmatrix} -\mathcal{M}_{\mathrm{MeOH}} \\ \mathcal{M}_{\mathrm{CO_2}} \end{pmatrix}, \quad (2.22)$$

where $\Phi \equiv ((1+6\alpha_{\mathrm{H_2O}})\,\mathcal{M}_{\mathrm{H_2O}} + \mathcal{M}_{\mathrm{MeOH}} - \mathcal{M}_{\mathrm{CO_2}})$; in the latter, $\alpha_{\mathrm{H_2O}}$ is the number of water molecules dragged through the membrane with each proton via electro-osmosis. The electro-osmosis of methanol is neglected as it is considerably lower than the electro-osmosis of water [**6**]. Scott *et al.* [**6**] assume that $\alpha_{\mathrm{MeOH}} \approx x_{\mathrm{MeOH}}\ \alpha_{\mathrm{H_2O}}$. For the cases considered, the highest value of the molar fraction of methanol is 0.019, whence the influence of the electro-osmosis of methanol is neglected. These boundary conditions can be derived from Faraday's law and the theory of multicomponent mixtures, and have been used in dimensional form for PEFC models by [**16, 20, 21**]. The novel feature in this paper is to combine these boundary conditions with an expression for the local superficial current density, which still takes concentration and potential gradients in the active layer into account, yet does not require a spatial resolution of the active layer in the model.

2.5. Constitutive relations. By extrapolating literature data to 70°C, the influence of methanol on the density is estimated to lower the density by 0.4% at 2 wt.% methanol in the mixture [**22**]. This contribution can safely be neglected, whence we take the density of the mixture, ρ, as that of pure water.

The diffusion tensor in the channel can be simplified to a diagonal tensor, since the system can be treated as a dilute solution, rendering the cross terms redundant, i.e

$$\mathbf{D} = \begin{bmatrix} D_{\mathrm{MeOH,H_2O}} & 0 \\ 0 & D_{\mathrm{CO_2,H_2O}} \end{bmatrix}; \quad (2.23)$$

in the porous backing, a Bruggeman relationship for the superficial total mass diffusion tensor, in the form

$$\langle \mathbf{D}\rangle = \gamma^{\frac{3}{2}}\mathbf{D}, \quad (2.24)$$

will be used. Note that we specify the superficial diffusion tensor here and not the intrinsic.

In order to take the porous effects of the actual active layer into account, a previous model [**11**] is used to generate an expression for the local current density, that can be used for the boundary conditions at the active layer/porous backing. This current density implicitly accounts for the same effects as were considered in that paper, i.e. pore diffusion in the active layer, finite ionic conductivity and the complex methanol oxidation kinetics. Appendix C outlines how the model in the previous paper is reduced, in dimensional form, to

$$\langle i\rangle = A\left(\langle c_{\mathrm{MeOH}}\rangle^{(\mathrm{l})}\right)^{B} \frac{\exp\left(\frac{\alpha_{\mathrm{A}}F}{RT}\left(E_{\mathrm{A}}-E_0\right)\right)}{1+\exp\left(\frac{\alpha_{\mathrm{A}}F}{RT}\left(E_{\mathrm{A}}-E_0\right)\right)}, \quad (2.25)$$

where $\langle i\rangle$ is the local superficial current density, E_{A} is the anode potential measured at the active layer/membrane interface versus a DHE reference electrode

($E_{\mathrm{A}} = 0.33 - 0.40$ V [**11**]), α_{A} is the Tafel slope measured at low potentials, $\langle c_{\mathrm{MeOH}} \rangle^{(\mathrm{l})} = \langle \rho \rangle^{(\mathrm{l})} \langle w_{\mathrm{MeOH}} \rangle^{(\mathrm{l})} / M_{\mathrm{MeOH}}$ is the methanol concentration at the porous backing/active layer interface, and A, B and E_0 are three experimentally fitted parameters (see Table I).

The vapor pressure of the dissolved carbon dioxide is taken from Henry's law for molar fractions, assuming that the low fraction of methanol in the liquid water does not influence the Henry's law coefficient, $H_{\mathrm{CO_2}}$:

$$p_{\mathrm{CO_2}} = x_{\mathrm{CO_2}} H_{\mathrm{CO_2}}. \tag{2.26}$$

2.6. Magnitude of dimensionless numbers. To determine the magnitude of the dimensionless numbers, we need typical scales for the anode, which are given by $[M] \sim 10^{-2}$ kg mol^{-1}, $[i] \sim 4 \times 10^3$ Am^{-2} and $[D] \sim 10^{-9}$ m^{2}s^{-1}; the remaining parameters are summarized in Table I.

Table I. Base-case parameters.

Parameter	Value	Units
A	1.57×10^2	[-]
α_{A}	7.9×10^{-1}	[-]
$\alpha_{\mathrm{H_2O}}$	2.5, see Ref. [**3**]	[-]
α_{MeOH}	$\alpha_{\mathrm{MeOH}} \approx x_{\mathrm{MeOH}}\ \alpha_{\mathrm{H_2O}}$ [**6**]	[-]
B	6.10×10^{-1}	[-]
$D_{\mathrm{MeOH,H_2O}}$	6.69×10^{-9}	m^{2}s^{-1}
E_0	5.04×10^{-1}	V
E_{A}	0.5	V
F	96487	As mol^{-1}
γ	8.75×10^{-1}	[-]
h_{a}	2.3×10^{-5}, see Ref. [**11**]	m
h_{f}	10^{-3}	m
h_{p}	1.8×10^{-4}	m
$H_{\mathrm{CO_2}}$	3903, see Ref. [**23**]	bar
κ_{p}	10^{-12}	m^2
L	1×10^{-1}	m
$M_{\mathrm{CO_2}}$	4.4×10^{-2}	kg mol^{-1}
$M_{\mathrm{H_2O}}$	1.8×10^{-2}	kg mol^{-1}
M_{MeOH}	3.2×10^{-2}	kg mol^{-1}
μ	4.1×10^{-4}	kgm^{-1}s^{-1}
p^{out}	101.325×10^3	Pa
R	8.314	Jmol^{-1}K^{-1}
ρ	978	kg m^{-3}
T	343	K
U^{in}	$\frac{3}{2} \times 3 \times 10^{-3}$	ms^{-1}
$w^{\mathrm{in}}_{\mathrm{CO_2}}$	0	[-]
$w^{\mathrm{in}}_{\mathrm{MeOH}}$	3.2×10^{-2}	[-]

The dimensionless numbers are thence Re $\sim 10^3$, Sc ~ 50, Da $\sim 10^{-10}$, $\Lambda \sim 4 \times 10^{-4}$, $\sigma \sim 10^{-2}$, $\Omega \sim 4 \times 10^{-2}$, $\Delta \sim 10$ and $\Sigma \sim 10$. Noting the orders of magnitude of these various parameters enables us to simplify the model equations further, as follows.

2.7. Adaption to the anode of a DMFC. We note that $w_{\mathrm{H_2O}} >> w_{\mathrm{MeOH}}$ and $w_{\mathrm{H_2O}} >> w_{\mathrm{CO_2}}$, so writing

$$w_{\mathrm{MeOH}} + w_{\mathrm{CO_2}} = 1 - w^{\mathrm{in}}_{\mathrm{H_2O}}, \tag{2.27}$$

we only need to solve the mass transfer equation for methanol and this relationship will provide the mass fraction of carbon dioxide. This also simplifies the diffusion coefficient $D_{\mathrm{MeOH,H_2O}}$, which we can treat as constant for the dilute system; thus, an appropriate choice for the characteristic diffusion coefficient scale, $[D]$, is $[D] = D_{\mathrm{MeOH,H_2O}}$.

Returning to the porous backing and the velocity boundary condition, Eq. 2.21, we scale the spanwise velocity in the porous backing further according to

$$\left\langle \widehat{V} \right\rangle = \frac{\langle V \rangle}{\Omega}. \tag{2.28}$$

Using Eq. 2.9 to eliminate $\langle U \rangle$ in Eqs. 2.8 and 2.11, Eqs. 2.8, 2.10 and 2.11 become, respectively,

$$\frac{\partial \left\langle \widehat{V} \right\rangle}{\partial Y} = 0, \tag{2.29}$$

$$\frac{\partial \langle P \rangle^{(\mathrm{l})}}{\partial Y} = -\Delta \Sigma^2 \Omega \left\langle \widehat{V} \right\rangle, \tag{2.30}$$

$$\Omega \left\langle \widehat{V} \right\rangle \frac{\partial \langle w_{\mathrm{MeOH}} \rangle^{(\mathrm{l})}}{\partial Y} = \frac{\Delta}{\mathrm{Sc}} \gamma^{\frac{3}{2}} \frac{\partial^2 \langle w_{\mathrm{MeOH}} \rangle^{(\mathrm{l})}}{\partial Y^2}. \tag{2.31}$$

Now, since $\Omega \sim O\left(10^{-2}\right) \ll 1$, we conclude from Eq. 2.18 that at leading order for the channel $V = 0$ at $Y = 0$; furthermore, Eqs. 2.9 and 2.17 imply that $U = 0$ at $Y = 0$. Consequently, we find that the inlet condition for a fully developed laminar velocity profile satisfies the momentum equation downstream, and thence that, at leading order, the velocity decouples from the mass transfer in the channel; all that remains to be solved there is

$$4\left(Y - Y^2\right) \frac{\partial w_{\mathrm{MeOH}}}{\partial X} = \frac{\Delta}{\mathrm{Sc}} \frac{\partial^2 w_{\mathrm{MeOH}}}{\partial Y^2}. \tag{2.32}$$

Now, Eqs. 2.21 and 2.29 combine to give, for the entire porous backing,

$$\left\langle \widehat{V} \right\rangle = -\frac{\langle \mathcal{I} \rangle \, \Phi}{6};$$

then, since the current density is a function of X alone, we have $\left\langle \widehat{V} \right\rangle = \left\langle \widehat{V}(X) \right\rangle$. We can integrate Eq. 2.31 and, using Eq. 2.21 and 2.22, we arrive at

$$-\frac{\Omega \langle \mathcal{I} \rangle \Phi}{6} \langle w_{\mathrm{MeOH}} \rangle^{(\mathrm{l})} - \frac{\Delta}{\mathrm{Sc}} \gamma^{\frac{3}{2}} \frac{\partial \langle w_{\mathrm{MeOH}} \rangle^{(\mathrm{l})}}{\partial Y} = -\frac{\Omega \langle \mathcal{I} \rangle}{6} \mathcal{M}_{\mathrm{MeOH}}. \tag{2.33}$$

Furthermore, choosing $[M] = M_{\mathrm{MeOH}}$, whence $\mathcal{M}_{\mathrm{MeOH}} = 1$, Eq. 2.33 becomes

$$\Phi \langle w_{\mathrm{MeOH}} \rangle^{(\mathrm{l})} + \frac{6\Delta}{\mathrm{Sc}\Omega \langle \mathcal{I} \rangle} \gamma^{\frac{3}{2}} \frac{\partial \langle w_{\mathrm{MeOH}} \rangle^{(\mathrm{l})}}{\partial Y} = 1. \tag{2.34}$$

Returning to the expression for the current density, Eq. 2.25, and choosing the, as yet, unspecified current density scale, $[i]$, to be

$$[i] = A \left(\frac{\rho w^{\mathrm{in}}_{\mathrm{MeOH}}}{M_{\mathrm{MeOH}}} \right)^{B} \frac{\exp\left(\frac{\alpha_{\mathrm{A}} F}{RT} (E_{\mathrm{A}} - E_0) \right)}{1 + \exp\left(\frac{\alpha_{\mathrm{A}} F}{RT} (E_{\mathrm{A}} - E_0) \right)}, \tag{2.35}$$

we obtain

$$\langle \mathcal{I} \rangle = \left(\langle w_{\mathrm{MeOH}} \rangle^{(\mathrm{l})} (X, -\mathcal{H}) / w^{\mathrm{in}}_{\mathrm{MeOH}} \right)^{B}. \tag{2.36}$$

Integrating Eq. 2.34 gives

$$\langle w_{\mathrm{MeOH}} \rangle^{(\mathrm{l})} (X, Y) = \frac{1}{\Phi} + \mathfrak{C} \exp\left(-\frac{\Phi \mathrm{Sc}\Omega \langle \mathcal{I} \rangle}{6\Delta \gamma^{\frac{3}{2}}} Y \right), \tag{2.37}$$

where $\mathfrak{C}$ is an integration constant to be determined shortly. At $Y = -\mathcal{H}$, we have

$$\langle w_{\mathrm{MeOH}} \rangle^{(\mathrm{l})} (X, -\mathcal{H}) = \frac{1}{\Phi} + \mathfrak{C} \exp\left(\frac{\Phi \mathrm{Sc}\Omega \langle \mathcal{I} \rangle}{6\Delta \gamma^{\frac{3}{2}}} \mathcal{H} \right), \tag{2.38}$$

and at $Y = 0$,

$$\langle w_{\mathrm{MeOH}} \rangle^{(\mathrm{l})} (X, 0) = \frac{1}{\Phi} + \mathfrak{C}, \tag{2.39}$$

whence the integration constant $\mathfrak{C}$ is given by the methanol mass fraction at the interface between the porous backing and the channel. Recalling the boundary conditions for the plain/porous interface, Eqs. 2.19 and 2.20, for the methanol transport equation, we combine these two to obtain just one boundary condition for the channel at $Y = 0$:

$$\frac{\partial w_{\mathrm{MeOH}}(X, 0)}{\partial Y} + \frac{\Phi \mathrm{Sc}\Omega \langle \mathcal{I} \rangle}{6\Delta} \left(w_{\mathrm{MeOH}}(X, 0) - \frac{1}{\Phi} \right) = 0. \tag{2.40}$$

This is valid for any profile $\langle \mathcal{I} \rangle$, which is a function of the value of $\langle w_{\mathrm{MeOH}} \rangle^{(\mathrm{l})}$ at $Y = -\mathcal{H}$; for the profile considered in this paper, $\langle \mathcal{I} \rangle$ can be determined in terms of $w_{\mathrm{MeOH}}(X, 0)$ through the transcendental equation

$$w^{\mathrm{in}}_{\mathrm{MeOH}} \langle \mathcal{I} \rangle^{\frac{1}{B}} = \frac{1}{\Phi} + \left(w_{\mathrm{MeOH}}(X, 0) - \frac{1}{\Phi} \right) \exp\left(\frac{\Gamma \langle \mathcal{I} \rangle}{6} \right), \tag{2.41}$$

where $\Gamma = \Phi \mathrm{Sc}\Omega\mathcal{H}/(\Delta \gamma^{\frac{3}{2}})$.

In summary, the adaption of the reduced model to the anode of a DMFC is based on the fact that the anode operates at a large water fraction and that

the magnitude of the dimensionless parameter Ω is much smaller than 1; in dimensionless form, the latter condition is

$$\frac{[i]\,[M]\,L}{\rho U^{\mathrm{in}} F h_{\mathrm{f}}} \ll 1.$$

Mathematically, we find that these reductions enable us to obtain solutions for the porous backing in simple analytical form; for the channel, we have an analytical solution for the velocity field and a linear diffusion equation for the methanol concentration, although subject to a highly non-linear boundary condition at the interface with the porous backing.

3. Numerics and verification

We have to resort to a numerical scheme to solve the transport equation for methanol in the channel, since no further simplifications are possible. This entails solving Eq. 2.32, subject to the boundary conditions Eqs. 2.15 and 2.40 and the inlet condition for methanol, Eq. 2.13.

The governing equations are parabolic, for which a Modified Box discretization scheme is suitable [**24**]. The scheme leads to a block tridiagonal matrix, allowing fast computations. The resulting system of non-linear equations is solved with a Newton-Raphson-based algorithm in MATLAB 6.

To confirm the validity of the reduced model, its predictions were compared with numerical results obtained using two other softwares, wherein the full elliptic governing equations and boundary conditions are implemented. One is FEMLAB 2.2 (see [**25**] for details), a commercial finite element solver for a wide variety of engineering applications; the other is CFX-4.4 (see [**26**] for details), a commercial CFD software which uses finite volumes. Comparison, shown in Figure 2, was carried out in terms of the local superficial current density obtained along the anode for a variety of values for the nondimensional parameters Δ and Ω (given in Table II).

Table II. Values of Δ and Ω used for the verification.

Δ	0.932	2.79	9.32	27.9	93.2	279
Ω	3.76×10^{-3}	1.13×10^{-2}	3.76×10^{-2}	1.13×10^{-1}	3.76×10^{-1}	1.13

These were obtained by varying the inlet velocity, U^{in}, and keeping all other physical parameters constant; in particular, the base case corresponds to $\Delta = 9.32$ and $\Omega = 3.76 \times 10^{-2}$. Several features are apparent. First, for the higher (Δ, Ω)-combinations, the reduced model starts to deviate from the full solution, since the spanwise velocity due to the electrochemical reaction now is of the same order of magnitude as the streamwise inlet velocity, i.e. Ω is no longer much smaller than unity and the spanwise velocity in the channel is no longer negligible. Nevertheless, the local current densities from the reduced model remain close to the current densities from the full elliptic equations, even for these combinations. Second, we note discrepancies between the values obtained

at the inlet and outlet by the two commercial solvers. In particular, convergence difficulties were encountered with FEMLAB 2.2 as regards the resolution of the corners, and the solutions presented are actually for a channel that is extended at the inlet and outlet; such difficulties were not encountered with CFX-4.4. Since our principal interest was only to verify the reduced model, these differences were not investigated further.

A final comment here which illustrates the benefit of the reduced model approach concerns a comparison of the computing times for the three methods. On a 1Ghz AMD PC, with 512 MB SDRAM the reduced model with 10^4 cells took $\sim$ 5 CPU seconds to converge, whereas Femlab 2.2 required $\gtrsim 1-2$ CPU minutes. The CFX-4.4 code required $\gtrsim 1-2$ CPU minutes on a 500 MHz Compaq Alphaserver with 3 GB RAM. Mesh independent solutions were found for the reduced model at $\lesssim 10^3$ cells, allowing for computational times of less than 1 second. For the present study 10^4 cells were chosen, as speed was not of the essence.

4. Results and Discussion

The nondimensionalisation of the governing equations reveals that the flow in the anode is governed essentially by three dimensionless numbers: Δ, Ω, and $\mathcal{H}$. Both Δ and Ω contain design parameters, such as the geometry of the anode in terms of length and height of the flow channel, and inlet conditions, such as velocity. $\mathcal{H}$ is the ratio of the heights of the porous backing and the flow channel. Varying Δ, Ω and $\mathcal{H}$ thus covers all possible combinations of the underlying parameters, apart from porous backing porosity and methanol inlet composition.

Figure 2 depicts the local superficial current density for different values of Δ. For lower values, which can be interpreted as higher inlet velocities or shorter channels, the current density distribution is more even than at higher ones, where the methanol content becomes more or less depleted downstream. Higher Δ-values correspond to lower inlet velocities or longer channels than given by the base case.

Given the importance of mass transfer in a DMFC anode [**11**], it is of interest to see the role of geometrical effects in a two-dimensional electrode, especially with regard to the current density distribution in the streamwise direction and the concentration gradients of methanol and carbon dioxide. A uniform current distribution is desirable, not only from the perspective of catalyst utilisation, but also since it is reasonable to assume that the degradation of the electrode with time is linked to the local current density.

In Figure 2, it is evident that the current distribution along the electrode is far from uniform, especially for the larger values of Δ; for instance, for the base case parameters, the local current density drops from 4300 Am^{-2} at the inlet to 3000 Am^{-2} at the outlet. Clearly we have mass transfer limitations along the anode. Since the local superficial current density is a function of the methanol mass fraction at the active layer/porous backing interface, a gradient in the methanol fraction is expected to be the cause.

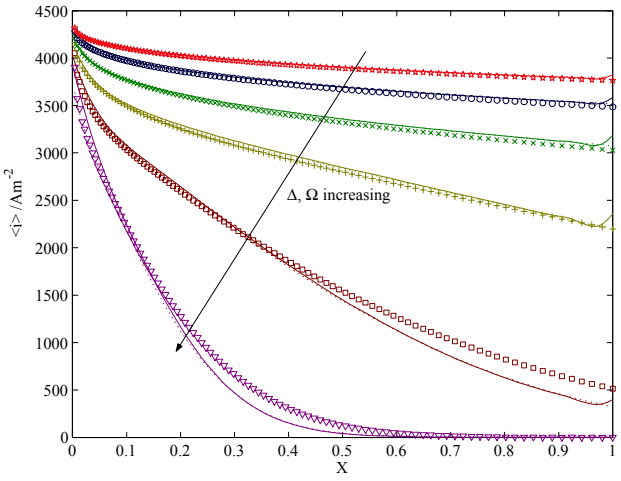

Figure 2. Verification of the reduced model. $(\cdots)$ corresponds to the CFX-4.4 solution with 10^4 number of nodes, (—) is the Femlab solution for $\sim$1000 adapted nodes and markers are for the reduced model, with 10^4 cells. ($\bigstar$): $\Delta = 0.932$, (o): $\Delta = 2.79$, ($\times$): $\Delta = 9.32$, (+): $\Delta = 27.9$, ($\square$): $\Delta = 93.2$, ($\triangledown$): $\Delta = 279$.

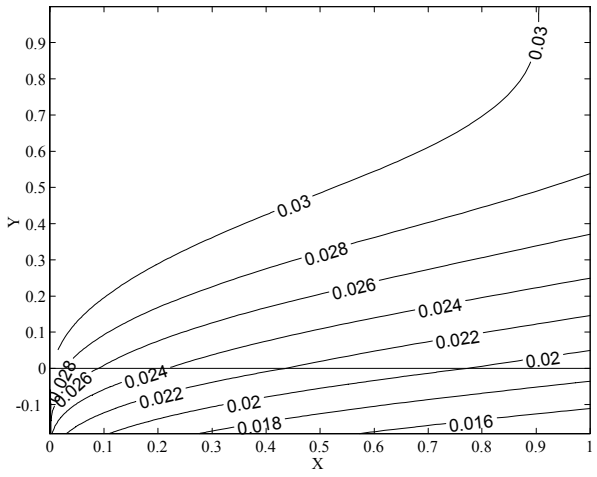

Figure 3. Methanol mass fraction for the base case ($\Delta = 9.32$).

This is indeed the case, as can be seen from Figure 3, where the methanol mass fraction for the base case is shown. From the contour lines we discern

two coupled mass transfer resistances, one in the channel and the other in the porous backing. In the channel, mass transfer is mainly via diffusion in the spanwise direction for $\Omega < 1$, see Eq. 2.32, whereas the convective contribution in the porous backing constitutes $\Phi \langle w_{\mathrm{MeOH}} \rangle^{(l)} \sim 20\%$ of the total mass flux, as given by Eq. 2.34.

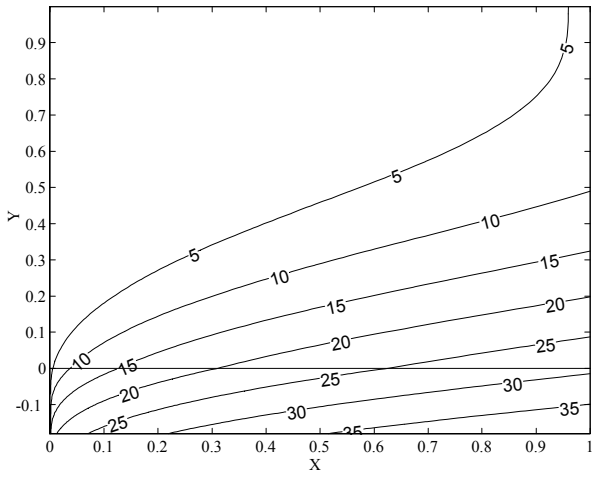

Figure 4. Partial pressure of the carbon dioxide for the base case ($\Delta = 9.32$).

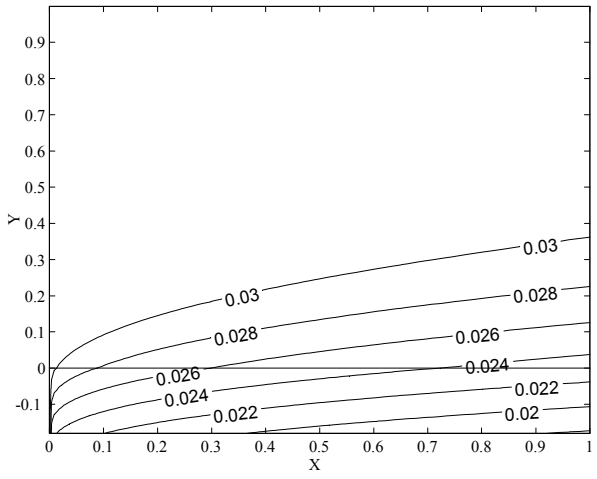

Figure 5. Methanol mass fraction for $\Delta = 2.79$.

As already noted above, the discrepancy between the results of the reduced model and the full elliptic model is due to the increasing contribution of the spanwise velocity to the mass transfer in the flow channel.

Figure 4 illustrates the theoretical partial pressures of the liquid mass fractions of carbon dioxide in the anode. The high supersaturations of 5-35 bar for the base case indicate that carbon dioxide will evolve as a gas and not remain fully dissolved in the liquid phase.

For $\Delta/\mathrm{Sc} << 1$, we expect a boundary layer to develop adjacent to the porous backing. This is indeed the case, as is illustrated in Figure 5, with contours for the methanol mass fraction for $\Delta = 2.80$, which can be viewed as the base case but with an inlet velocity of 10^{-2} ms^{-1}. As Δ is decreased, this boundary layer will decrease in thickness, leading to an enhanced mass transfer to the active layer, as is apparent from Figure 2.

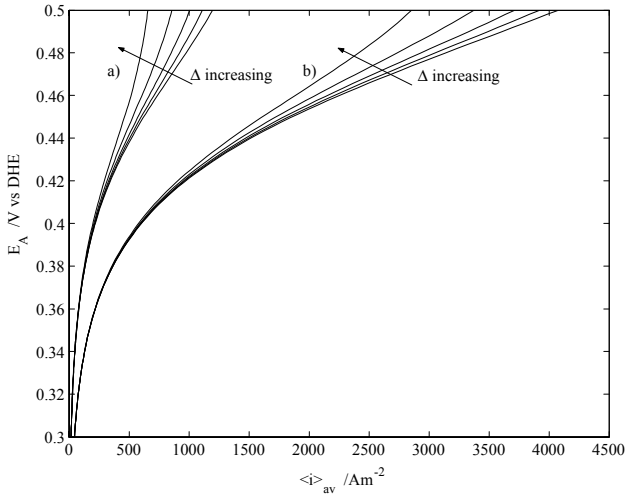

Figure 6. Polarization curves for $\Delta = 0.279$, 0.932, 2.79, 9.32 and 27.9. a) $w^{\mathrm{in}}_{\mathrm{MeOH}} = 6.4 \times 10^{-3}$ (0.2 M) and b) $w^{\mathrm{in}}_{\mathrm{MeOH}} = 3.2 \times 10^{-2}$ (1 M).

Varying Δ will also influence the polarization curves, as shown in Figure 6. The figure shows polarization curves corresponding to the inlet concentrations 0.2 M and the base case, 1 M, of methanol. The impact of varying Δ is larger for higher potentials. At a potential of 0.5 V vs DHE, the difference between high and low Δ values is significant. The influence of Δ on the polarization curve is very low at potentials below 0.4 V, i.e. anode performance at such low potentials is independent of operating conditions, such as the fluid flow rate or length of the anode. Of note here is that the impact of varying Δ needs to be considered above a certain potential rather than above a certain current density, contrary to what one might at first expect.

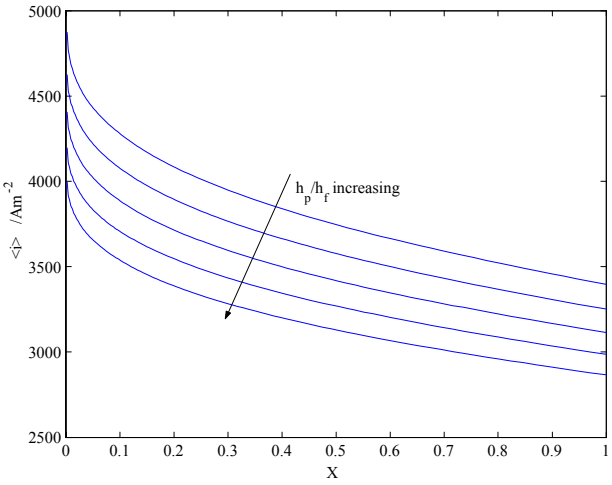

Figure 7. Local current density for different $\mathcal{H} = h_{\mathrm{p}}/h_{\mathrm{f}}$. $\mathcal{H} = 0$, $6.75{\times}10^{-2}$, $1.35{\times}10^{-1}$, $2.03{\times}10^{-1}$ and $2.70{\times}10^{-1}$. Keeping the height of the flow channel fixed at $h_{\mathrm{f}} = 10^{-3}$ m, these curves would correspond to $h_{\mathrm{p}} = 0$ m, $6.75{\times}10^{-5}$ m, $1.35{\times}10^{-4}$ m, $2.03{\times}10^{-4}$ m and $2.70{\times}10^{-4}$ m.

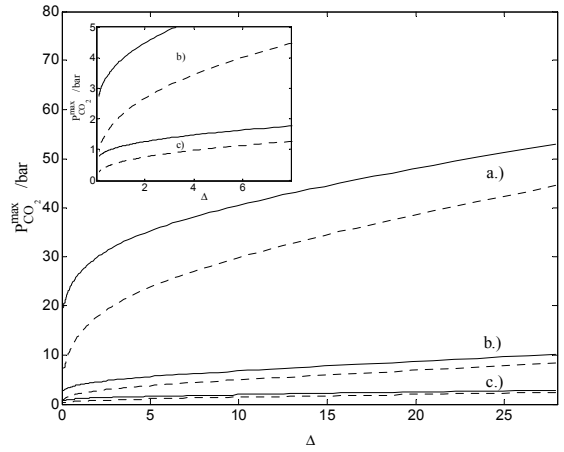

Figure 8. The maximum pressure in the porous backing (—) and the adjacent channel $(\cdots)$ for different Δ. a) $E_{\mathrm{A}} = 0.5$ V, b) $E_{\mathrm{A}} = 0.40$ V and c) $E_{\mathrm{A}} = 0.35$ V.

It is interesting to see the model prediction when the height of the porous backing or the flow channels is changed. From Figure 7, where we have kept the base case parameters and varied $\mathcal{H}$, it is clear that it would be desirable to have smaller $\mathcal{H}$ values. This corresponds to a thin porous backing and/or broad flow channels. The performance in terms of total current density at a given anode potential can potentially be improved by $\sim$10% for the base case set of parameters, by letting $\mathcal{H} \to 0$. The figure also shows that the shape of the local current density distribution is almost entirely unaffected by changing $\mathcal{H}$.

An important question arises when the carbon dioxide partial pressure is as high as in the base case: can the pressure be reduced by lowering Δ? Figure 8 gives the maximum partial pressure of carbon dioxide in the two different media, the porous backing and the flow channel. It is obvious from the figure that even for very low values of Δ, thermodynamics imply that the carbon dioxide from the electrochemical reaction will evolve as a gas, unless the potential is very low. The conditions for one-phase flow are thus satisfied only for $\Delta << 1$ in conjunction with low potentials, typically $E_{\mathrm{A}} \lesssim 0.35$ V. Previous calculations [**27**] indicate that carbon dioxide gas will form in the gas diffusion layer, or even in the porous electrode, at base-case supersaturations. Since not even very large flows of fuel (lower values of Δ) prevent the formation of carbon dioxide gas at moderate current densities, it is inevitable that a model that aims to capture the full physics in a DMFC has to take two-phase flow into account.

5. Conclusions

A one-phase model for mass, momentum and species transport in the anode of a DMFC has been considered. The governing equations and boundary conditions were nondimensionalised, and a reduced model was then derived, using elementary asymptotic techniques, for the case where the anode geometry is slender.

From the modelling point of view, an important advantage of the reduced approach is that it leads to an understanding of the important transport mechanisms for momentum, mass and species that would have been difficult to discern from simply a numerical solution of the full set of equations. In particular, we find that flow in the anode can be described by three dimensionless parameters, $\Delta, \Omega, \mathcal{H}$, given in terms of operating, design and physical parameters by

$$\Delta = \frac{\mu L}{\rho U^{\mathrm{in}} h_{\mathrm{f}}^2}, \Omega = \frac{[i]\,[M]\,L}{\rho U^{\mathrm{in}} F h_{\mathrm{f}}}, \mathcal{H} = \frac{h_{\mathrm{p}}}{h_{\mathrm{f}}}.$$

In addition, differences and similarities between different types of fuel cells become apparent. For instance, in contrast to the cathode of a PEFC, where the flow induced by the electrochemical reaction at the catalytic layer was found to have a leading order effect on the flow field in the channel [**16**], the velocity induced by the electrochemical reaction in the anode of the DMFC has a negligible effect on the channel flow field, which leads to a decoupling

of the momentum equations and furthermore allows us to write the velocity field in the channel in closed form. In addition, although the equations of the reduced model must themselves be solved numerically, the computational cost is considerably smaller than that incurred when using commercial software to solve the full set. This can be of benefit both for thorough parameter studies, as well as for system studies of DMFCs.

From the point of view of predicting fuel cell performance, a parameter study has shown that the current density distribution is far from even, especially for higher values of Δ, i.e. lower inlet velocitites or longer anodes. Performance can be improved by choosing thin porous backings (small $\mathcal{H}$) and running the cell at smaller values of Δ : the former will reduce the mass transfer limitations in the porous backing and the latter in the flow channel.

The mass fraction of the carbon dioxide in the liquid phase leads to high supersaturations, whence carbon dioxide will vaporize for all operationally realistic values of Δ and evolve as a gas. The present model does not capture this gas phase, which is expected to affect overall flow behavior in the anode, not least due to the buoyancy effect of the rising bubbles and its resulting impact on the mass transfer of liquid methanol to the active layer. The analysis of the one-phase flow presented in this paper is intended to serve as a stepping stone for a forthcoming two-phase study.

Acknowledgements

Financial support from the Swedish Foundation for Strategic Environmental Research, MISTRA, and from the Swedish National Energy Administration is gratefully acknowledged. The work was done within the framework of the Jungner Center. J. Nordlund gratefully acknowledges a scholarship from the Ernst Johnson foundation.

Appendix A. Governing equations in dimensional form

Flow channel.- The equations for the conservation of mass and momentum, given respectively by

$$\nabla \cdot \mathbf{v} = 0, \tag{A.1}$$

$$\nabla \cdot (\rho \mathbf{v} \otimes \mathbf{v}) = -\nabla p + \mu \nabla^2 \mathbf{v}, \tag{A.2}$$

are solved together with the scalar transport equations for methanol and carbon dioxide:

$$\nabla \cdot \left(\mathbf{v} \begin{pmatrix} w_{\mathrm{MeOH}} \\ w_{\mathrm{CO_2}} \end{pmatrix} \right) = \nabla \cdot \left(\mathbf{D} \begin{bmatrix} \nabla w_{\mathrm{MeOH}} \\ \nabla w_{\mathrm{CO_2}} \end{bmatrix} \right). \tag{A.3}$$

Porous backing.- Darcy's law with the Forchheimer and Brinkman extension is assumed to govern the flow in the porous backing:

$$\nabla \cdot \langle \mathbf{v} \rangle = 0, \tag{A.4}$$

$$\langle \mathbf{v} \rangle = -\frac{\kappa_{\mathrm{p}}}{\mu} \nabla \langle p \rangle^{(\mathrm{l})} + \kappa_{\mathrm{p}} \nabla^2 \left(\frac{\langle \mathbf{v} \rangle}{\gamma} \right) - \mathbf{F} \langle \mathbf{v} \rangle, \tag{A.5}$$

where $\mathbf{F}$ is the Forchheimer correction tensor. Scalar transport is given by

$$\nabla \cdot \left(\langle \mathbf{v} \rangle \begin{pmatrix} \langle w_{\mathrm{MeOH}} \rangle^{(\mathrm{l})} \\ \langle w_{\mathrm{CO_2}} \rangle^{(\mathrm{l})} \end{pmatrix} \right) = \nabla \cdot \left(\gamma \langle \mathbf{D} \rangle^{(\mathrm{l})} \begin{bmatrix} \nabla \langle w_{\mathrm{MeOH}} \rangle^{(\mathrm{l})} \\ \nabla \langle w_{\mathrm{CO_2}} \rangle^{(\mathrm{l})} \end{bmatrix} \right). \tag{A.6}$$

Appendix B. Boundary conditions in dimensional form

Inlet, outlet, upper wall, vertical walls.- For the flow channel, we specify inlet velocity and liquid composition at $x = 0$, $0 \leq y \leq h_f$:

$$u = U^{\text{in}}, \quad v = 0, \quad w_{\text{MeOH}} = w^{\text{in}}_{\text{MeOH}}, \quad w_{\text{CO}_2} = w^{\text{in}}_{\text{CO}_2}. \tag{B.1}$$

At the upper channel wall ($0 \leq x \leq L$, $y = h_f$), there is no slip, no normal flow and no componental flux:

$$u = v = \frac{\partial w_{\text{MeOH}}}{\partial y} = \frac{\partial w_{\text{CO}_2}}{\partial y} = 0. \tag{B.2}$$

At the outlet at $x = L$, $0 \leq y \leq h_f$, we set the pressure and no diffusive componental flux:

$$p = p^{\text{out}}, \quad \frac{\partial v}{\partial x} = \frac{\partial w_{\text{MeOH}}}{\partial x} = \frac{\partial w_{\text{CO}_2}}{\partial x} = 0. \tag{B.3}$$

At the vertical walls of the porous electrode ($x = 0, L$, $-h_p \leq y \leq 0$), we have no normal flow, no tangential shear and no mass flux for the species:

$$\langle u \rangle = \frac{\partial \langle v \rangle}{\partial x} = \frac{\partial \langle w_{\text{MeOH}} \rangle^{(\text{l})}}{\partial x} = \frac{\partial \langle w_{\text{CO}_2} \rangle^{(\text{l})}}{\partial x} = 0. \tag{B.4}$$

Channel/porous backing interface.- At the fluid-porous interface at $y = 0$, $0 \leq x \leq L$, we specify continuity of the superificial mass fractions and fluxes with their pointwise counterparts in the flow channel:

$$\mathbf{n}_{\text{MeOH}} \cdot \mathbf{n} = \langle \mathbf{n}_{\text{MeOH}} \rangle \cdot \mathbf{n}, \ \mathbf{n}_{\text{CO}_2} \cdot \mathbf{n} = \langle \mathbf{n}_{\text{CO}_2} \rangle \cdot \mathbf{n}, \tag{B.5}$$

$$\langle w_{\text{MeOH}} \rangle^{(\text{l})} = w_{\text{MeOH}}, \ \langle w_{\text{CO}_2} \rangle^{(\text{l})} = w_{\text{CO}_2}, \tag{B.6}$$

where $\mathbf{n}$ is the normal vector of the interface, coupled with continuity of the pointwise velocities, tangential and normal shear stresses in the flow channel with their superficial counterparts in the porous backing:

$$v = \langle v \rangle, \ u = \langle u \rangle, \tag{B.7}$$

$$p - \mu \frac{\partial v}{\partial y} = \langle p \rangle - \frac{\mu}{\gamma} \frac{\partial \langle v \rangle}{\partial y}, \frac{\partial u}{\partial y} = \frac{1}{\gamma} \frac{\partial \langle u \rangle}{\partial y}. \tag{B.8}$$

Active layer/porous backing interface.- At $y = -h_p$, we treat the active layer as a boundary condition, whence the total superficial mass flux is given by

$$\rho \langle v \rangle = -\frac{\langle i \rangle}{6F} \left((1 + 6\alpha_{\text{H}_2\text{O}}) M_{\text{H}_2\text{O}} + M_{\text{MeOH}} - M_{\text{CO}_2} \right), \tag{B.9}$$

and the componental fluxes by

$$\rho \langle v \rangle \begin{pmatrix} \langle w_{\text{MeOH}} \rangle^{(\text{l})} \\ \langle w_{\text{CO}_2} \rangle^{(\text{l})} \end{pmatrix} - \rho\gamma \langle \mathbf{D} \rangle^{(\text{l})} \frac{\partial}{\partial Y} \begin{pmatrix} \langle w_{\text{MeOH}} \rangle^{(\text{l})} \\ \langle w_{\text{CO}_2} \rangle^{(\text{l})} \end{pmatrix} = \frac{\langle i \rangle}{6F} \begin{pmatrix} -M_{\text{MeOH}} \\ M_{\text{CO}_2} \end{pmatrix}. \tag{B.10}$$

Appendix C. Reduction of the equations for the active layer

An earlier model of the porous anode electrode of the DMFC [**11**] showed that the porous structure of the electrode is responsible for the mass transport limitations and, at high currents, finite ionic conductivity. The kinetic equation of the anode reaction was also shown to be very complex. As concentrations and potential in the active layer can vary considerably, it is desirable to take these effects into account.

Since $L >> h_{\mathrm{a}}$, it is safe to assume that the concentration gradient in the electrode is only a function of the distance across the electrode. For a given potential, any concentration of methanol at the porous backing/active layer interface corresponds to a local current density. As a consequence, it is possible to express the local current density as a function of the concentration at that location and the measured anode potential. Such a function will implicitly take into account the effects of the concentration and potential gradients. Since the kinetic equation of the anode reaction is very complex, an analytical solution will not be considered, but rather an expression that is parameter-adapted to data from the model of the active layer. Thus, the porous effects of the more detailed model is considered in the resulting expression for the local superficial current density. In order to obtain a simple expression, we restrict the domain where the function is valid to $0.3\mathrm{V} \leq E \leq 0.51$ V and 50 mol m^{-3} $\leq \langle c_{\mathrm{MeOH}} \rangle^{(\mathrm{l})} \leq 1000$ mol m^{-3}.

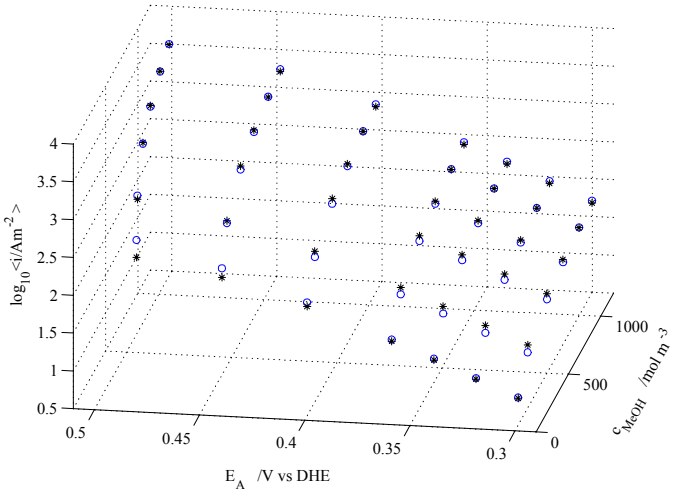

Figure A1. Comparison between the parameter-adapted kinetic function, used as local superficial current density for the boundary conditions at $(0 \leq X \leq 1, Y = -\mathcal{H})$, and the result from the more detailed anode model [**11**].

The concentration of methanol for the base case is ~ 1000 mol m^{-3} at the inlet and drops to about half of the inlet concentration. If the concentration or the potential gradients within the electrode are of interest, it is always possible to generate the gradients using the full electrode model [**11**].

Figure A1 gives the agreement between the adapted expression and the current density from the detailed model by [**11**].

The parameter-adapted expression we use is then

$$\langle i \rangle = A \left(\langle c_{\mathrm{MeOH}} \rangle^{(\mathrm{l})} \right)^{B} \frac{\exp\left(\frac{\alpha_{\mathrm{A}} F}{RT} \left(E_{\mathrm{A}} - E_0\right)\right)}{1 + \exp\left(\frac{\alpha_{\mathrm{A}} F}{RT} \left(E_{\mathrm{A}} - E_0\right)\right)}. \tag{C.1}$$

Figure A1 shows that the new expression for the local current density correlates well to the data from the electrode model in this region. The only exception is when the potential is high whilst the concentration is lower than 200 mol m^{-3}.

List of symbols

A, B	Experimentally fitted parameters
$\mathfrak{C}$	Integration constant
$\mathrm{Da} \equiv \frac{\kappa_\mathrm{p}}{L^2}$	Darcy number
$D_{\mathrm{i,j}}$	Binary diffusion coefficients for a pair (i,j), $\mathrm{m^2 s^{-1}}$
E_0	Experimentally fitted parameter, V
E_A	Electrode potential of anode vs DHE, V
F	Faraday's constant, A s $\mathrm{mol^{-1}}$
h	Height, m
$\mathcal{H} \equiv h_\mathrm{p}/h_\mathrm{f}$	Dimensionless height of porous backing
$H_{\mathrm{CO_2}}$	Henry's law coefficient, bar
i	Current density, $\mathrm{A m^{-2}}$
I	Dimensionless current density
L	Length of anode, m
M	Mean molecular mass, kg $\mathrm{mol^{-1}}$
M_i	Molar mass of species i, kg $\mathrm{mol^{-1}}$
$\mathcal{M}$, $\mathcal{M}_\mathrm{i}$	Dimensionless molar mass
p	Pressure, Pa
$\widetilde{p}, P$	Dimensionless pressures
R	Gas constant, J $\mathrm{mol^{-1}}$ $\mathrm{K^{-1}}$
$\mathrm{Re} \equiv \frac{\rho U^\mathrm{in} L}{\mu}$	Reynolds number
$\mathrm{Sc} \equiv \frac{\mu}{[D]\rho}$	Schmidt number
T	Anode temperature, K
u, v, $\mathbf{v}$	Velocities, m $\mathrm{s^{-1}}$
$\widetilde{u}$, $\widetilde{v}$, $\widetilde{\mathbf{v}}$, U, V	Dimensionless velocities
$\mathcal{V}$	Volume of the representative elementary volume, $\mathrm{m^3}$
w	Mass fraction
x, y	Coordinates in streamwise and spanwise direction, m
$\widetilde{x}, \widetilde{y}, X, Y$	Dimensionless coordinates

Greek

α	Coefficient for transport by electro-osmosis
α_{A}	Tafel slope
γ	Porosity of the porous backing
$\Gamma \equiv \Phi \mathrm{Sc} \Omega \mathcal{H} / (\Delta \gamma^{\frac{3}{2}})$	Dimensionless number
$\Delta \equiv \frac{1}{\mathrm{Re}\, \sigma^2}$	Dimensionless number
κ_{p}	Permeability of the porous backing, m^2
$\Lambda \equiv \frac{[i][M]}{\rho U^{\mathrm{in}} F}$	Dimensionless number
μ	Dynamic viscosity, kg $\mathrm{m}^{-1}\mathrm{s}^{-1}$
ρ	Density, kg m^{-3}
$\sigma \equiv \frac{h_f}{L}$	Dimensionless number
$\Sigma \equiv \frac{\sigma^2}{\mathrm{Da}^{\frac{1}{2}}}$	Dimensionless number
ϕ	General tensor
$\Phi \equiv ((1 + 6\alpha_{\mathrm{H_2O}})\, \mathcal{M}_{\mathrm{H_2O}} + \mathcal{M}_{\mathrm{MeOH}} - \mathcal{M}_{\mathrm{CO_2}})$	Dimensionless number
$\Omega \equiv \frac{\Lambda}{\sigma}$	Dimensionless number

Subscripts

a	Active layer
$\mathrm{CO_2}$	Carbon dioxide
f	Flow channel
$\mathrm{H_2O}$	Water
i	Species i
(l)	Liquid phase
MeOH	Methanol
p	Porous backing

Superscripts

in	Inlet
(l)	Liquid phase
out	Outlet

Bibliography

[1] K. Scott, W. Taama and J. Cruickshank, *J. Power Sources*, **65**, 159 (1997).
[2] K. Scott, W. Taama and J. Cruickshank, *J. Appl. Electrochem.*, **28**, 289 (1998).
[3] S. F. Baxter, V. S. Battaglia and R. E. White, *J. Electrochem. Soc.*, **146**, 437 (1999).
[4] A. A. Kulikovsky, J. Divisek and A. A. Kornyshev, *J. Electrochem. Soc.*, **147**, 953 (2000).
[5] H. Dohle, J. Divisek and R. Jung, *J. Power Sources*, **86**, 469 (2000).
[6] K. Scott, P. Argyropoulos and K. Sundmacher, *J. Electroanal. Chem.*, **477**, 97 (1999).
[7] A. A. Kulikovsky, *J. Appl. Electrochem.*, **30**, 1005 (2000).
[8] P. S. Kauranen, *Acta Polytechnica Scandinavica*, **237**, 1 (1996).
[9] K. Sundmacher, T. Schultz, S. Zhou, K. Scott, M. Ginkel and E. D. Gilles, *Chem. Eng. Sci.*, **56**, 333 (2001).
[10] S. Zhou, T. Schultz, M. Peglow and K. Sundmacher, *Phys. Chem. Chem. Phys.*, **3**, 347 (2001).
[11] J. Nordlund and G. Lindbergh, *J. Electrochem. Soc.*, **149**, A1107 (2002).
[12] A. A. Kulikovsky, *Electrochemistry Communications*, **3**, 460 (2001).
[13] A. A. Kulikovsky, *Electrochemistry Communications*, **3**, 572 (2001).
[14] Z. H. Wang and C. Y. Wang, *Proceedings Volume 2001-4*, The Electroch. Soc., USA, p. 286 (2001)
[15] C. Y. Wang and P. Cheng, *Int. J. Heat Mass Transfer*, **39**, 3607 (1996).
[16] M. Vynnycky and E. Birgersson, *submitted to SIAM Journal on Applied Mathematics (2001)*.
[17] M. Kaviany, *Principles of Heat Transfer in Porous Media*, 2nd ed., p. 15, Springer-Verlag, New York (1995).
[18] S. Whitaker, *Transport in Porous Media*, **1**, 3 (1986).
[19] J. C. Slattery, *AIChe Journal*, **13**, 1066 (1967).
[20] S. Dutta, S. Shimpalee and J. W. Van Zee, *J. Appl. Electrochem.*, **30**, 135 (2000).
[21] J. S. Yi and T. Van Nguyen, *J. Electrochem. Soc.*, **146**, 38 (1999).
[22] Landolt-Börnstein, *New Series IV/1*, p. 117, Springer, Germany (1977).
[23] *Solubility data series vol 62*, IUPAC, Oxford, GB, (1996).
[24] J. C. Tannehill, D. A. Anderson and R. H. Pletcher, *Computational Fluid Mechanics and Heat Transfer*, 2nd ed., p 462, Taylor & Francis, USA (1997).
[25] FEMLAB 2.2, http://www.comsol.se.
[26] CFX-4.4, http://www.cfx.aeat.com.
[27] J. Nordlund, A. Roessler and G. Lindbergh, *J. Appl. Electrochem.*, **32**, 259 (2002).